Polarization Transfer Observables in Elastic Electron-Proton Scattering at $Q^2 = 2.5, 5.2, 6.8$, and 8.5 GeV^2

Andrew Puckett
University of Connecticut

Jefferson Lab Seminar

January 26, 2018

UCONN Jefferson Lab

Outline

- Introduction
  - One-photon-exchange formalism for elastic electron-proton scattering
- Experiment overview: E04-108 and E04-019 (GEp-III and GEp-2γ)
- Data analysis
- Results
- Comparison to selected theoretical predictions
  - High-Q^2 data
  - Implications of GEp-2γ for TPEX physics
- (***Time permitting***) Nucleon Form Factors in the 12 GeV era
  - Hall A GMp with HRS(s)
  - SBS program
  - Hall B G_{Mn} measurement
- Summary and Conclusions

Introduction

- What this talk ***isn't***:
  - A detailed review of the entire literature on form factors, theoretical or experimental
  - A detailed overview of approved form factor experiments for the 12 GeV upgrade
  - A conclusive explanation of the cross section/polarization disagreement on the value of G_E^p
  - A talk that will explore the neutron form factors in significant depth
- What this talk ***is***:
  - An experimental talk
  - An in-depth retrospective of a "flagship" experiment of the 6 GeV era
  - A detailed exploration of the power of the polarization transfer method for precise AND accurate FF ratio measurements
  - Probably the last talk dedicated specifically to my Ph.D. experiment
  - A summary of our recent archival paper: A. J. R. Puckett et al., Phys. Rev. C 96, 055203 (2017)

Acknowledgements

- GEp-III spokespeople and core collaborators:
  - Charles Perdrisat, Vina Punjabi, Ed Brash, Mark Jones, Lubomir Pentchev, Frank Wesselmann
- MIT thesis supervisors: Bill Bertozzi and Shalev Gilad
- Fellow GEp grad students:
  - Mehdi Meziane
  - Wei Luo
- GEp-III collaboration
- Hall C and JLab Technical Staff
- Support from US DOE, Office of Science, Office of Nuclear Physics, Award ID DE-SC0014230 (Early Career research program)

Elastic eN scattering and form factors: formalism

$$\mathcal{M} = \frac{4\pi\alpha}{q^2}\bar{u}(k')\gamma^\mu u(k) g_{\mu\nu}\bar{u}(p')\left[F_1(q^2)\gamma^\nu + F_2(q^2)\frac{i\sigma^{\nu\alpha}q_\alpha}{2M}\right]u(p)$$

Invariant amplitude for elastic eN scattering in the one-photon-exchange approximation

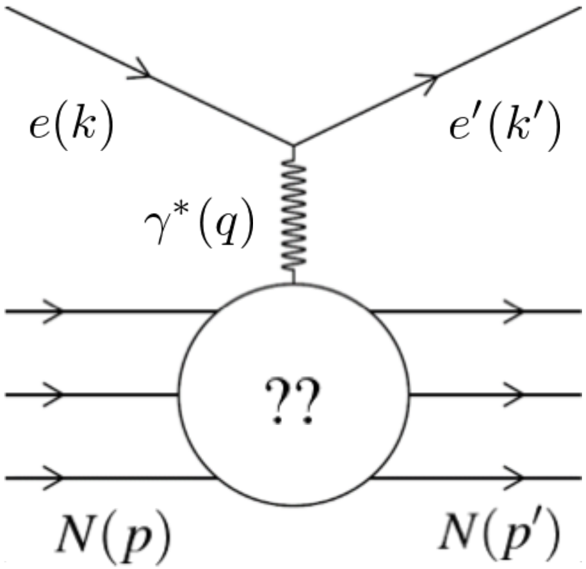

- The most general possible form of the virtual photon-nucleon vertex consistent with Lorentz invariance, parity conservation and gauge invariance is described by two form factors F_1 (Dirac) and F_2 (Pauli):
  - F_1 describes the helicity-conserving amplitude (charge and Dirac magnetic moment)
  - F_2 describes the helicity-flip amplitude (anomalous magnetic moment contribution)

$$G_E \equiv F_1 - \tau F_2$$
$$G_M \equiv F_1 + F_2$$
$$\tau \equiv \frac{Q^2}{4M^2}$$

Sachs Form Factors G_E (electric) and G_M (magnetic), are experimentally convenient linearly independent combinations of F_1, F_2

$$\frac{d\sigma}{d\Omega_e} = \frac{\alpha^2}{Q^2}\left(\frac{E'_e}{E_e}\right)^2 \cot^2\left(\frac{\theta_e}{2}\right)\left[\frac{G_E^2 + \frac{\tau}{\varepsilon}G_M^2}{1+\tau}\right]$$

$$\varepsilon^{-1} \equiv 1 + 2(1+\tau)\tan^2\left(\frac{\theta_e}{2}\right)$$

$$\sigma_R \equiv \frac{\varepsilon(1+\tau)\frac{d\sigma}{d\Omega_e}}{\left(\frac{d\sigma}{d\Omega_e}\right)_{Mott}} = \varepsilon G_E^2 + \tau G_M^2$$

Differential cross section in the nucleon rest frame:
Rosenbluth formula

Rosenbluth Separation Method: Measure cross section at fixed Q^2 as a function of ε to obtain G_E^2 (slope) and G_M^2 (intercept).

Rosenbluth Separation Method

- The nucleon structure-dependent part of the cross section factorizes from the "point-like" part.
- The "reduced cross section" σ_R depends linearly on ϵ for a given Q^2, with slope G_E^2 and intercept τG_M^2.
- Experimentally, one measures $d\sigma/d\Omega$ while varying the beam energy and scattering angle to change ϵ while holding Q^2 constant

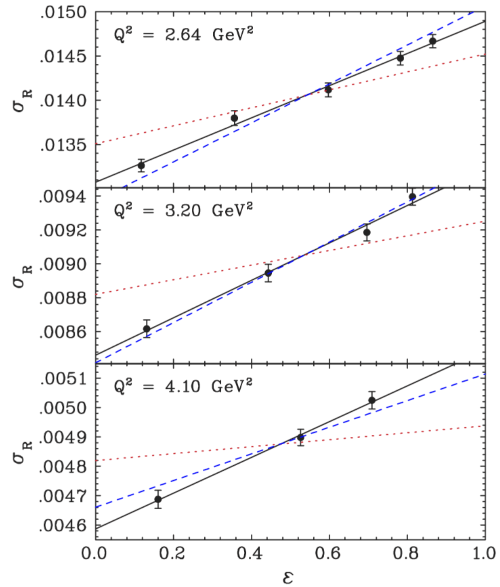

FIG. 2 (color online). Reduced cross sections as a function of ε. The solid line is a linear fit to the reduced cross sections, the dashed line shows the slope expected from scaling ($\mu_p G_E/G_M = 1$), and the dotted line shows the slope predicted by the polarization transfer experiments [6].

Qattan *et al.*, **Phys. Rev. Lett.** 94, 142301 (2005)

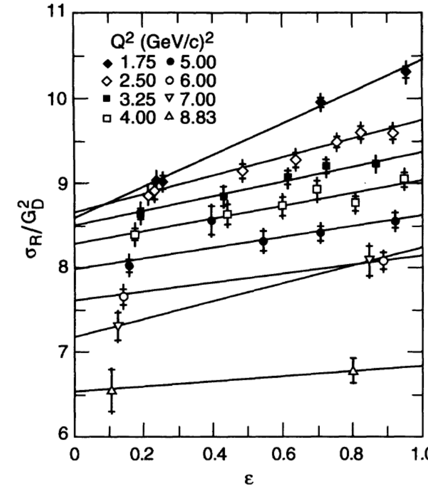

FIG. 22. Reduced cross sections divided by the square of the dipole fit plotted versus ϵ for each value of Q^2. The 1.6 GeV data points correspond to the leftmost point on each line, and the E136 data point is the rightmost point on the Q^2 = 8.83 (GeV/c)^2 line. The inner error bars show the statistical error, while the outer error bars show the total point-to-point uncertainty, given by the quadrature sum of the statistical and point-to-point systematic errors. An overall normalization uncertainty of ±1.77% has not been included.

Andivahis *et al.*, **Phys. Rev. D** 50, 5491 (1994)

$$\frac{d\sigma}{d\Omega_e} = \left(\frac{d\sigma}{d\Omega_e}\right)_{Mott} \frac{\epsilon G_E^2 + \tau G_M^2}{\epsilon(1+\tau)}$$

$$\tau \equiv \frac{Q^2}{4M_p^2}$$

$$\left(\frac{d\sigma}{d\Omega_e}\right)_{Mott} = \frac{\alpha^2 \cos^2\left(\frac{\theta_e}{2}\right)}{4E_e^2 \sin^4\left(\frac{\theta_e}{2}\right)} \frac{E_e'}{E_e}$$

$$\epsilon \equiv \left[1 + 2(1+\tau)\tan^2\left(\frac{\theta_e}{2}\right)\right]^{-1}$$

$$\sigma_R = \epsilon G_E^2 + \tau G_M^2$$

Polarization Transfer in Elastic *eN* scattering

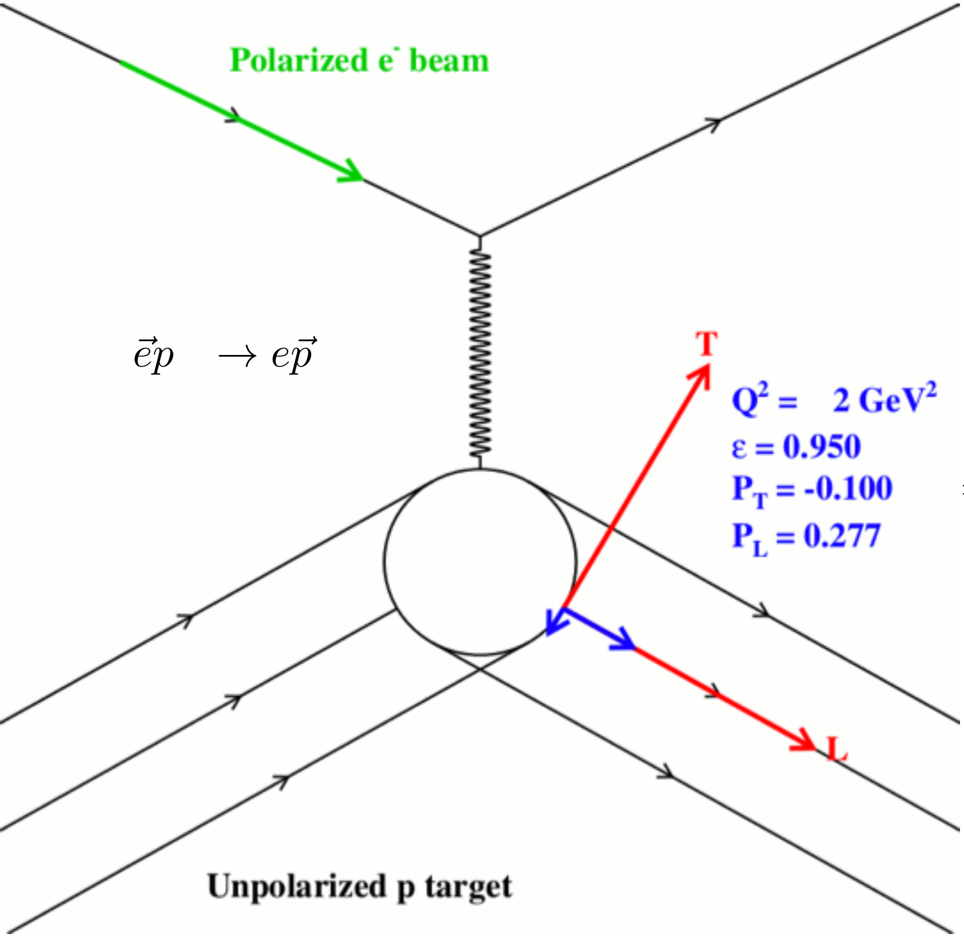

$$P_t = -P_{beam}\sqrt{\frac{2\epsilon(1-\epsilon)}{\tau}}\frac{r}{1+\frac{\epsilon}{\tau}r^2}$$

$$P_\ell = P_{beam}\frac{\sqrt{1-\epsilon^2}}{1+\frac{\epsilon}{\tau}r^2}$$

$$P_n = 0$$

$$r \equiv \frac{G_E}{G_M}$$

$$\Longrightarrow R_p \equiv \mu_p\frac{G_E^p}{G_M^p} = -\mu_p\sqrt{\frac{\tau(1+\epsilon)}{2\epsilon}}\frac{P_t}{P_\ell}$$

- Akhiezer and Rekalo (1968) + Arnold, Carlson, Gross (1981):
  - ***Derived relations between transferred polarization components in elastic eN scattering and the ratio of electromagnetic FFs R = $\mu G_E/G_M$***
- Perdrisat + Punjabi, 1993 proposal to CEBAF PAC: A ***simultaneous*** measurement of the two recoil polarization components in a polarimeter determines the FF ratio while canceling many systematic uncertainties (beam polarization, analyzing power, FPP instrumental asymmetry)

- ***The ratio of transferred polarization components is directly proportional to G_E/G_M, and therefore much more sensitive to G_E at large Q^2 than the cross section***

Polarized Beam-Polarized Target Asymmetry

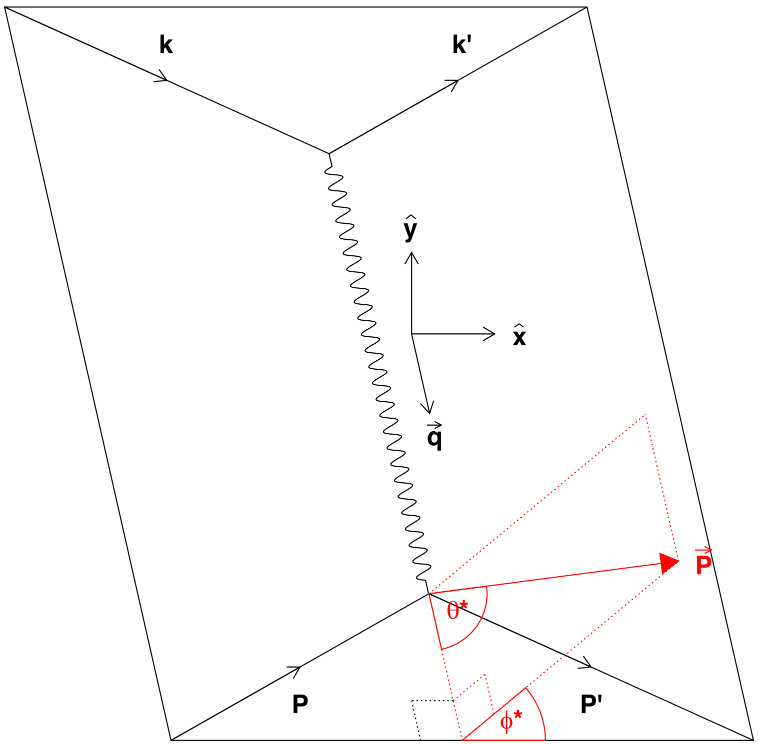

- The beam helicity asymmetry in elastic *eN* scattering from a polarized target is related to the transferred polarization by time reversal symmetry.
- The asymmetry A_t for target polarization perpendicular to the momentum transfer but parallel to the scattering plane ($\theta^* = 90°, \phi^* = 0$) equals the transverse component P_t of the transferred polarization.
- The asymmetry A_ℓ for target polarization along the momentum transfer direction ($\theta^* = 0$) is equal in magnitude but opposite in sign to the longitudinal transferred polarization P_ℓ.
- The sign change between A_ℓ and P_ℓ is due to the proton spin flip required for the absorption of the transversely polarized virtual photon

$$\vec{\mathbf{P}} \equiv \text{Target polarization}$$

$$\begin{aligned}
A_{eN} &= -\frac{P_{beam}P_{target}}{1+\frac{\epsilon}{\tau}r^2}\left[\left(\sqrt{\frac{2\epsilon(1-\epsilon)}{\tau}}\sin\theta^*\cos\phi^*\right)r + \sqrt{1-\epsilon^2}\cos\theta^*\right] \\
&\equiv P_{target}\left[A_t\sin\theta^*\cos\phi^* + A_\ell\cos\theta^*\right] \\
A_t &= P_t \\
A_\ell &= -P_\ell \\
A_n &= P_n = 0
\end{aligned}$$

Proton FFs—Rosenbluth data

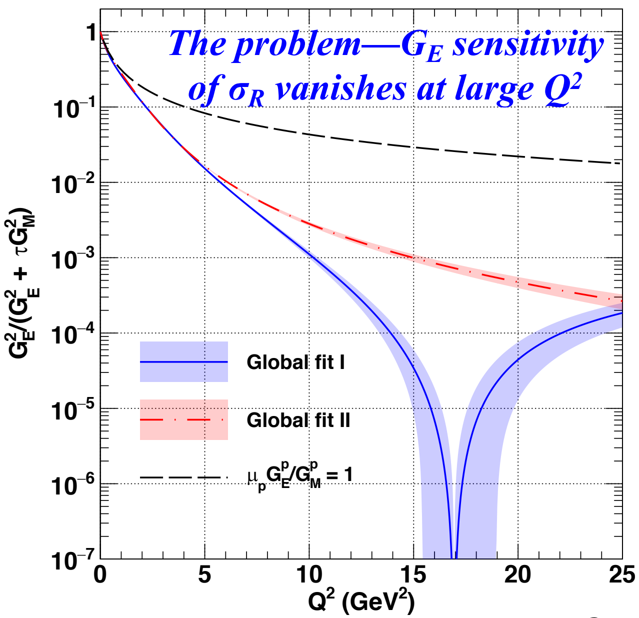

Maximum contribution of G_E^2 term to σ_R vanishes at large τ. Fits to FF data are described in [Phys. Rev. C, 96, 055203 (2017)] (more on these later)

$$\sigma_R = \epsilon G_E^2 + \tau G_M^2$$

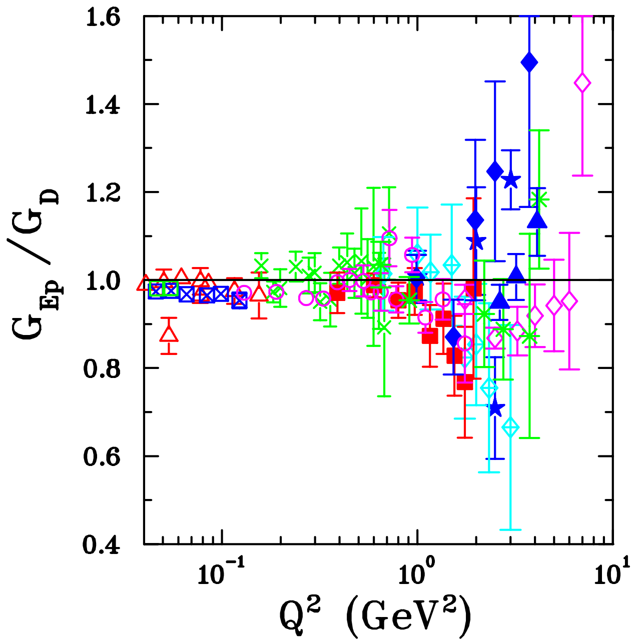

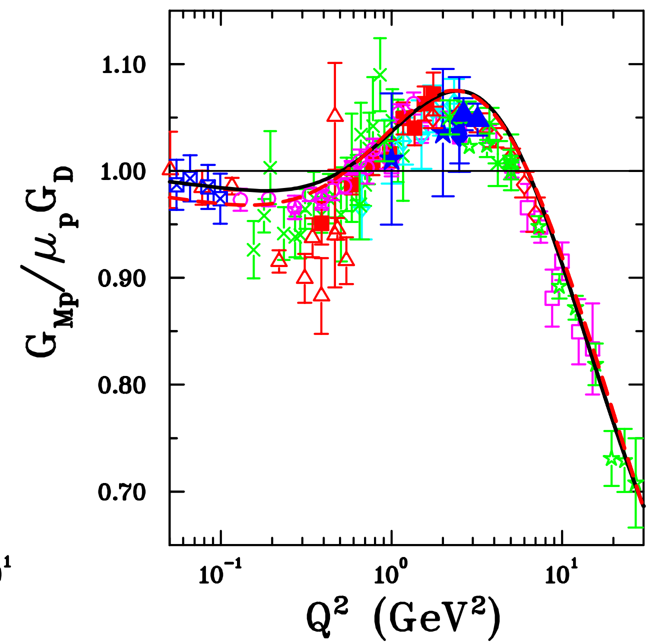

G_E^p and G_M^p Rosenbluth Data: $G_E^p \approx \frac{G_M^p}{\mu_p} \approx G_D$

$$G_D \equiv \left(1 + \frac{Q^2}{\Lambda^2}\right)^{-2}$$
$$\Lambda^2 = 0.71 \text{ GeV}^2$$

- Elastic *ep* cross sections have been measured for $0.003 \leq Q^2 \leq 31.2$ GeV^2.
- Rosenbluth data for G_E^p and G_M^p are qualitatively described by the "dipole" form factor, which is the Fourier transform of a spherically symmetric, exponentially decreasing radial charge/magnetization density.

Polarization Transfer data for G_E^p/G_M^p (prior to GEp-III)

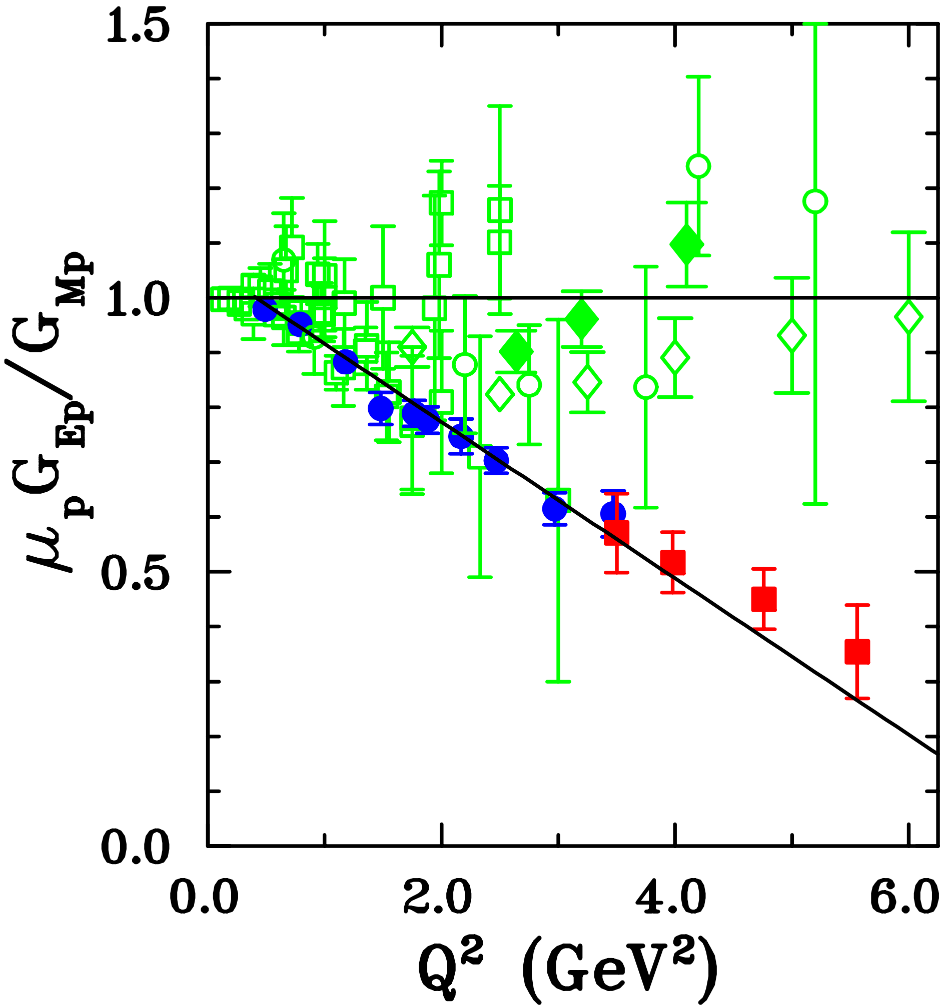

GEp-I and GEp-II results from Hall A with selected Rosenbluth data. Figure from [Phys. Rev. C, 96, 055203 (2017)]

- **GEp-I: Jones *et al.*, Phys. Rev. Lett. 84, 1398 (2000)**
  - **825 INSPIRE-HEP citations (1/12/2017)**
  - **Final results: Punjabi *et al.*, Phys. Rev. C 71, 055202 (2005)**
- **GEp-II: Phys. Rev. Lett. 88, 092301 (2002)**
  - **749 INSPIRE-HEP citations (1/12/2017)**
  - **Final results: Puckett *et al.*, Phys. Rev. C 85, 045203 (2012)**
- *Extraction of the same physical property of the proton from different experimental observables yields different results!*
- Guichon and Vanderhaeghen, **PRL** 91, 142303 (2003): *"This discrepancy is a serious problem as it generates confusion and doubt about the whole methodology of lepton scattering experiments."*
- General consensus: the polarization method provides the most reliable determination of G_{Ep}, due to superior experimental sensitivity and precision, and robustness of the physical observable against radiative and multi-photon-exchange corrections.
- Discrepancy still needs to be fully understood:
  - Refinement of higher-order corrections
  - Direct experimental determination of TPEX contributions

APS physics

2017 Tom W. Bonner Prize in Nuclear Physics Recipient

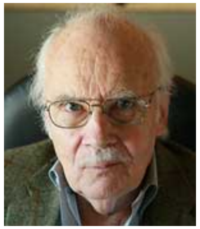

Charles F. Perdrisat
College of William and Mary

Citation:

"*For groundbreaking measurements of nucleon structure, and discovering the unexpected behavior of the magnetic and electric nucleon form factors with changing momentum transfer.*"

Background:

Charles F. Perdrisat, Ph.D., was a professor at the College of William and Mary (Williamsburg, Va.) for the last 50 years having retired earlier this year. Throughout his career, Dr. Perdrisat's research focus included nuclear reactions with proton and deuteron beams, both polarized and unpolarized. He conducted research at SATURNE in Saclay, France, TRIUMF in Vancouver, B.C., LAMPF in Los Alamos, New Mexico, Brookhaven National Laboratory in Upton, N.Y., and JINR in Dubna, Russia. During the last half of his career, he was committed to the investigation of the structure of the proton at Jefferson Laboratory, concentrating in obtaining polarization transfer data in the scattering of polarized electrons on unpolarized protons. These data, from 3 distinct experiments organized in close collaboration with Vina Punjabi, Ph.D., Mark K. Jones, Ph.D., Edward J. Brash, Ph.D., and Lubomir Pentchev, Ph.D., have resulted in a significant change of paradigm in the understanding of the structure of the nucleon. After completing his undergraduate training in physics and mathematics at the University of Geneva in 1956, Dr. Perdrisat became an assistant in the physics department at the Swiss Federal Institute of Technology in Zurich) in Switzerland, under Prof. Paul Scherrer; he received his Ph.D. in 1962. He completed a three-year postdoctoral fellowship at the University of Illinois Urbana-Champaign, before heading to William and Mary in 1966.

Selection Committee:

2017 Selection Committee Members: Rocco Schiavilla (Chair), D. Hertzog, P. Jacobs, Kate Jones, I-Y. Lee

Experiments E04-108 (GEp-III) and E04-019 (GEp-2γ)

The GEp-III and GEp-2γ experiments in Hall C

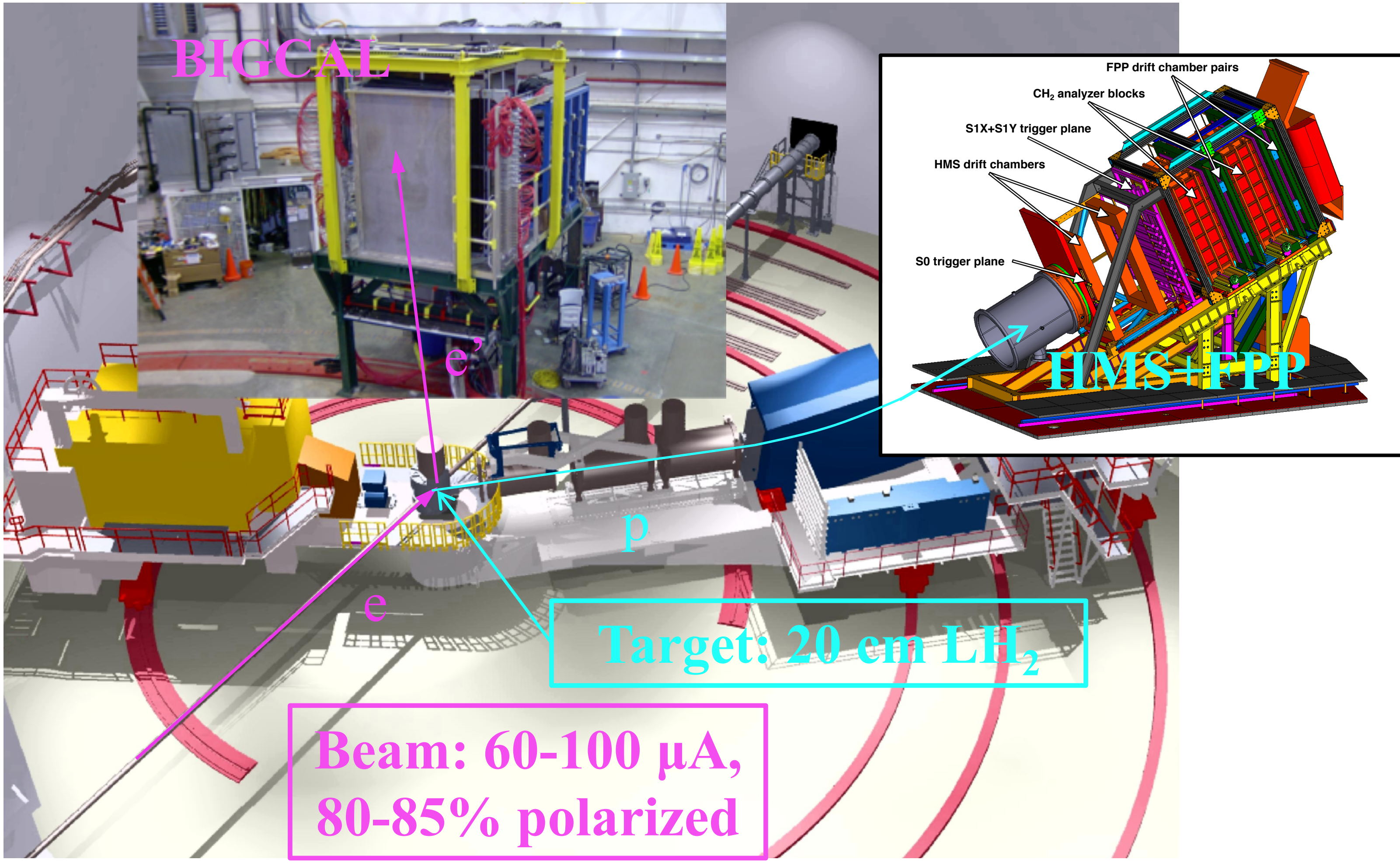

- Polarization transfer in ^{1}H(**e**,e'**p**). Nominal luminosity ~ 4×10^{38} Hz/cm^2
- "Fast" beam helicity reversal (30 Hz) cancels FPP instrumental asymmetry in polarization transfer observables

Kinematics

TABLE I. Central kinematics of the GEp-III and GEp-2γ experiments. Q^2 denotes the central or nominal Q^2 value, defined by the central momentum setting of the High Momentum Spectrometer (HMS) in which the proton was detected. ϵ is the value of the kinematic parameter defined in equation (3) computed from the incident beam energy (not corrected for energy loss in the target prior to scattering), and the central Q^2. E_e is the incident beam energy, averaged over the duration of each running period. E'_e is the scattered electron energy at the nominal Q^2. The central angle of BigCal is denoted θ_e, and can differ slightly from the electron scattering angle at the central Q^2. p_p is the HMS central momentum setting. θ_p is the HMS central angle. χ is the central spin precession angle in the HMS, P_e is the average beam polarization, and D_{cal} is the distance from the origin to the surface of BigCal.

Dates (mm/dd-mm/dd, yyyy)	Q^2 (GeV^2)	ϵ	E_e (GeV)	E'_e (GeV)	θ_e (°)	p_p (GeV)	θ_p (°)	χ (°)	P_e (%)	D_{cal} (m)
11/27-12/08, 2007	2.50	0.154	1.873	0.541	105.2	2.0676	14.5	108.5	85.9	4.93
01/17-01/25, 2008	2.50	0.150	1.868	0.536	105.1	2.0676	14.5	108.5	85.5	4.94
12/09-12/16, 2007	2.50	0.633	2.847	1.515	44.9	2.0676	31.0	108.5	84.0	12.00
12/17-12/20, 2007	2.50	0.772	3.548	2.216	32.6	2.0676	35.4	108.5	85.8	11.16
01/05-01/11, 2008	2.50	0.789	3.680	2.348	30.8	2.0676	36.1	108.5	85.2	11.03
11/07-11/20, 2007	5.20	0.377	4.052	1.281	60.3	3.5887	17.9	177.2	79.5	6.05
05/27-06/09, 2008	6.80	0.506	5.711	2.087	44.2	4.4644	19.1	217.9	79.5	6.08
04/04-05/27, 2008	8.54	0.235	5.712	1.161	69.0	5.4070	11.6	262.2	80.9	4.30

- GEp-III goal: extend knowledge of G_E^p/G_M^p to highest practically achievable Q^2, given maximum available beam energy (ca. 2008) of ~5.71 GeV
  - Hall C HMS was used due to its max. central momentum of 7.4 GeV/c (Hall A HRSs have $p_{max} = 4.0$ GeV/c, corresponding to $Q^2_{max} \approx 5.9$ GeV^2).
- GEp-2γ goal: Measure the ϵ dependence of polarization transfer observables in $ep \to ep$ with $\leq 1\%$ total uncertainty at a fixed Q^2 in the region of the Rosenbluth/PT discrepancy

A Brief Historical Digression

Owl shift summary, 1/25/2008

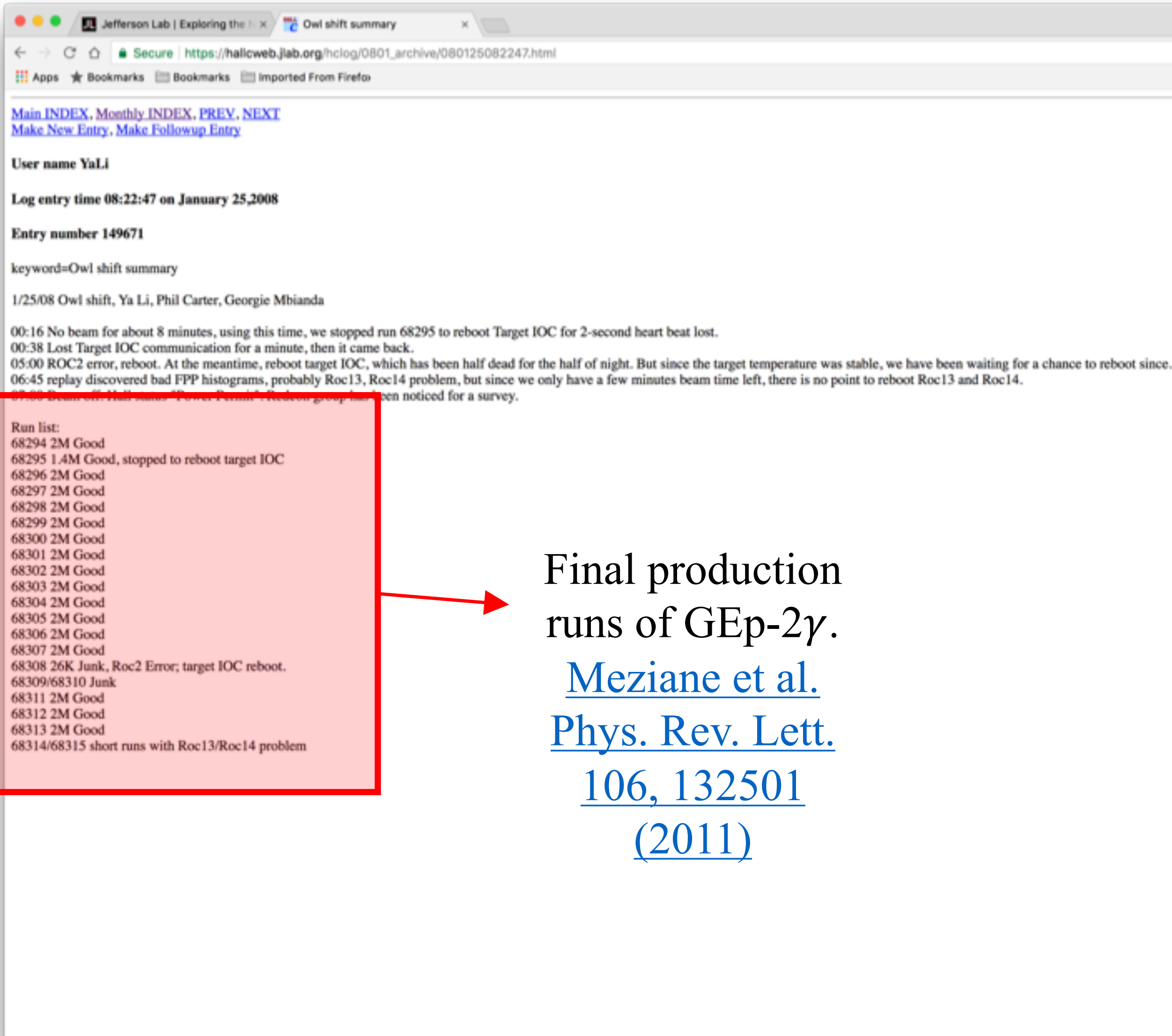

Main INDEX, Monthly INDEX, PREV, NEXT
Make New Entry, Make Followup Entry

User name YaLi

Log entry time 08:22:47 on January 25,2008

Entry number 149671

keyword=Owl shift summary

1/25/08 Owl shift, Ya Li, Phil Carter, Georgie Mbianda

00:16 No beam for about 8 minutes, using this time, we stopped run 68295 to reboot Target IOC for 2-second heart beat lost.
00:38 Lost Target IOC communication for a minute, then it came back.
05:00 ROC2 error, reboot. At the meantime, reboot target IOC, which has been half dead for the half of night. But since the target temperature was stable, we have been waiting for a chance to reboot since.
06:45 replay discovered bad FPP histograms, probably Roc13, Roc14 problem, but since we only have a few minutes beam time left, there is no point to reboot Roc13 and Roc14.
07:00 Beam off. Hall status "Power Permit". Radcon group has been noticed for a survey.

Run list:
68294 2M Good
68295 1.4M Good, stopped to reboot target IOC
68296 2M Good
68297 2M Good
68298 2M Good
68299 2M Good
68300 2M Good
68301 2M Good
68302 2M Good
68303 2M Good
68304 2M Good
68305 2M Good
68306 2M Good
68307 2M Good
68308 26K Junk, Roc2 Error; target IOC reboot.
68309/68310 Junk
68311 2M Good
68312 2M Good
68313 2M Good
68314/68315 short runs with Roc13/Roc14 problem

Final production runs of GEp-2γ.
Meziane et al. Phys. Rev. Lett. 106, 132501 (2011)

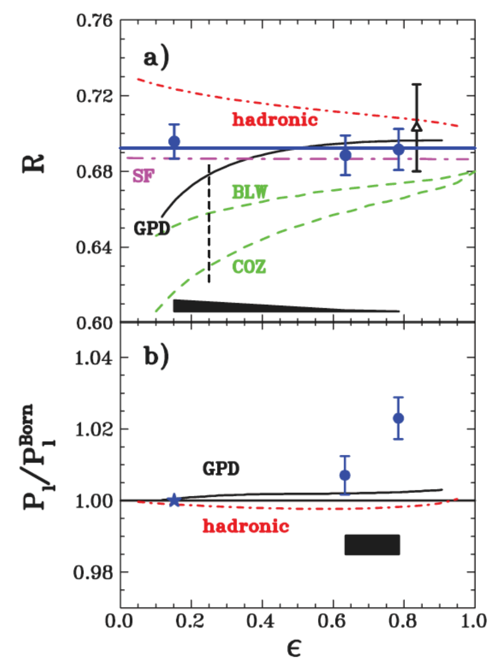

Screenshot from Hall C Logbook, Day Shift, 1/26/2008

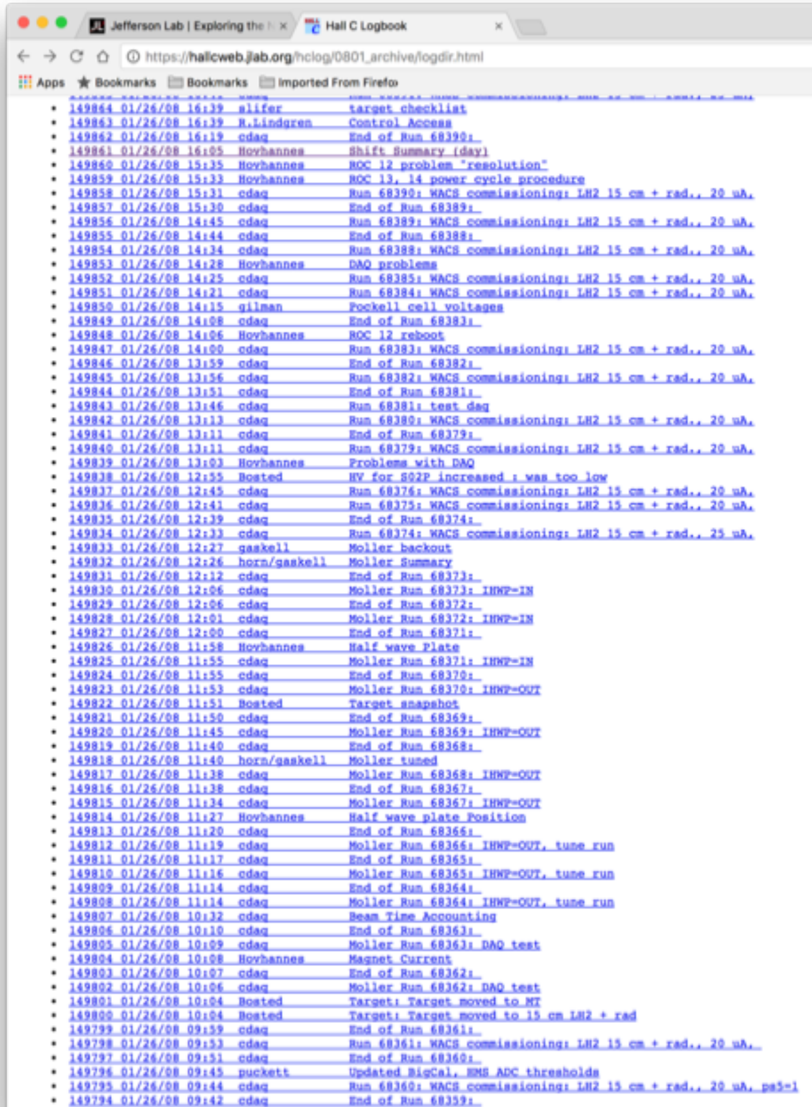
Jefferson Lab | Exploring the N
Hall C Logbook
https://hallcweb.jlab.org/hclog/0801_archive/logdir.html
Apps Bookmarks Bookmarks Imported From Firefox

- 149864 01/26/08 16:39 slifer target checklist
- 149863 01/26/08 16:39 R.Lindgren Control Access
- 149862 01/26/08 16:19 cdaq End of Run 68390:
- 149861 01/26/08 16:05 Hovhannes Shift Summary (day)
- 149860 01/26/08 15:35 Hovhannes ROC 12 problem "resolution"
- 149859 01/26/08 15:33 Hovhannes ROC 13, 14 power cycle procedure
- 149858 01/26/08 15:31 cdaq Run 68390: WACS commisioning: LH2 15 cm + rad., 20 uA,
- 149857 01/26/08 15:30 cdaq End of Run 68389:
- 149856 01/26/08 14:45 cdaq Run 68389: WACS commisioning: LH2 15 cm + rad., 20 uA,
- 149855 01/26/08 14:44 cdaq End of Run 68388:
- 149854 01/26/08 14:34 cdaq Run 68388: WACS commisioning: LH2 15 cm + rad., 20 uA,
- 149853 01/26/08 14:28 Hovhannes DAQ problems
- 149852 01/26/08 14:25 cdaq Run 68385: WACS commisioning: LH2 15 cm + rad., 20 uA,
- 149851 01/26/08 14:21 cdaq Run 68384: WACS commisioning: LH2 15 cm + rad., 20 uA,
- 149850 01/26/08 14:15 gilman Pockell cell voltages
- 149849 01/26/08 14:08 cdaq End of Run 68383:
- 149848 01/26/08 14:06 Hovhannes ROC 12 reboot
- 149847 01/26/08 14:00 cdaq Run 68383: WACS commisioning: LH2 15 cm + rad., 20 uA,
- 149846 01/26/08 13:59 cdaq End of Run 68382:
- 149845 01/26/08 13:56 cdaq Run 68382: WACS commisioning: LH2 15 cm + rad., 20 uA,
- 149844 01/26/08 13:51 cdaq End of Run 68381:
- 149843 01/26/08 13:46 cdaq Run 68381: test daq
- 149842 01/26/08 13:13 cdaq Run 68380: WACS commisioning: LH2 15 cm + rad., 20 uA,
- 149841 01/26/08 13:11 cdaq End of Run 68379:
- 149840 01/26/08 13:11 cdaq Run 68379: WACS commisioning: LH2 15 cm + rad., 20 uA,
- 149839 01/26/08 13:03 Hovhannes Problems with DAQ
- 149838 01/26/08 12:55 Bosted HV for S02P increased : was too low
- 149837 01/26/08 12:45 cdaq Run 68376: WACS commisioning: LH2 15 cm + rad., 20 uA,
- 149836 01/26/08 12:41 cdaq Run 68375: WACS commisioning: LH2 15 cm + rad., 20 uA,
- 149835 01/26/08 12:39 cdaq End of Run 68374:
- 149834 01/26/08 12:33 cdaq Run 68374: WACS commisioning: LH2 15 cm + rad., 25 uA,
- 149833 01/26/08 12:27 gaskell Moller backout
- 149832 01/26/08 12:26 horn/gaskell Moller Summary
- 149831 01/26/08 12:12 cdaq End of Run 68373:
- 149830 01/26/08 12:06 cdaq Moller Run 68373: IHWP=IN
- 149829 01/26/08 12:06 cdaq End of Run 68372:
- 149828 01/26/08 12:01 cdaq Moller Run 68372: IHWP=IN
- 149827 01/26/08 12:00 cdaq End of Run 68371:
- 149826 01/26/08 11:58 Hovhannes Half wave Plate
- 149825 01/26/08 11:55 cdaq Moller Run 68371: IHWP=IN
- 149824 01/26/08 11:55 cdaq End of Run 68370:
- 149823 01/26/08 11:53 cdaq Moller Run 68370: IHWP=OUT
- 149822 01/26/08 11:51 Bosted Target snapshot
- 149821 01/26/08 11:50 cdaq End of Run 68369:
- 149820 01/26/08 11:45 cdaq Moller Run 68369: IHWP=OUT
- 149819 01/26/08 11:40 cdaq End of Run 68368:
- 149818 01/26/08 11:40 horn/gaskell Moller tuned
- 149817 01/26/08 11:38 cdaq Moller Run 68368: IHWP=OUT
- 149816 01/26/08 11:38 cdaq End of Run 68367:
- 149815 01/26/08 11:34 cdaq Moller Run 68367: IHWP=OUT
- 149814 01/26/08 11:27 Hovhannes Half wave plate Position
- 149813 01/26/08 11:20 cdaq End of Run 68366:
- 149812 01/26/08 11:19 cdaq Moller Run 68366: IHWP=OUT, tune run
- 149811 01/26/08 11:17 cdaq End of Run 68365:
- 149810 01/26/08 11:16 cdaq Moller Run 68365: IHWP=OUT, tune run
- 149809 01/26/08 11:14 cdaq End of Run 68364:
- 149808 01/26/08 11:14 cdaq Moller Run 68364: IHWP=OUT, tune run
- 149807 01/26/08 10:32 cdaq Beam Time Accounting
- 149806 01/26/08 10:10 cdaq End of Run 68363:
- 149805 01/26/08 10:09 cdaq Moller Run 68363: DAQ test
- 149804 01/26/08 10:08 Hovhannes Magnet Current
- 149803 01/26/08 10:07 cdaq End of Run 68362:
- 149802 01/26/08 10:06 cdaq Moller Run 68362: DAQ test
- 149801 01/26/08 10:04 Bosted Target: Target moved to MT
- 149800 01/26/08 10:04 Bosted Target: Target moved to 15 cm LH2 + rad
- 149799 01/26/08 09:59 cdaq End of Run 68361:
- 149798 01/26/08 09:53 cdaq Run 68361: WACS commisioning: LH2 15 cm + rad., 20 uA,
- 149797 01/26/08 09:51 cdaq End of Run 68360:
- 149796 01/26/08 09:45 puckett Updated BigCal, HMS ADC thresholds
- 149795 01/26/08 09:44 cdaq Run 68360: WACS commisioning: LH2 15 cm + rad., 20 uA, ps5=1
- 149794 01/26/08 09:42 cdaq End of Run 68359:

- Changeover from GEp-2γ to Wide-angle Compton Scattering: Fanelli et al., Phys. Rev. Lett. 115, 152001 (2015)

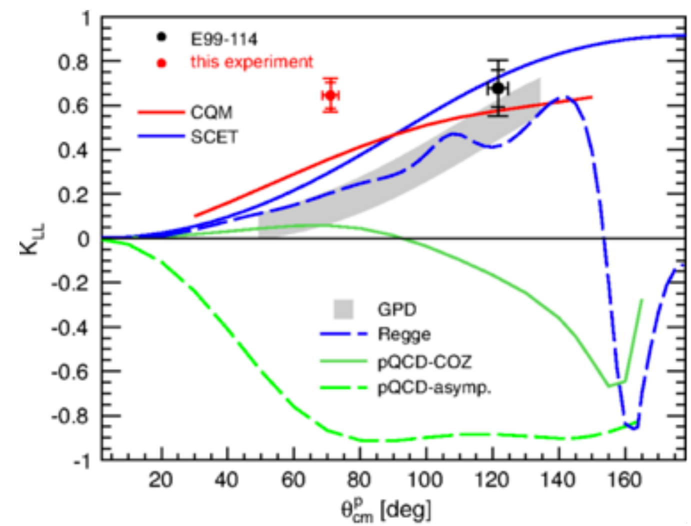

Hall C GEp Apparatus

High Momentum Spectrometer (HMS)

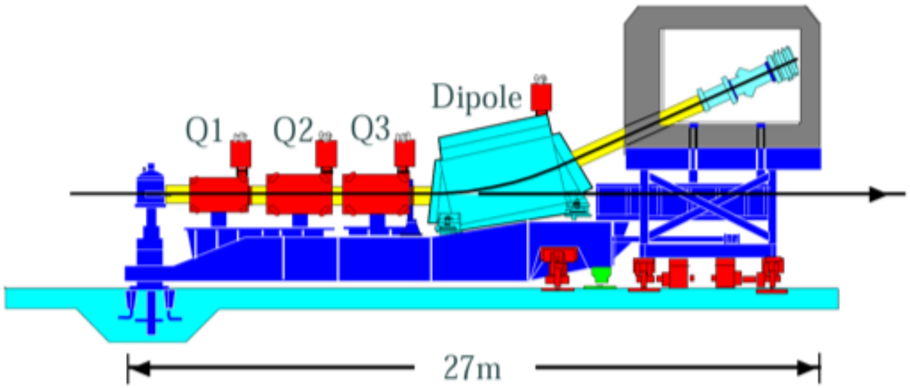

- QQQD superconducting, 25° vertical bend magnetic spectrometer, max central momentum $p_{max} = 7.4$ GeV/c
- Acceptance:
  - 6.74 msr solid angle (~2:1 vertical/horizontal aspect ratio)
  - ±9% momentum bite
  - ±5 cm/sin ϑ extended target acceptance
- Resolution (standard detector configuration):
  - $\frac{\sigma_p}{p} \approx 10^{-3}$
  - Angular resolution ~1 mrad
  - Vertex resolution ~2 mm (perpendicular to optical axis)

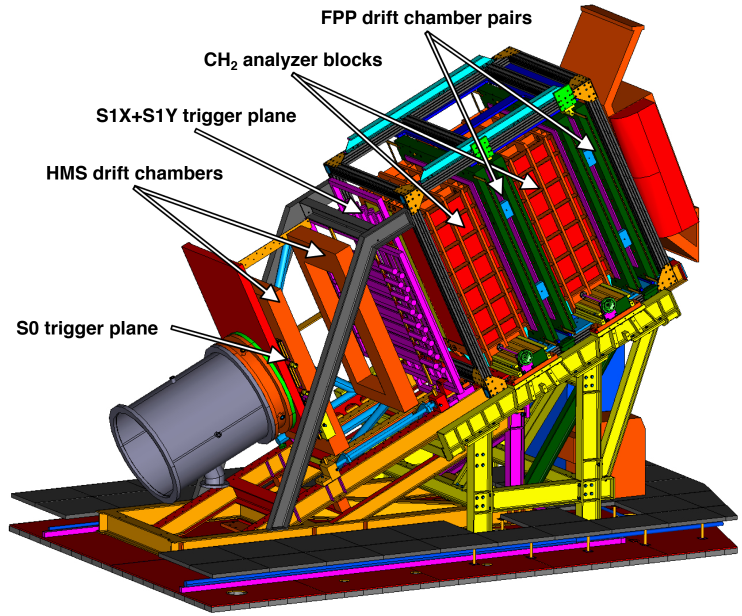

Detector package for GEp-III:

- Drift chambers: track scattered protons for kinematic reconstruction and incident FPP track definition
- Scintillator hodoscopes: trigger and timing (resolution ~250 ps)
- FPP: measure proton polarization
- S0: restrict acceptance to reduce trigger rate

Focal Plane Polarimeter (FPP)

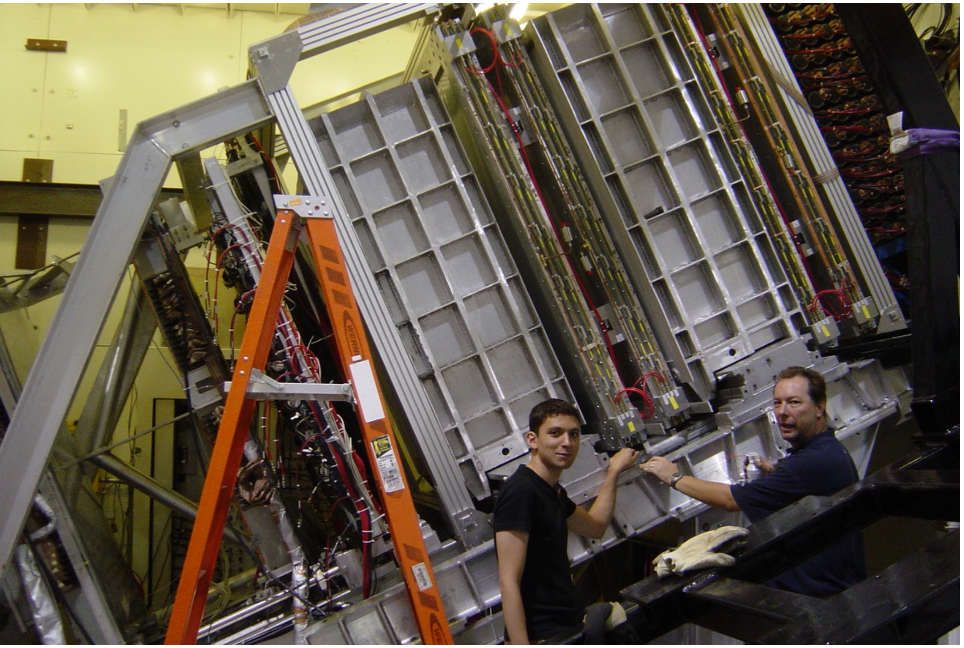

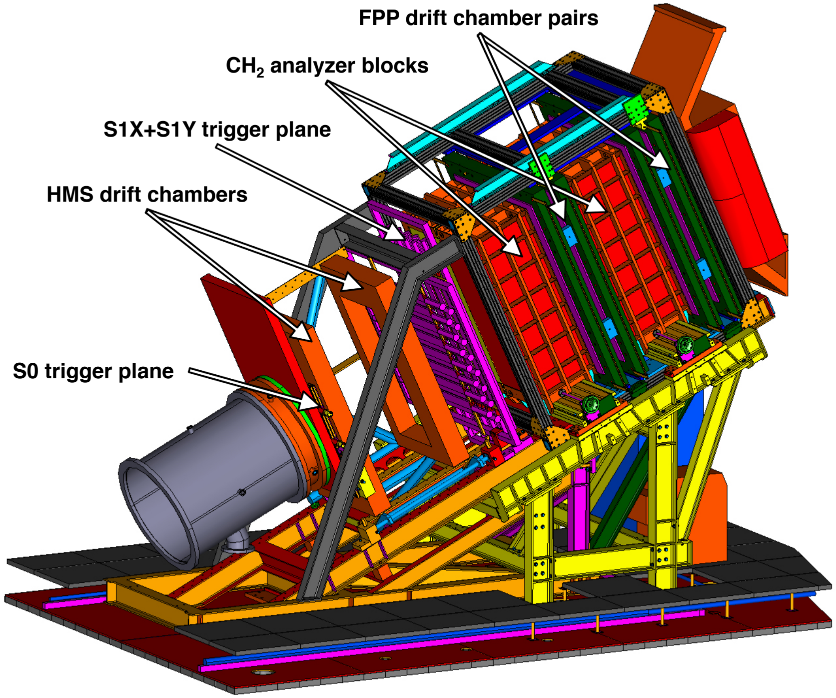

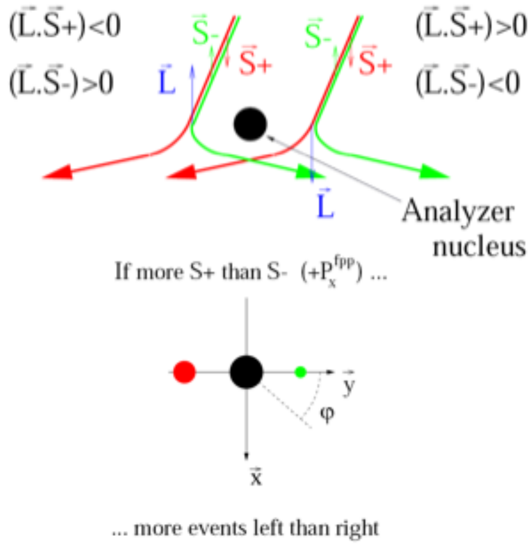

- Proton polarimetry via proton-nucleus scattering is based on the spin-orbit coupling in the nucleon-nucleon force.
- A spin-1/2 particle, such as a proton, is preferentially deflected by a spin-orbit force along the direction of $\vec{p}\times\vec{S}$, where $\vec{p}$ is the incident proton momentum, and $\vec{S}$ is the proton spin.
  - Note that a spin-orbit force is insensitive to longitudinal polarization!
- By tracking the incident and scattered proton and measuring the azimuthal asymmetry in the angular distribution of secondary scatterings, the incident proton's (transverse) polarization can be reconstructed
- Retractable CH$_2$ analyzers allow collection of "straight-through" data for calibration/alignment

FPP design aspects and motivation

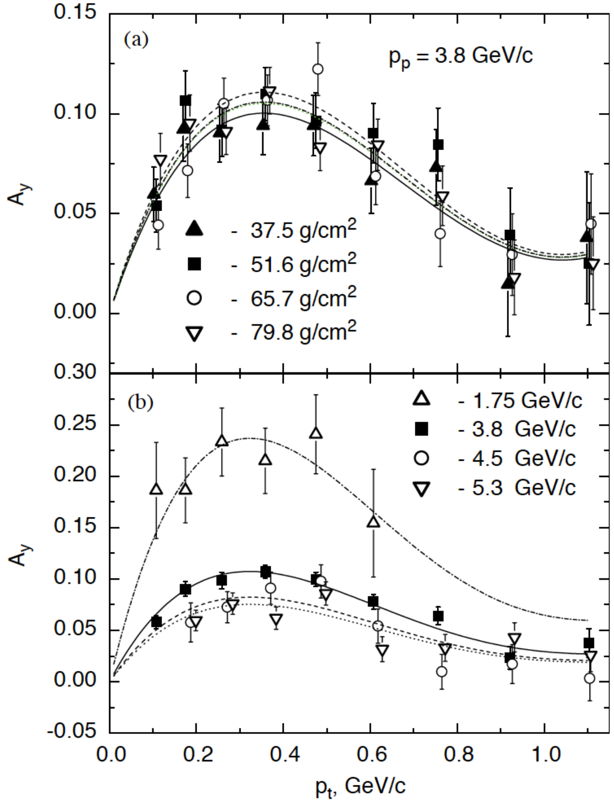

Fig. 4. Analyzing powers as a function of p_t: (a) for different target thicknesses at $p_p = 3.8\,\mathrm{GeV}/c$; (b) for different momenta at $L = 51.6\,\mathrm{g/cm^2}$.

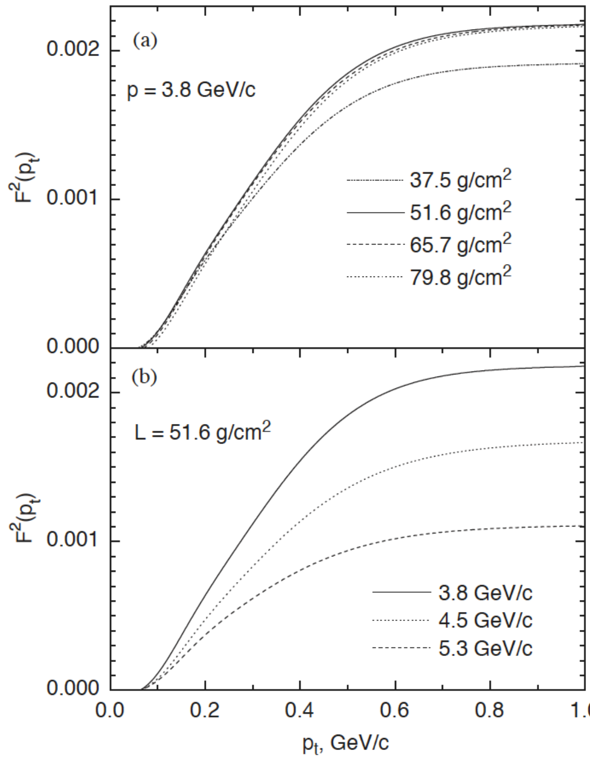

Fig. 6. Figure of merit as a function of p_t: (a) for different target thicknesses at $p_p = 3.8\,\mathrm{GeV}/c$; (b) for different momenta at $L = 51.6\,\mathrm{g/cm^2}$.

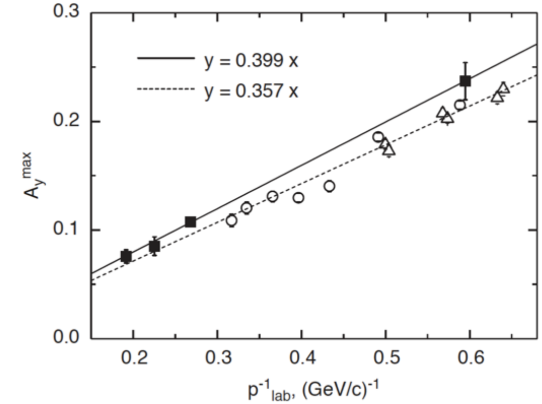

Fig. 5. Momentum dependence of CH_2- and C-data. Solid squares—current data, open circles— Ref. [4], open triangles— Ref. [5]. Solid line—fit of CH_2-data, dashed line—fit of C-data.

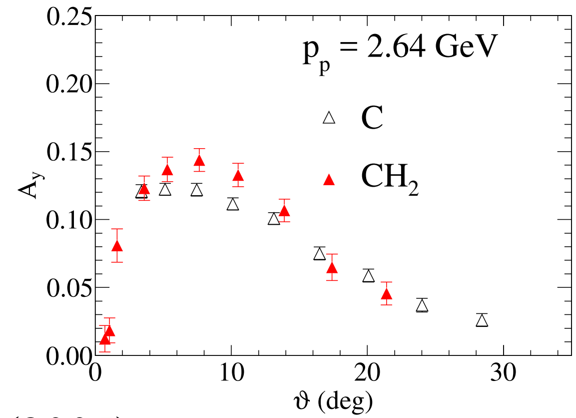

Azhgirey *et al.*, Nucl. Instr. Meth. A, 538, 441 (2005):

- Analyzing power roughly independent of target thickness at 3.8 GeV
- Polarimeter figure-of-merit essentially saturates beyond one nuclear collision length λ_T of CH_2 thickness (at 3.8 GeV proton momentum, anyway) and for transverse momenta $p_T = p_p \sin\vartheta \geq 0.7$ GeV
- CH_2 analyzing power significantly higher than C in the few-GeV momentum range
- Stacking two polarimeters in series, each with approximately one λ_T analyzer thickness, increases FPP FOM by ~1.5

FPP drift chamber design

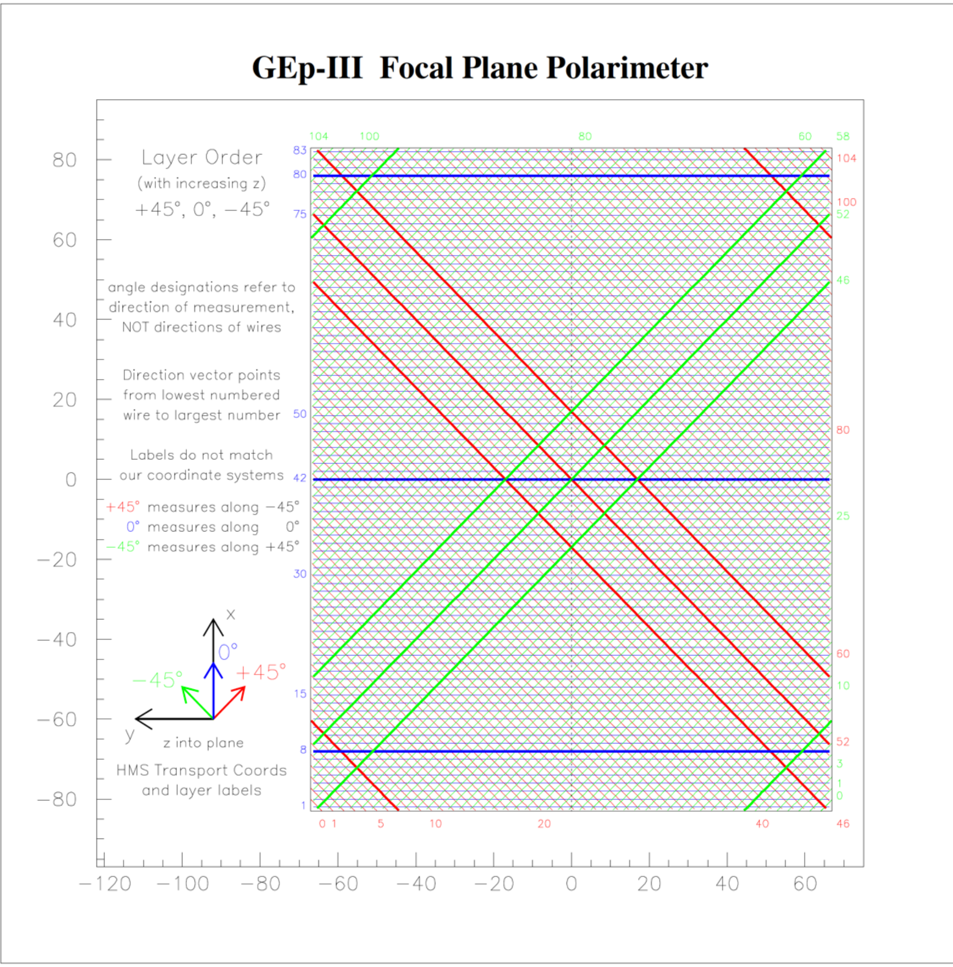

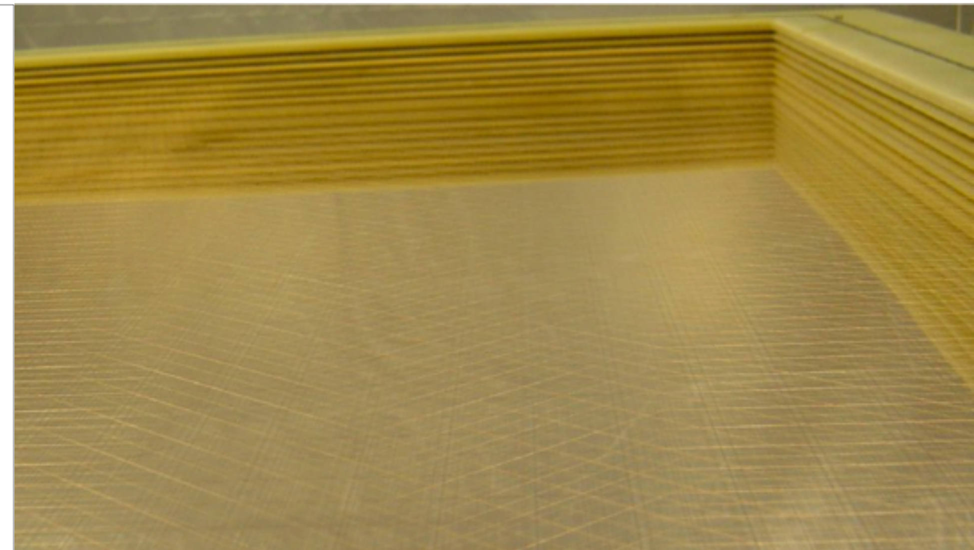

TABLE III. Characteristics of the wires used in the FPP drift chambers. The sense wires are gold-plated tungsten, while the cathode and field wires are made of a beryllium-bronze alloy.

Type	Diameter (μm)	Tension (g)
Sense	30	70
Field	100	150
Cathode	80	120

- Each chamber consists of three planes of sense wires, oriented at $\pm 45°, 90°$ relative to HMS dispersive direction, with 2-cm "pitch"
- Protons tracked after each analyzer by a pair of FPP chambers, ***six planes in total***

- FPP chambers and CH_2 analyzers are on separate support frames, to insure that FPP chambers cannot move upon insertion/retraction of the CH_2 analyzers
- Space in the HMS hut, cost considerations/etc limited the number of wire planes used for FPP tracking system.

FPP performance: coordinate and angular resolution

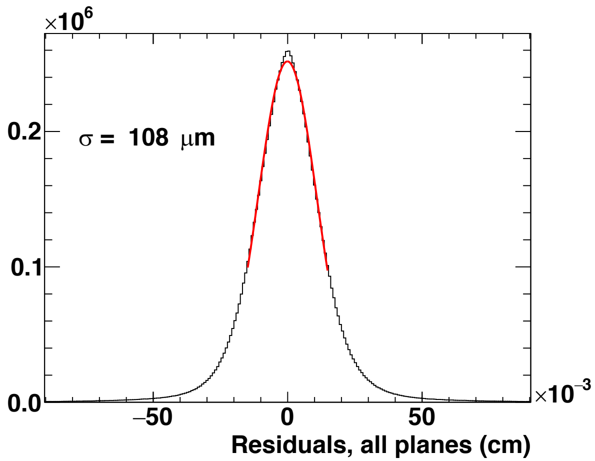

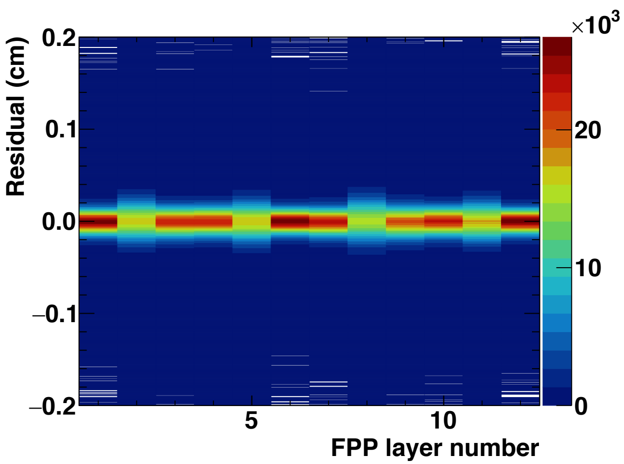

- Width of tracking residuals for straight-through tracks with all six planes firing average about 100 μm for 2.4 GeV electrons, slightly worse for 2.1-5.4 GeV protons.

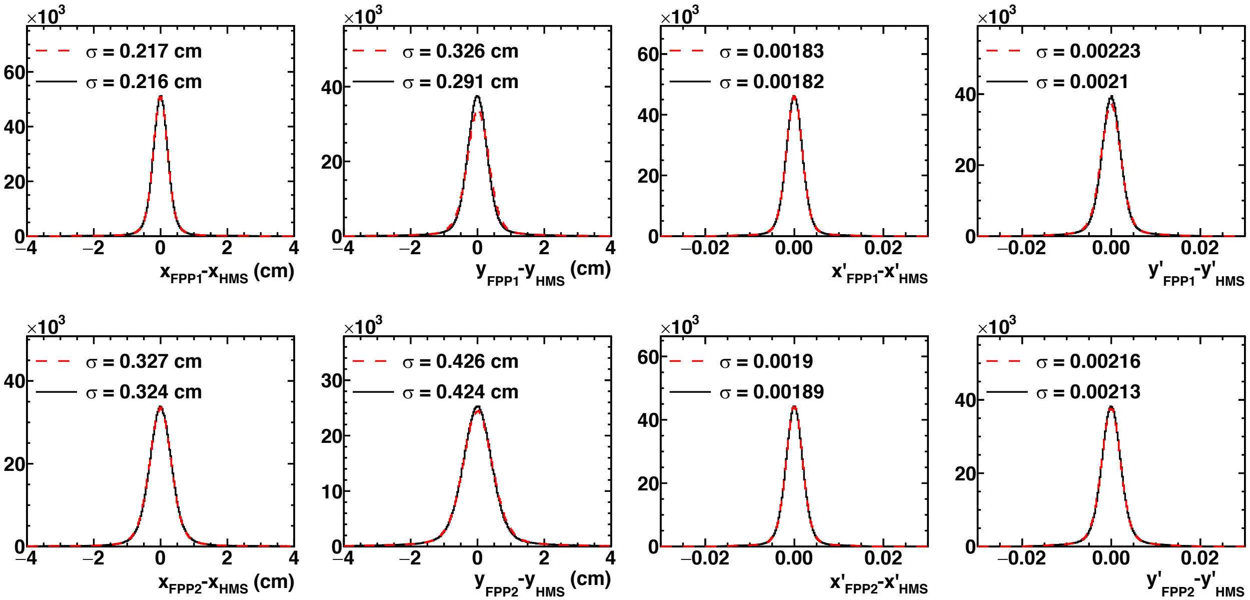

FPP-HMS track parameter differences, before (**after**) alignment corrections

- Observed tracking residuals correspond to an intrinsic coordinate resolution of ≈ 270 μm, which is consistent with observed HMS drift chamber resolution (same gas mixture, similar electric field/drift velocity/readout characteristics)
- As measured by track slope differences between FPP/HMS for straight-through tracks, FPP angular resolution is $\sigma_{x'}(\sigma_{y'}) = 1.8\ (2.1)$ mrad. The resolution asymmetry between the "x" and "y" directions results from the orientation/layout of the wire planes.
- The smallest polar scattering angle accepted in the analysis is ~0.5 degrees = 9 mrad (for $Q^2 = 8.5$ GeV^2, $p_p = 5.4$ GeV/c)

“S0”

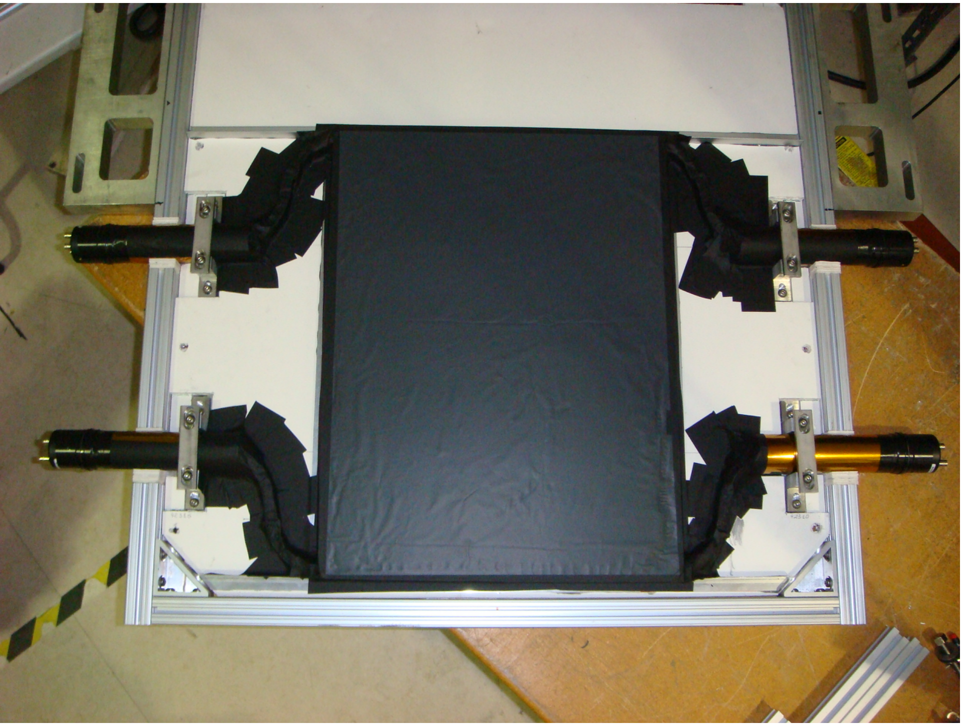

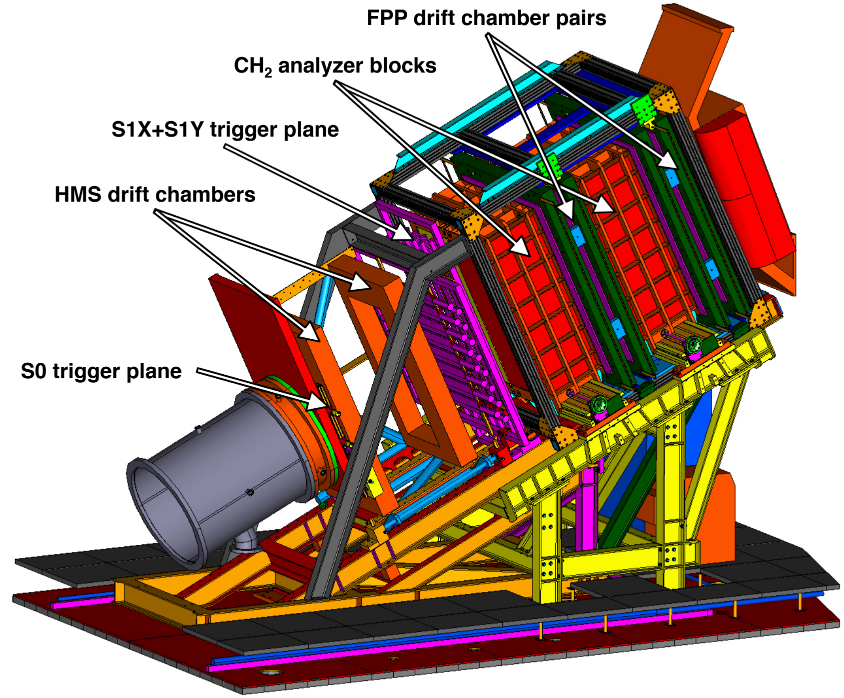

- 1-cm-thick plastic scintillator installed upstream of HMS drift chambers to restrict acceptance to the region of the HMS focal plane populated by elastically scattered protons, and reject inelastic background processes that occur at a much higher rate, particularly for high-Q^2 and/or low-ϵ kinematics. Consists of two paddles, $15'' \times 12'' \times 1\ cm$, coupled to Photonis PMTs
- This addition (or something similar, given HMS space constraints) was necessary to achieve a manageable trigger rate for the DAQ, even in coincidence with BigCal
- Side effect—multiple scattering prior to tracking chambers makes HMS angular resolution approximately 3X worse (at 2.1 GeV momentum), compared to standard configuration.

BigCal

- 1,744 lead-glass blocks, “TF1-0” type
  - “Protvino” section (bottom): 32×32 array, $3.8\times3.8\times45$ cm^3.
  - “RCS” section (top): 30×24 array, $4.0\times4.0\times40$ cm^3
- Optically isolated via aluminized mylar wrapping
- Russian FEU-84 PMTs
- Calorimeter positioned at maximum distance from target consistent with HMS acceptance matching for $ep \rightarrow ep$ kinematics, space limitations in Hall C, and cable length

- Detecting the elastically scattered electron in coincidence was necessary to manage trigger rate and suppress inelastic backgrounds—large solid angle was needed to match proton arm acceptance for high-Q^2 kinematics—precludes use of an existing magnetic spectrometer (e.g., SOS in Hall C)
- 4” aluminum absorber in front of BigCal, used for all but one of the production kinematics, mitigates radiation damage to the lead-glass

BigCal Performance (coordinate/energy/timing resolution)

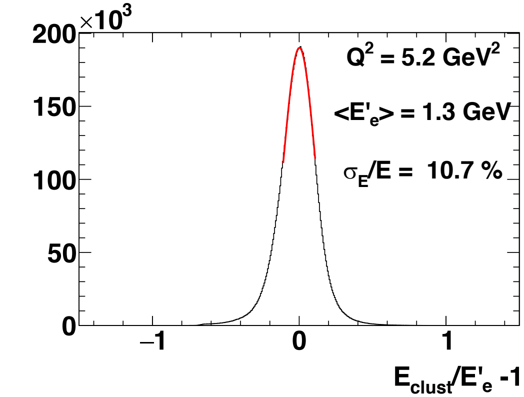

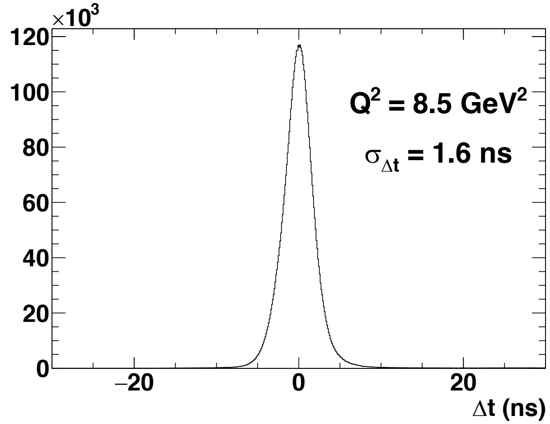

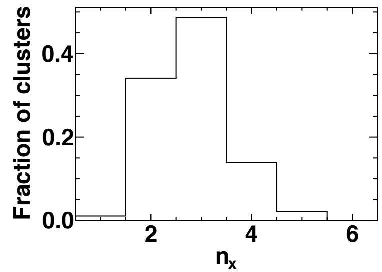

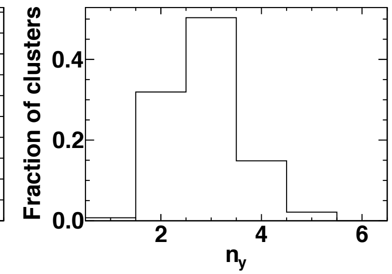

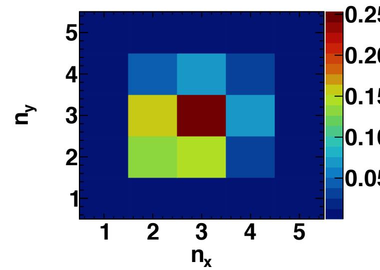

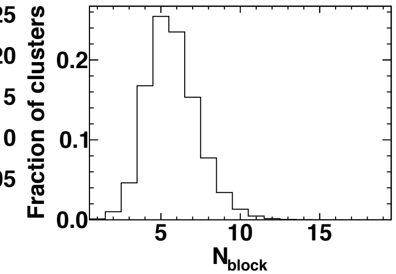

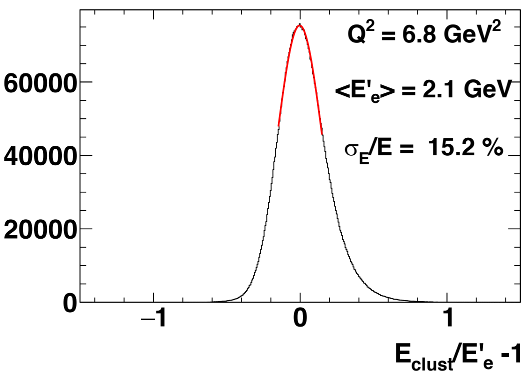

- Clustering results (above right):
  - Typical cluster size is 3×3.
  - ~98% of elastic electron clusters at least 2×2
  - Average (most probable) total number of hits above software threshold ~5.8 (5)

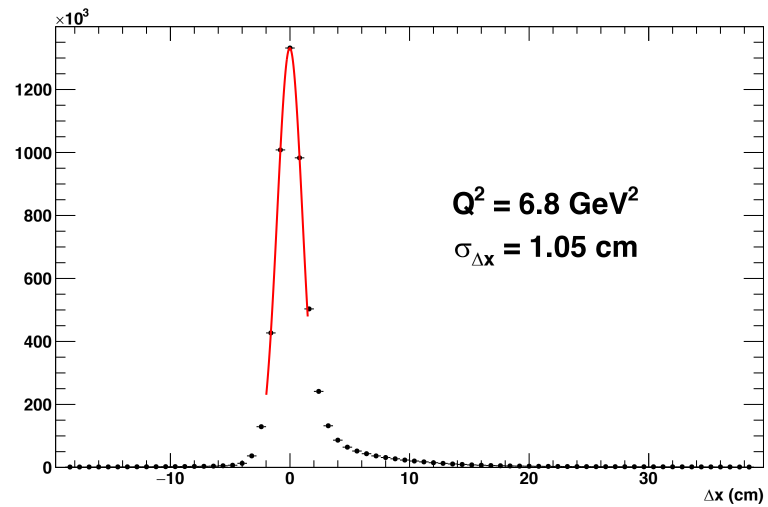

- Energy resolution (above, left) was (intentionally) degraded by 4”-thick Al absorber in front, used to mitigate radiation damage.
  - Radiation-induced darkening of lead-glass worsened energy resolution by ~factor of 2 from beginning to end of experiment, even including the partial UV curing that occurred during Feb.-March 2008 accelerator shutdown
- BigCal timing resolution ~1.5 ns (above, middle)
- BigCal coordinate resolution ~5-6 mm (bottom right)

Implied shower coordinate resolution is ~6 mm after subtracting contributions of HMS momentum/vertex resolution and multiple scattering in air

Data Analysis

Elastic Event Selection, GEp-III

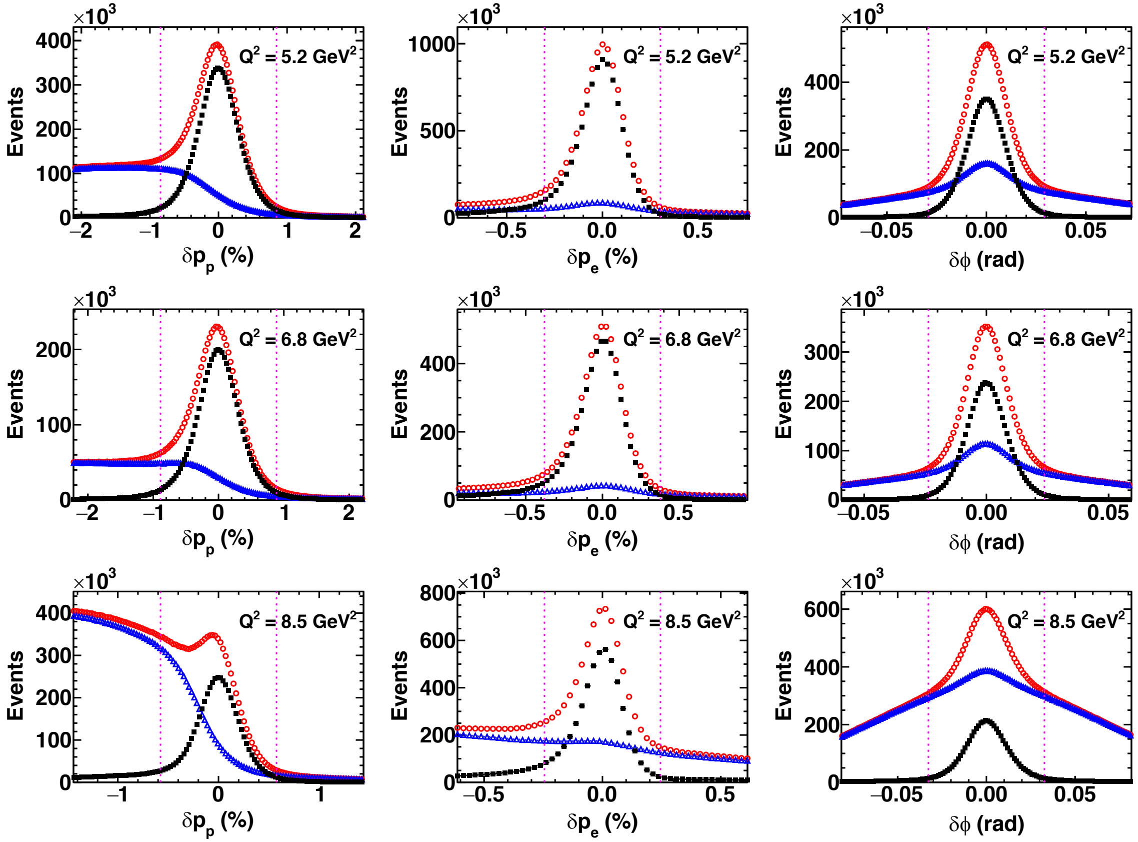

$$\delta p_p \equiv 100 \times \frac{p_p - p_p(\theta_p)}{p_0}$$

$$\delta p_e \equiv 100 \times \frac{p_p - p_p(\theta_e)}{p_0}$$

$$\delta \phi \equiv \phi_e - \phi_p - \pi$$

$$p_0 = \text{HMS central momentum}$$

- BigCal energy resolution was too poor to provide meaningful discrimination between elastic/inelastic events for any cut with a high efficiency for elastics—therefore, no cuts were applied to the reconstructed shower energy, beyond the BigCal trigger threshold and the software minimum cluster energy
- The proton momentum and the proton and electron scattering angles are the useful quantities for elastic event selection
- Three cuts were applied:
  - Proton polar angle-proton momentum correlation “δp_p”
  - Electron polar angle-proton momentum correlation “δp_e”
  - *ep* azimuthal angle correlation “$\delta \phi$”
- These three cuts produce a very clean and highly efficient selection of elastic events
- Dominant background processes are $\gamma p \to \pi^0 p$ and $ep \to ep\pi^0$, which are kinematically indistinguishable within the experimental acceptance
- Contributions from scattering in the aluminum entry and exit windows of the LH_2 target cell are essentially negligible

Elastic Event Selection, GEp-2γ ($Q^2 = 2.5$ GeV^2)

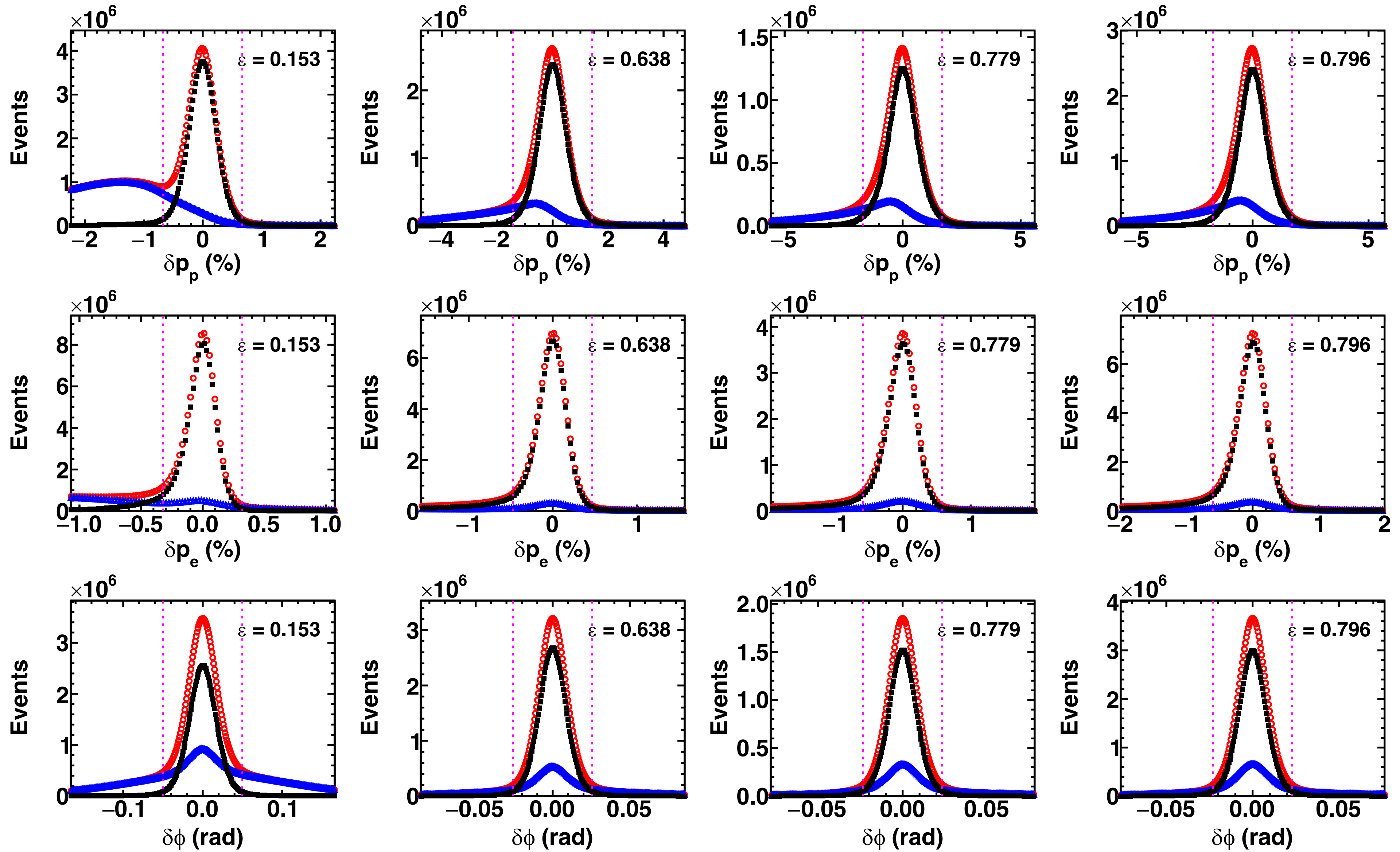

Variable-width exclusivity cuts

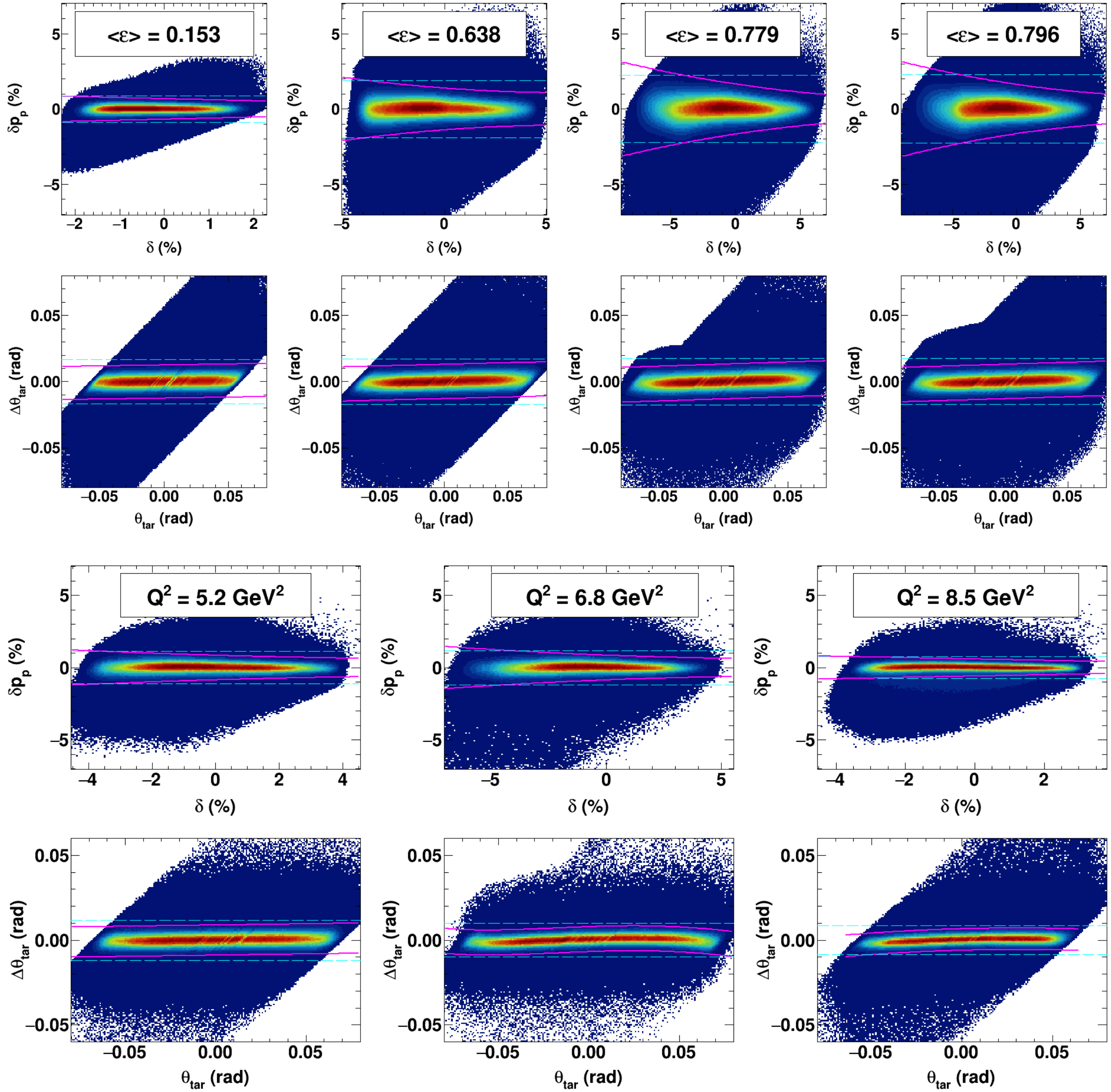

- Variable-width cuts were applied to δp_p as a function of $\delta \equiv 100\times\left(\frac{p_p}{p_0}-1\right)$ and to $\delta\phi$, or, equivalently, $\Delta\theta_{tar}$, as a function of the HMS dispersive-plane trajectory angle θ_{tar}, to optimize the efficiency and purity of the elastic event selection within the acceptance, and to minimize cut-induced bias of the reconstructed proton kinematics, which are the inputs to the HMS spin transport calculation
- The resolution of δp_p was observed to vary significantly as a function of the proton momentum within the HMS acceptance, by more than a factor of two at $(Q^2, \epsilon) = (2.5, 0.79)$, the setting with the largest δ coverage for elastically scattered protons
- The elastic peak position in $\delta\phi/\Delta\theta_{tar}$ exhibited slight correlations with θ_{tar}, with deviations from zero in $\Delta\theta_{tar}$ not exceeding 2 mrad.

Inelastic Background Estimation, I

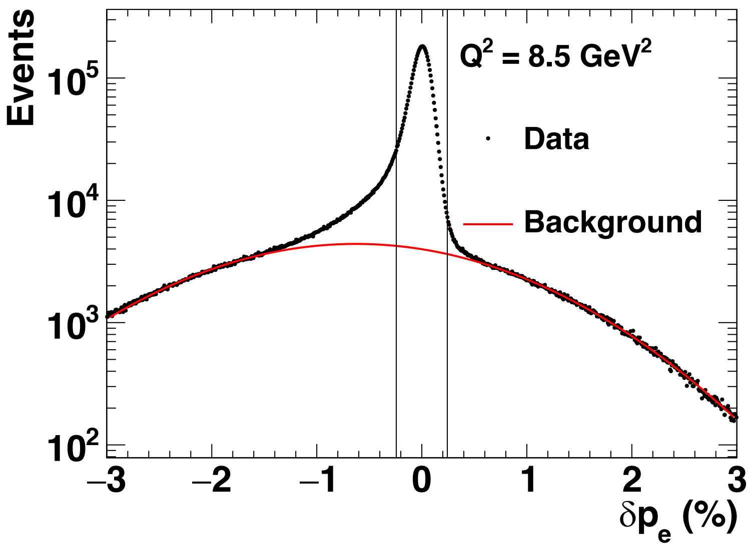

TABLE IV. (color online) Estimated fractional background contamination $f \equiv \frac{B}{S+B}$ (where B and S refer to the background and the signal, respectively) within the final, $\pm 3\sigma$ cut region of the δp_e distribution, for all the kinematics of the GEp-III and GEp-2γ experiments. The estimates shown are obtained after applying $\pm 3\sigma$ cuts to δp_p and $\delta\phi$. The quoted uncertainties are statistical only. The quoted beam energy E_e is the value from Table I, which is averaged over the duration of the running period, and *not* corrected for energy loss in the LH$_2$ target.

Q^2 (GeV^2)	E_e (GeV)	$(f \pm \Delta f_{stat})$ (%)
2.5	1.873	0.435 ± 0.002
2.5	1.868	0.512 ± 0.001
2.5	2.847	0.161 ± 0.002
2.5	3.548	0.198 ± 0.002
2.5	3.680	0.208 ± 0.001
5.2	4.052	1.018 ± 0.004
6.8	5.711	0.748 ± 0.004
8.5	5.712	4.89 ± 0.01

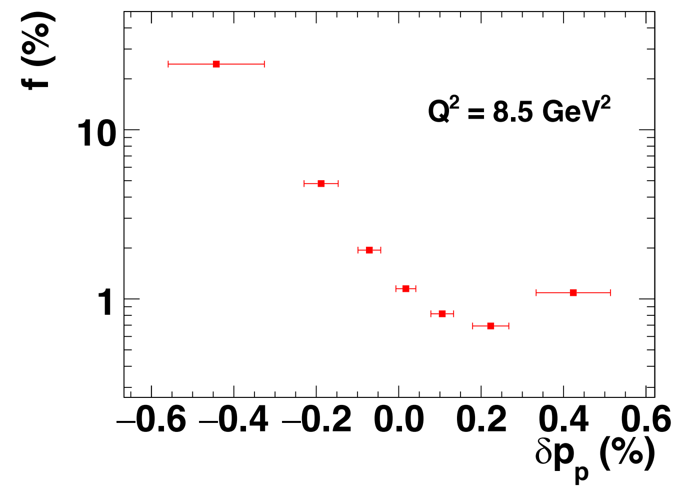

Fractional inelastic contamination vs. δp_p within final cut region, $Q^2 = 8.5\ GeV^2$

- The δp_e distribution is used to estimate the residual inelastic contamination of the final elastic *ep* selection, because the background shape under the elastic peak is smooth and relatively uniform (see next slide), and also because the resolution of δp_e is roughly constant within the acceptance.
- The cuts applied to $\delta p_e, \delta\phi$ strongly suppress the radiative tail of the δp_p spectrum for elastic events.
- Elastically scattered protons have the highest kinematically allowed momenta for positively charged particles produced on a free proton target→ $\delta p_p < 0$ for inelastic reactions on hydrogen.
- The separation between ep and $\pi^0 p$ reactions (at "threshold") in terms of δp_p is comparable to the experimental resolution.
- Scattering from Al target endcaps dominates the "superelastic" ($\delta p_p > 0$) region due to Fermi smearing of events into the "forbidden" region.

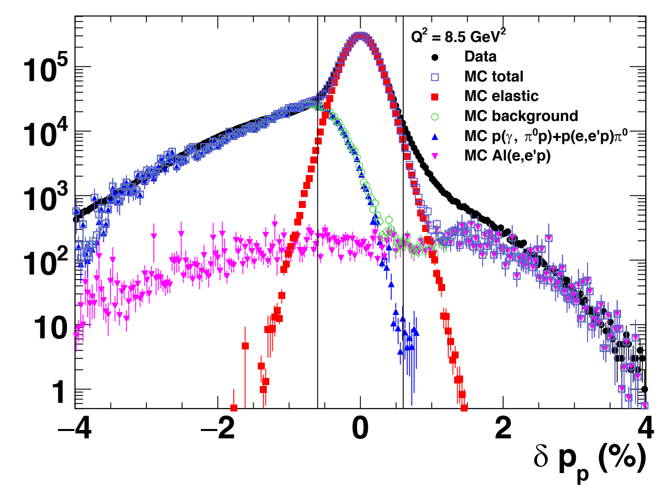

Simulated contributions to the δp_p distribution after cuts, $Q^2 = 8.5\ GeV^2$.

Inelastic Background Estimation, II

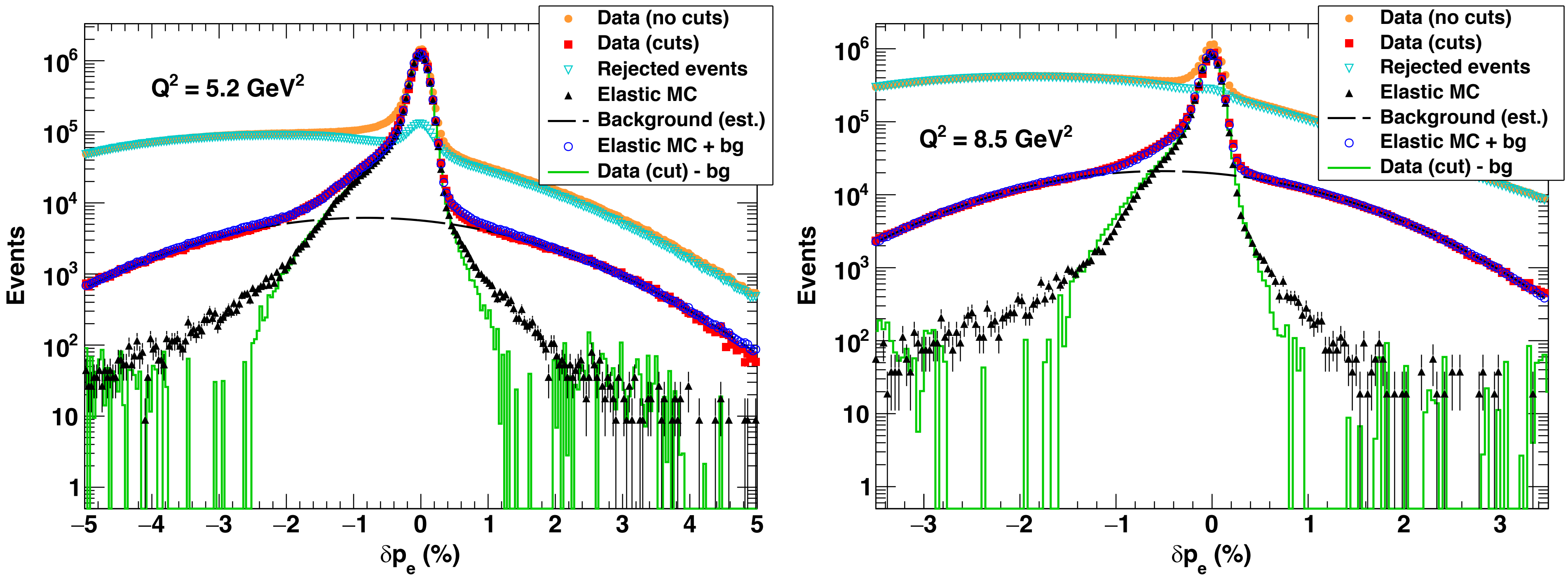

- Monte Carlo simulations of the main background processes indicate that the δp_e distribution of the background is approximately described by a smooth Gaussian in the immediate vicinity of the elastic peak.
- The final δp_e spectrum after $\delta p_p, \delta\phi$ cuts is well described by the sum of the Gaussian background and the simulated, radiatively corrected elastic *ep* yield with realistic detector acceptances and resolutions.
- In particular, after subtracting the background estimated using the Gaussian sideband method, the data agree qualitatively with the predicted shape of the (radiatively corrected) elastic peak over ~3 orders of magnitude in event yield.
- The experimental resolution of δp_e, which is dominated by the HMS momentum resolution and the BigCal coordinate resolution, is more nearly Gaussian than that of δp_p and $\delta\phi$, which are dominated by the HMS angular resolution, and therefore susceptible to significant non-Gaussian tails owing to multiple-scattering in ”S0” and the HMS drift chambers themselves, incorrect solutions of the left/right ambiguity, and other effects that are difficult to precisely model in MC.

FPP event selection criteria

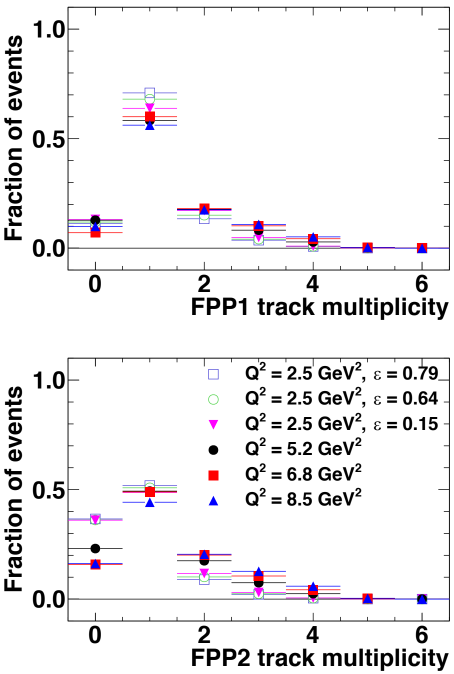

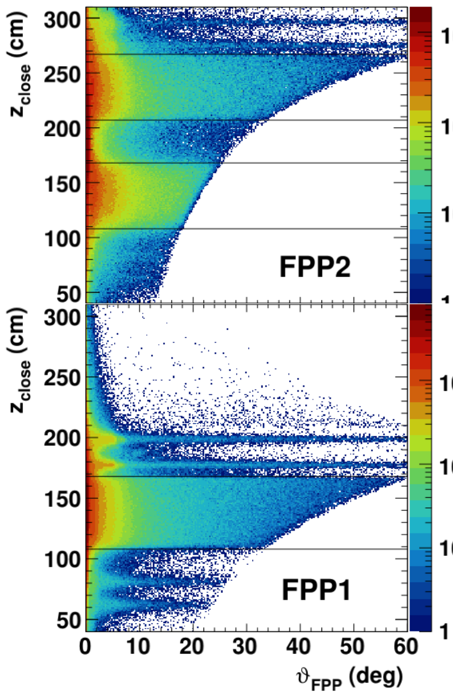

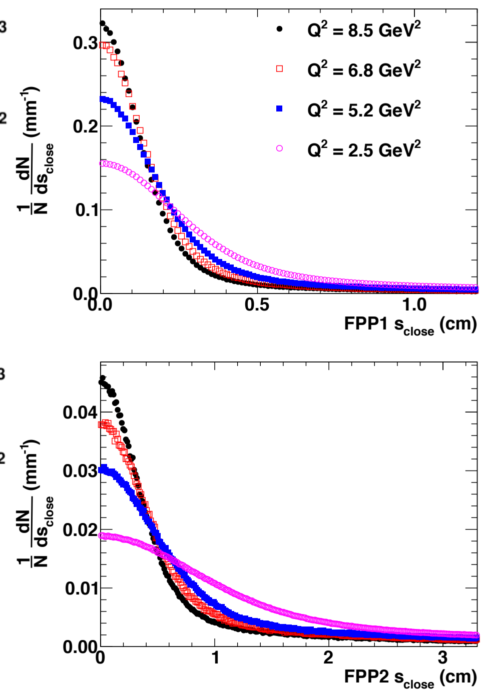

Table 1: FPP event selection criteria as a function of Q^2. Only single-track events passing the "cone test" were included in the analysis. No explicit ϑ cuts were applied. Instead, the ϑ ranges shown are the effective ranges resulting from the p_T cuts. The same criteria were applied to all three ϵ values at $Q^2 = 2.5$ GeV^2. s_{close} and z_{close} are defined, respectively, as the distance of closest approach between the incident and scattered tracks, and the z-coordinate of the point of closest approach between incident and scattered tracks, with $z = 0$ at the HMS focal plane.

Q^2 (GeV^2)	2.5	5.2	6.8	8.5
p_T^{min} (GeV/c)	0.06	0.05	0.05	0.05
p_T^{max} (GeV/c)	1.2	1.5	1.5	1.5
FPP1 ϑ_{min}^{eff}(°)	1.71	0.81	0.65	0.53
FPP1 ϑ_{max}^{eff}(°)	36.7	25.1	19.9	16.3
FPP2 ϑ_{min}^{eff}(°)	1.82	0.84	0.67	0.55
FPP2 ϑ_{max}^{eff}(°)	39.5	26.0	20.4	16.6
FPP1 s_{close}^{max} (cm)	2.2	1.7	1.4	1.2
FPP2 s_{close}^{max} (cm)	6.5	5.1	4.1	3.3
FPP1 z_{close}^{min} (cm)	108	108	108	108
FPP1 z_{close}^{max} (cm)	168	168	168	168
FPP2 z_{close}^{min} (cm)	207	207	207	207
FPP2 z_{close}^{max} (cm)	267	267	267	267

$$p_T \equiv p_p \sin\vartheta$$

- Useful events in the FPP are selected according to the following criteria:
  - Single charged track—multi-track events have low analyzing power, negligible contribution to figure-of-merit
  - Tracks must pass "cone test", requiring the projection of the cone of opening angle ϑ from the point of closest approach between incident and scattered tracks to the rearmost wire plane to be entirely contained within the FPP drift chamber active area (the z-dependent large-ϑ cutoff in the (ϑ, z_{close}) plot is due to the cone test application.
  - Distance of closest approach s_{close} between incident and scattered tracks is required to be less than a reasonable upper limit, chosen to optimize figure-of-merit
  - z_{close}, the "z" coordinate of the point of closest approach between incident and scattered tracks, must lie within the physical extent of the analyzer, with a small additional tolerance to account for detector resolution

FPP polar angle distributions

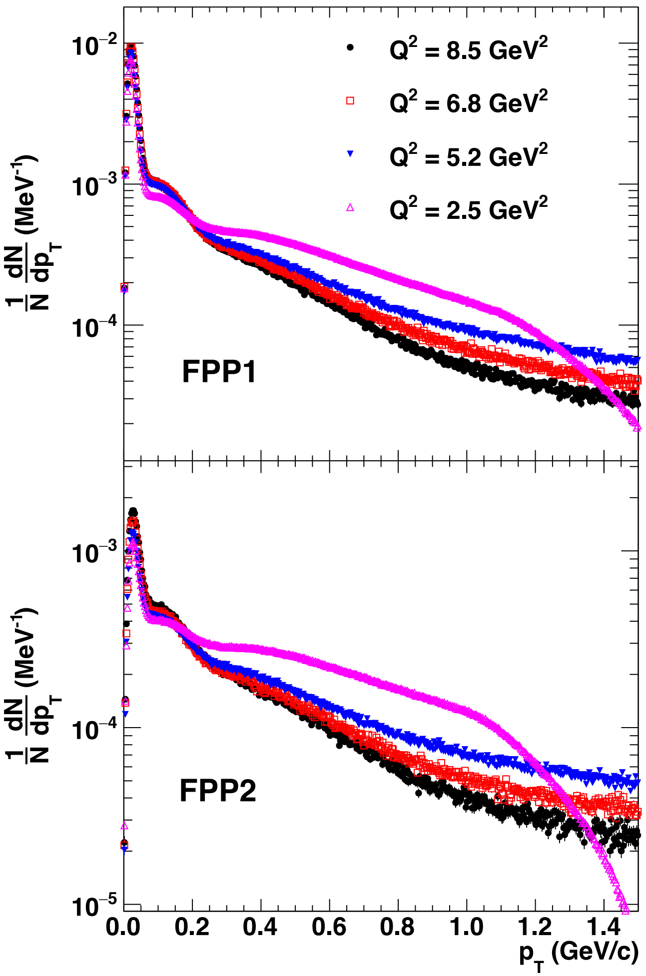

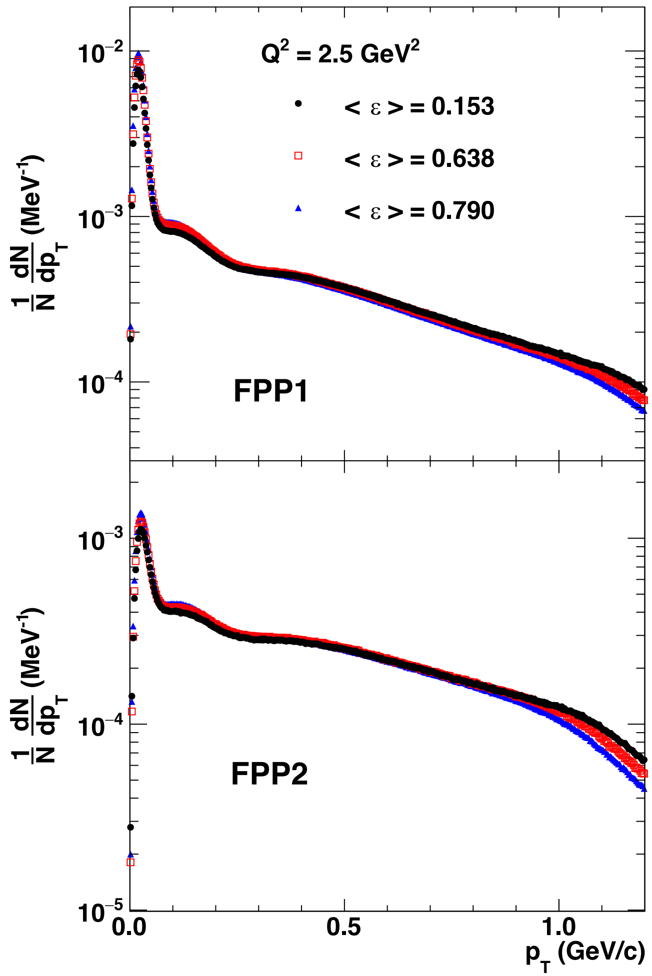

Table 1: FPP event selection criteria as a function of Q^2. Only single-track events passing the "cone test" were included in the analysis. No explicit ϑ cuts were applied. Instead, the ϑ ranges shown are the effective ranges resulting from the p_T cuts. The same criteria were applied to all three ϵ values at $Q^2 = 2.5$ GeV^2. s_{close} and z_{close} are defined, respectively, as the distance of closest approach between the incident and scattered tracks, and the z-coordinate of the point of closest approach between incident and scattered tracks, with $z = 0$ at the HMS focal plane.

Q^2 (GeV^2)	2.5	5.2	6.8	8.5
p_T^{min} (GeV/c)	0.06	0.05	0.05	0.05
p_T^{max} (GeV/c)	1.2	1.5	1.5	1.5
FPP1 ϑ_{min}^{eff} (°)	1.71	0.81	0.65	0.53
FPP1 ϑ_{max}^{eff} (°)	36.7	25.1	19.9	16.3
FPP2 ϑ_{min}^{eff} (°)	1.82	0.84	0.67	0.55
FPP2 ϑ_{max}^{eff} (°)	39.5	26.0	20.4	16.6
FPP1 s_{close}^{max} (cm)	2.2	1.7	1.4	1.2
FPP2 s_{close}^{max} (cm)	6.5	5.1	4.1	3.3
FPP1 z_{close}^{min} (cm)	108	108	108	108
FPP1 z_{close}^{max} (cm)	168	168	168	168
FPP2 z_{close}^{min} (cm)	207	207	207	207
FPP2 z_{close}^{max} (cm)	267	267	267	267

$$p_T \equiv p_p \sin\vartheta$$

- Coulomb scattering dominates for $p_T \leq 0.06$ GeV
- Analyzing power negligible for $p_T \geq 1$ GeV

- Polar scattering angle distribution *approximately* scales with proton momentum, for a given CH_2 thickness.
- At $Q^2 = 2.5\ GeV^2$, the p_T distributions are the same for all three kinematics, at the few-percent level, as expected.

FPP azimuthal asymmetries, I

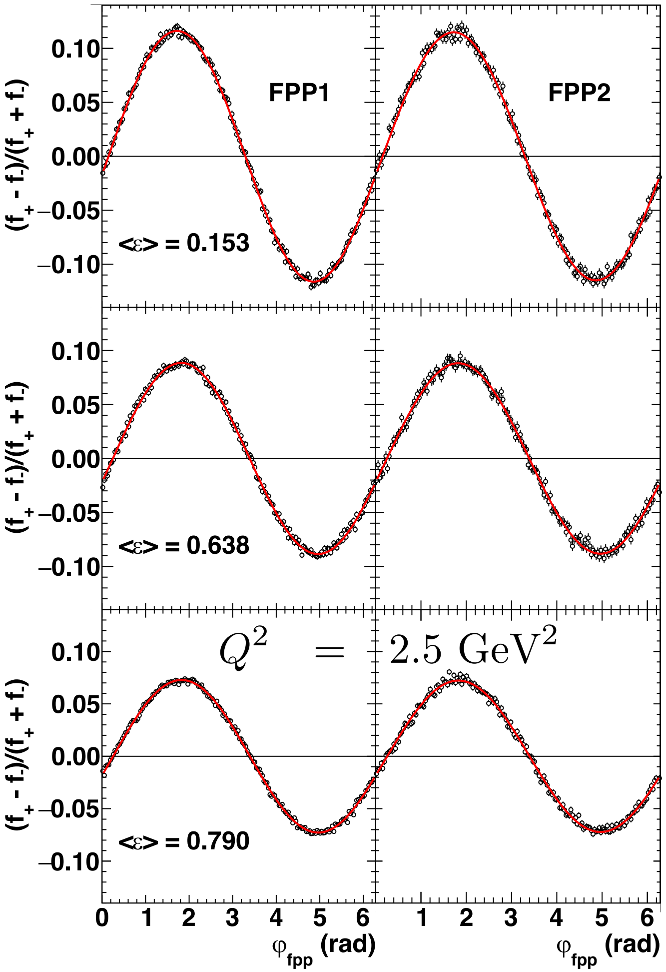

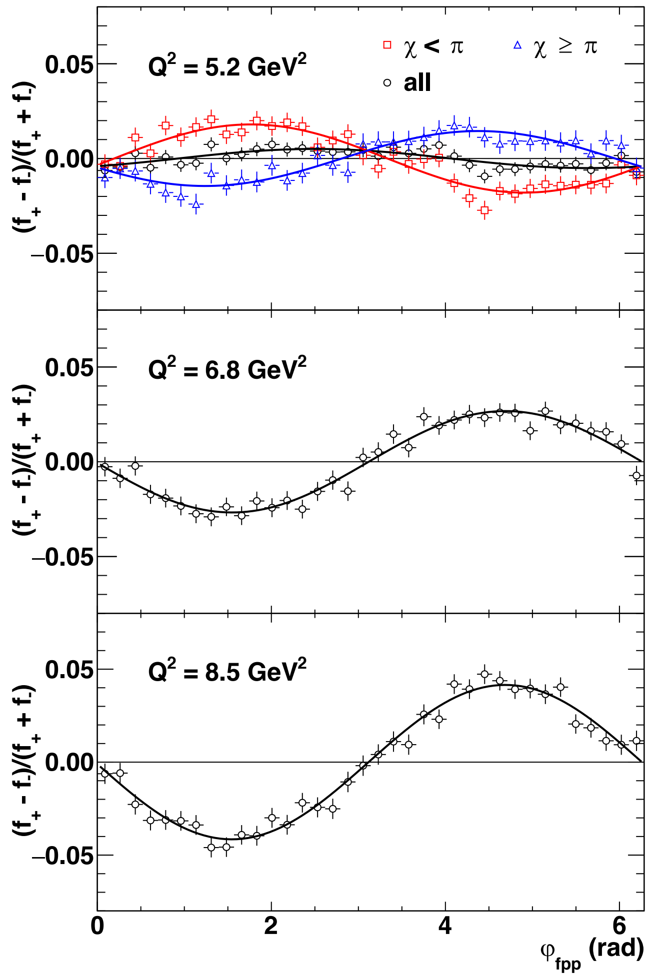

- The 30-Hz beam helicity reversal cancels the effects of FPP instrumental asymmetries due to; e.g., φ-dependence of acceptance and/or efficiency and/or angular resolution
- The resulting sinusoidal asymmetry is proportional to the effective average analyzing power of the selection of events and the incident proton's transverse polarization components.
- Only the transferred polarization components survive in the difference distribution between opposite beam helicity states
- The proton's polarization at the focal plane is related to the reaction-plane transferred polarization components P_t, P_ℓ by a rotation describing the spin transport through the HMS magnetic field.

$$\frac{f_+ - f_-}{f_+ + f_-} = \frac{\bar{A}_y \left(P_{y,tr}^{FPP} \cos\varphi - P_{x,tr}^{FPP} \sin\varphi\right)}{1 + \bar{A}_y \left(P_{y,ind}^{FPP} \cos\varphi - P_{x,ind}^{FPP} \sin\varphi\right)} \approx \bar{A}_y \left(P_{y,tr}^{FPP} \cos\varphi - P_{x,tr}^{FPP} \sin\varphi\right) \qquad (20)$$

FPP azimuthal asymmetries, II

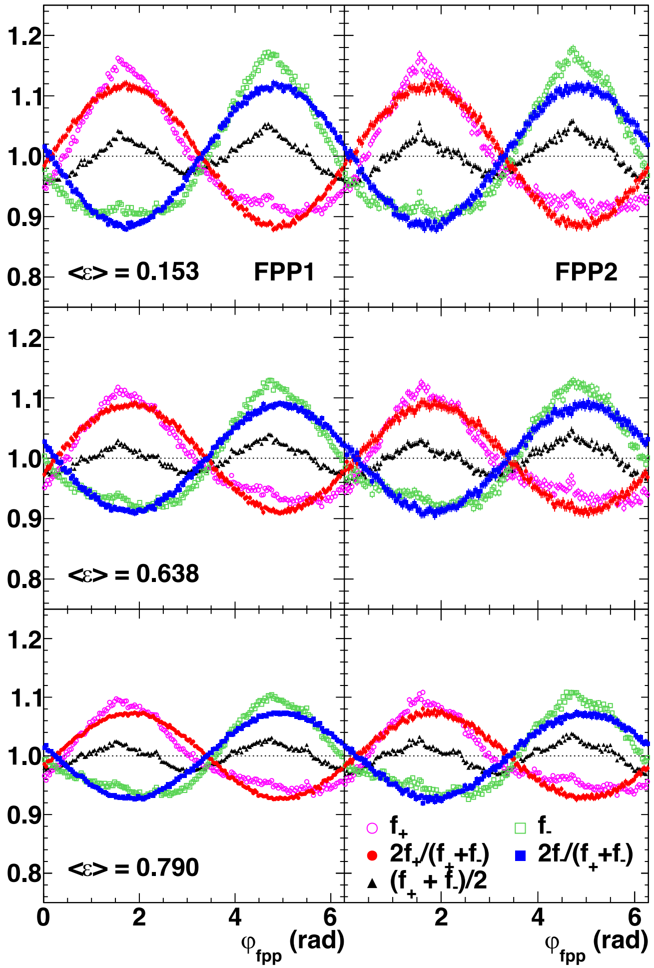

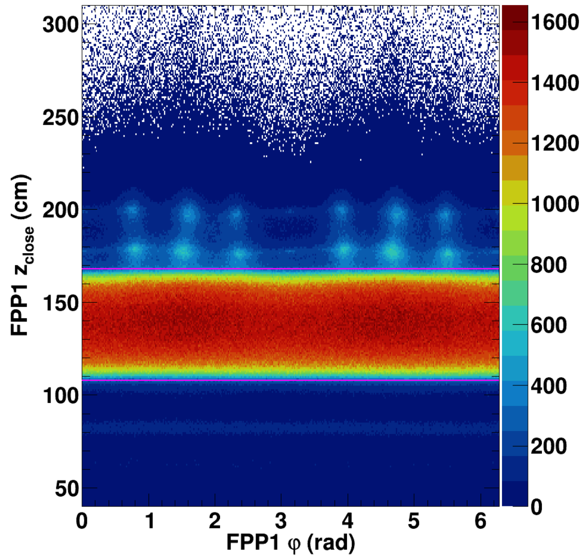

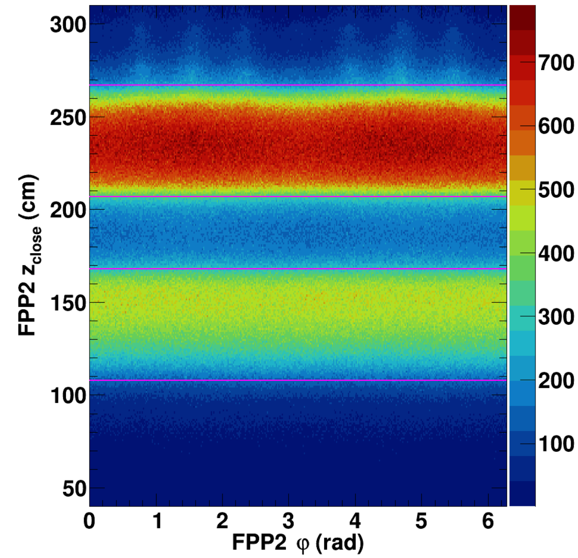

- Spurious, artificial peaks in the helicity-sum φ spectrum, at angles corresponding to FPP wire orientations, and z_{close} corresponding to the drift chamber locations, result from incorrect solutions of the left-right ambiguity (see next slide)
- These events are mostly (but not entirely) rejected by the z_{close} cuts.

$$\begin{aligned} f^+ + f^- &\equiv \frac{\pi}{\Delta\varphi}\left[\frac{N^+(\varphi)}{N_0^+} + \frac{N^-(\varphi)}{N_0^-}\right] \\ &= [1+\mu_0(\varphi)] \times \\ &\quad [1 + \bar{A}_y(P_{y,ind}^{FPP}\cos\varphi - P_{x,ind}^{FPP}\sin\varphi)] \\ &\approx 1 + \mu_0(\varphi) \qquad (19) \end{aligned}$$

$$\mu_0(\varphi) \equiv \sum_{n=1}^{\infty}\left[c_n\cos(n\varphi) + s_n\sin(n\varphi)\right]$$

$$\begin{aligned} \frac{2f_\pm}{f_+ + f_-} &= 1 \pm \frac{\bar{A}_y\left(P_{y,tr}^{FPP}\cos\varphi - P_{x,tr}^{FPP}\sin\varphi\right)}{1 + \bar{A}_y\left(P_{y,ind}^{FPP}\cos\varphi - P_{x,ind}^{FPP}\sin\varphi\right)} \\ &\approx 1 \pm \bar{A}_y\left(P_{y,tr}^{FPP}\cos\varphi - P_{x,tr}^{FPP}\sin\varphi\right) \qquad (21) \end{aligned}$$

Lesson Learned: Irreducible FPP left-right ambiguity

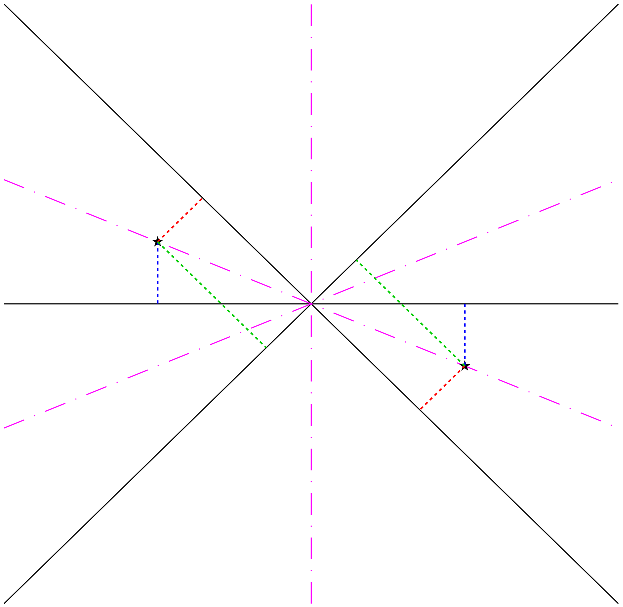

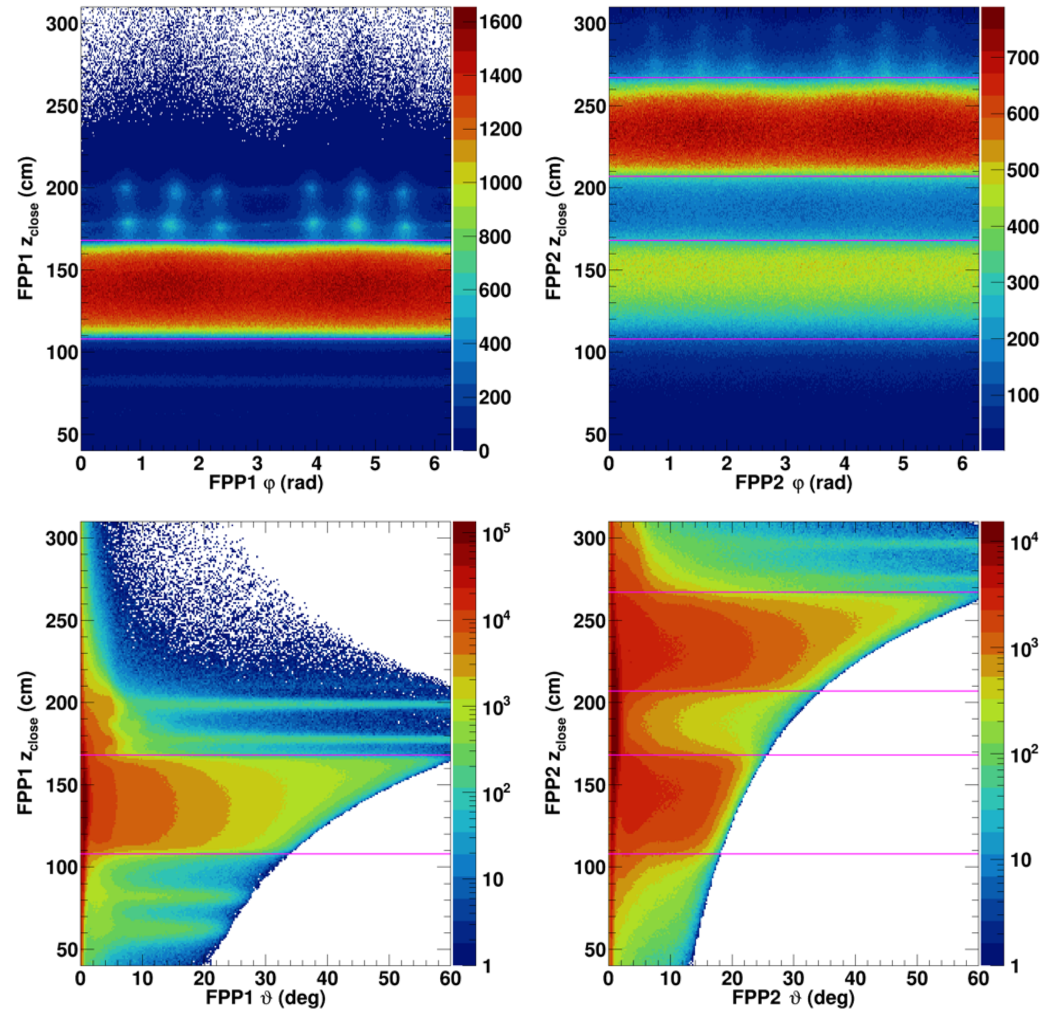

- The symmetry of wire orientations and common intersection point of U, V, X wires at chamber center leads to the existence of two solutions with (nearly) identical χ^2, with hits placed on the opposite side of all three wires firing in a given chamber, for tracks at or near normal incidence.
- Ambiguity cannot be eliminated without introducing scattering-parameter-dependent biases in the pattern recognition and track reconstruction, which is dangerous.
- Ambiguity can be eliminated (for future experiments) by adding more wire planes; e.g., operating in a single-FPP configuration with 12 tracking planes by retracting the second analyzer block, or retaining the double-FPP layout, but slightly reducing the thickness of each analyzer block and adding a third identical chamber to each FPP.

HMS Spin Transport, I

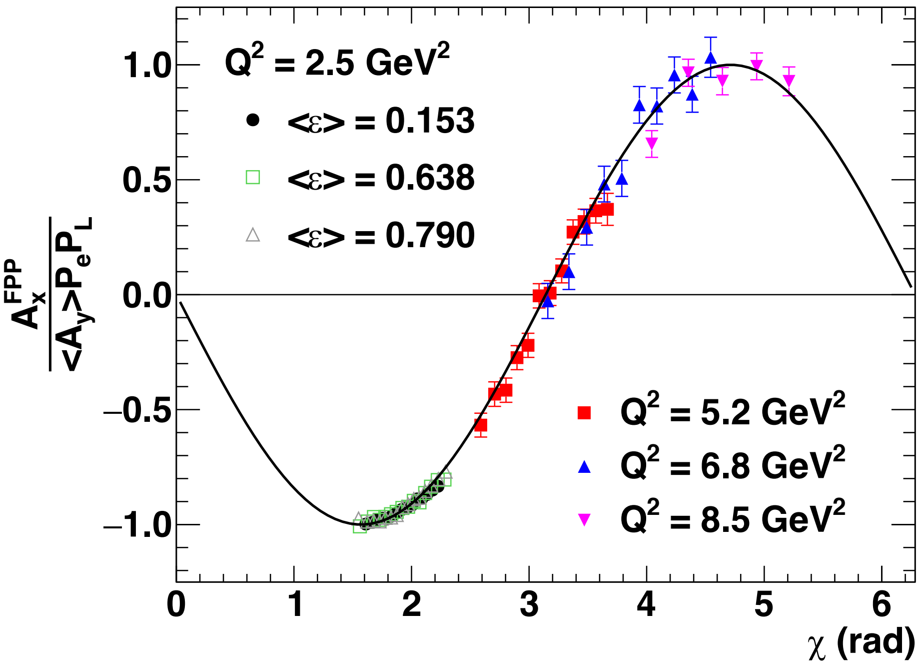

$$A_x^{FPP} \approx -\sin\chi \langle A_y \rangle P_e P_\ell$$

- The ideal dipole approximation qualitatively accounts for the acceptance-averaged behavior of the sin φ asymmetry A_x^{FPP}.
- The wide χ acceptance of the HMS provides adequate sensitivity to P_ℓ even at $Q^2 = 5.2$ GeV^2, for which the acceptance-averaged asymmetry is close to zero.

- The precession of the polarization of relativistically moving charged particles in a magnetic field is described in the lab frame by the Thomas-BMT equation: Phys. Rev. Lett. 2, 435 (1959).
- For protons, the equation can be written as:

$$\frac{d\mathbf{S}}{dt} = \frac{e}{\gamma m}\mathbf{S} \times \left(\frac{g}{2}\mathbf{B}_\parallel + \left[1 + \gamma\left(\frac{g}{2} - 1\right)\right]\mathbf{B}_\perp\right)$$

$$\frac{d\mathbf{v}}{dt} = \frac{e}{\gamma m}\mathbf{v} \times \mathbf{B}$$

- Here $B_\parallel$ and $B_\perp$ are the magnetic field components parallel and perpendicular to the proton's velocity, respectively, and g is the gyromagnetic ratio
- In the ideal dipole approximation, the proton spin component perpendicular to the HMS dipole field (which roughly coincides with P_ℓ) precesses by an angle $\chi = \gamma\kappa_p\theta_{bend}$ relative to the proton trajectory (where θ_{bend} is the trajectory bend angle), while the component parallel to the dipole field does not precess; i.e.:

$$P_y^{FPP} \approx P_t$$
$$P_x^{FPP} \approx -\sin\chi P_\ell$$

- The spin transport matrix is computed event-by-event from a detailed 5th-order COSY INFINITY model of the HMS including fringe fields.

HMS Spin Transport, II

$$
\begin{aligned}
S_{yt} &\approx \cos\chi_\phi \\
S_{y\ell} &\approx \sin\chi_\phi \\
S_{xt} &\approx \sin\chi_\phi \sin\chi \\
S_{x\ell} &\approx -\cos\chi_\phi \sin\chi
\end{aligned}
$$

$$
\begin{aligned}
\chi_\phi &\equiv \gamma\kappa_p(\phi_{fp} - \phi_{tar}) \\
&\equiv \gamma\kappa_p\phi_{bend} \\
\chi &\equiv \gamma\kappa_p\theta_{bend}
\end{aligned}
$$

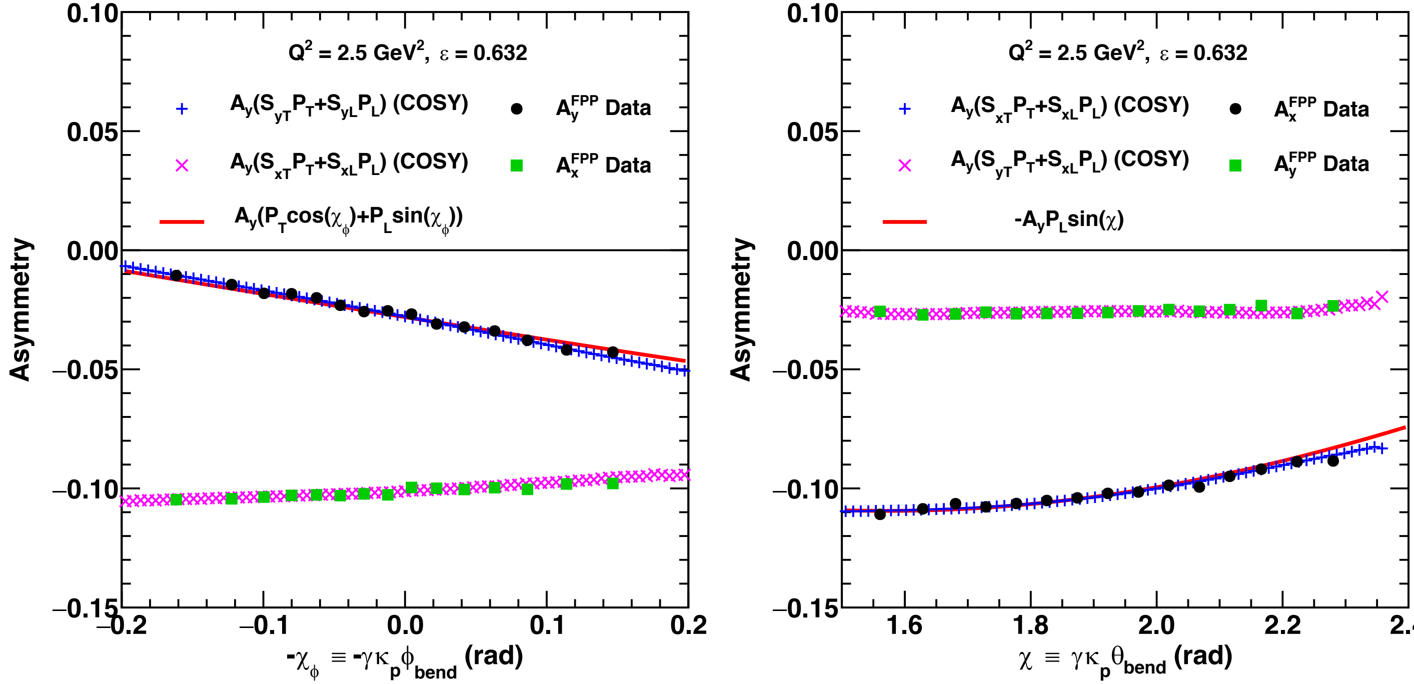

- The quadrupoles also cause the proton spin to precess in the non-dispersive (horizontal) plane, mixing P_t and P_ℓ.
- The total rotation relative to the trajectory can be approximated by the composition of a rotation by angle $\chi_\phi \equiv \gamma\kappa_p\phi_{bend}$ in the non-dispersive plane, followed by a rotation through angle χ in the dispersive (vertical) plane.
- For the HMS, the differences between this "geometric" approximation and the full COSY calculation are quite small, due to the "simple" QQQD layout of the magnets.
- The observed χ, χ_ϕ dependencies of the measured FPP asymmetries are in good agreement with COSY and the geometric approximation

FPP azimuthal asymmetry definitions:

- A_y = analyzing power
- S_{ij}'s are spin transport matrix elements

$$
\begin{aligned}
\frac{f_+(\varphi) - f_-(\varphi)}{f_+(\varphi) + f_-(\varphi)} &= A_y^{FPP}\cos\varphi - A_x^{FPP}\sin\varphi \\
A_y^{FPP} &\equiv A_y P_y^{FPP} = A_y(S_{yt}P_t + S_{y\ell}P_\ell) \\
A_x^{FPP} &\equiv A_y P_x^{FPP} = A_y(S_{xt}P_t + S_{x\ell}P_\ell)
\end{aligned}
$$

Maximum-likelihood Estimators for P_t, P_ℓ

- The transferred polarization components are extracted using an unbinned maximum-likelihood estimator, linearized by truncating the expansion of $\ln(1+x) = x - \frac{x^2}{2} + \mathcal{O}(x^3)$ at second order:

$$\begin{aligned}\mathcal{L}(P_t, P_\ell) &= \prod_{i=1}^{N_{event}} \frac{E(\varphi_i)}{2\pi}\left\{1 + h_i P_e A_y^{(i)}\left[\left(S_{yt}^{(i)} P_t^{obs} + S_{y\ell}^{(i)} P_\ell^{obs}\right)\cos\varphi_i \right.\right. \\ &\quad \left.\left. - \left(S_{xt}^{(i)} P_t^{obs} + S_{x\ell}^{(i)} P_\ell^{obs}\right)\sin\varphi_i\right]\right\}\end{aligned}$$

- Measured asymmetries are an incoherent mixture of signal (elastic) and background (inelastic) asymmetries:

$$\begin{aligned}P_t^{obs} &= (1 - f_{inel}) P_t + f_{inel} P_t^{inel} \\ P_\ell^{obs} &= (1 - f_{inel}) P_\ell + f_{inel} P_\ell^{inel}\end{aligned}$$

- The φ-dependent acceptance/efficiency/false asymmetry terms do not contribute to the linearized ML estimators:

$$E(\varphi_i) \equiv 1 + \sum_{n=1}^{\infty}\left[c_n \cos(n\varphi_i) + s_n \sin(n\varphi_i)\right]$$

- The linearized ML estimators for the transferred polarization components are given by the solution of the system of equations at right, with shorthand symbols defined below:

$$\sum_{i=1}^{N_{event}}\begin{bmatrix}\left(\lambda_t^{(i)}\right)^2 & \lambda_t^{(i)}\lambda_\ell^{(i)} \\ \lambda_t^{(i)}\lambda_\ell^{(i)} & \left(\lambda_\ell^{(i)}\right)^2\end{bmatrix}\begin{bmatrix}\hat{P}_t \\ \hat{P}_\ell\end{bmatrix} = \sum_{i=1}^{N_{event}}\begin{bmatrix}\lambda_t^{(i)}\left(1 - \lambda_{inel}^{(i)}\right) \\ \lambda_\ell^{(i)}\left(1 - \lambda_{inel}^{(i)}\right)\end{bmatrix}$$

$$\begin{aligned}\lambda_t^{(i)} &\equiv h_i P_{beam} A_y^{(i)}\left(1 - f_{inel}^{(i)}\right)\left[S_{yt}^{(i)}\cos\varphi_i - S_{xt}^{(i)}\sin\varphi_i\right] \\ \lambda_\ell^{(i)} &\equiv h_i P_{beam} A_y^{(i)}\left(1 - f_{inel}^{(i)}\right)\left[S_{y\ell}^{(i)}\cos\varphi_i - S_{x\ell}^{(i)}\sin\varphi_i\right] \\ \lambda_{inel}^{(i)} &= h_i P_{beam} A_y^{(i)} f_{inel}^{(i)}\left[\left(S_{yt}^{(i)}\cos\varphi_i - S_{xt}^{(i)}\sin\varphi_i\right)P_t^{inel} + \left(S_{y\ell}^{(i)}\cos\varphi_i - S_{x\ell}^{(i)}\sin\varphi_i\right)P_\ell^{inel}\right]\end{aligned}$$

See [Phys. Rev. C, 96, 055203 (2017)] for additional details of the formalism!

Form Factor Ratio Extraction

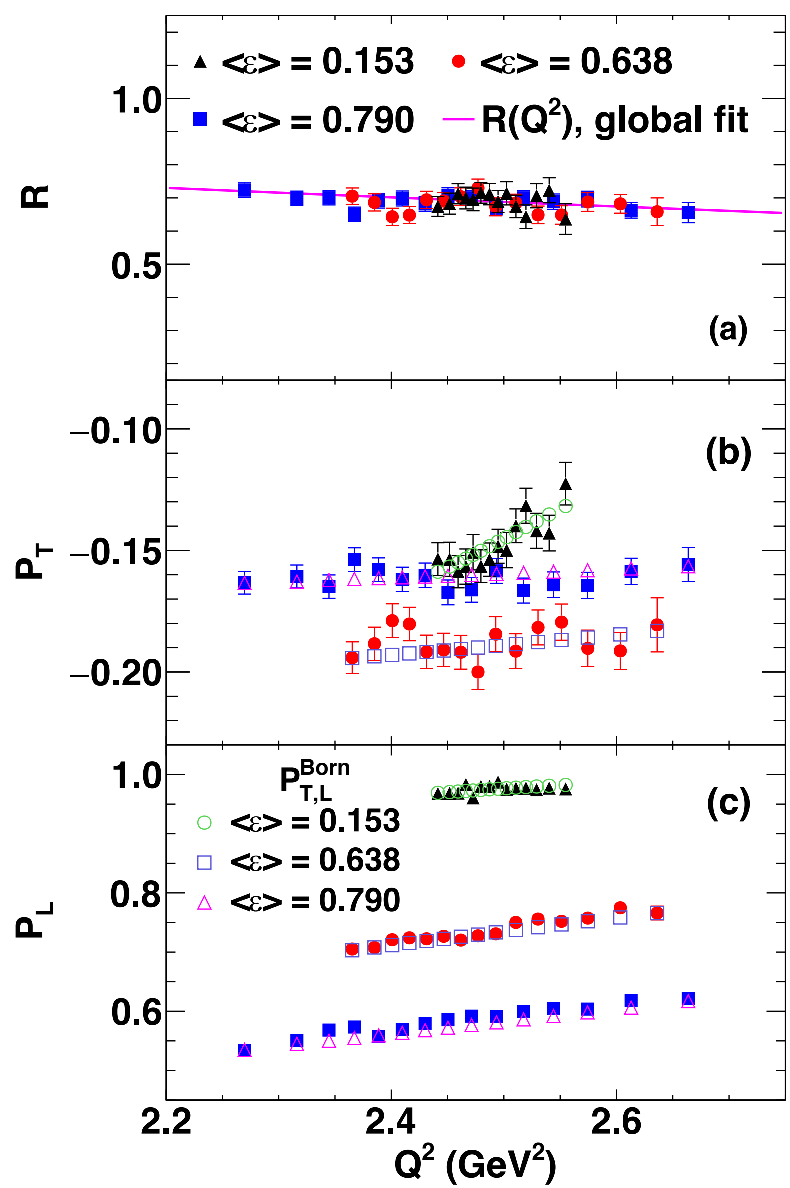

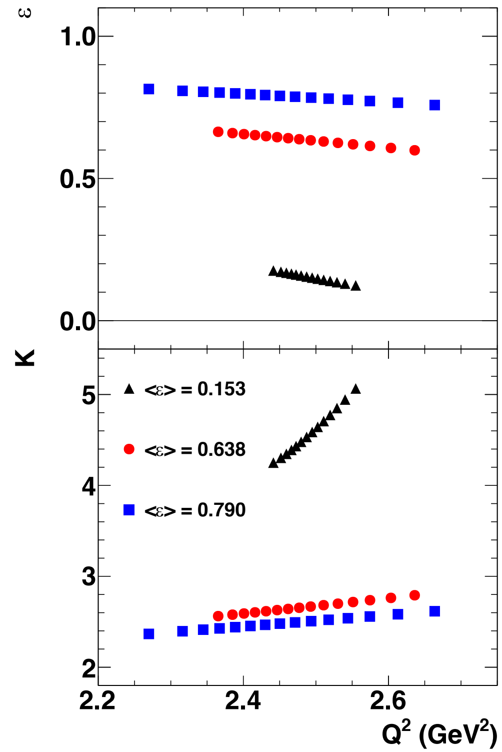

$$R = \mu_p \frac{G_E^p}{G_M^p} = -K\frac{P_t}{P_\ell}$$

$$K \equiv \mu_p \sqrt{\frac{\tau(1+\epsilon)}{2\epsilon}}$$

$$P_t = -\sqrt{\frac{2\epsilon(1-\epsilon)}{\tau}}\frac{r}{1+\frac{\epsilon}{\tau}r^2}$$

$$P_\ell = \frac{\sqrt{1-\epsilon^2}}{1+\frac{\epsilon}{\tau}r^2}$$

- P_t, P_ℓ vary significantly within the HMS acceptance for each kinematic at 2.5 GeV^2, even assuming validity of the Born approximation.
- R varies more slowly within the acceptance than P_t or P_ℓ individually.
- To within experimental precision, P_t, P_ℓ, and R vary linearly with Q^2 within the acceptance, such that the acceptance-averaged results of the unbinned ML analysis are valid at the acceptance-averaged kinematics.
- Q^2-dependence of the PT observables within the acceptance is consistent with Born approximation at 2.5 GeV^2.

Analyzing Power Calibration

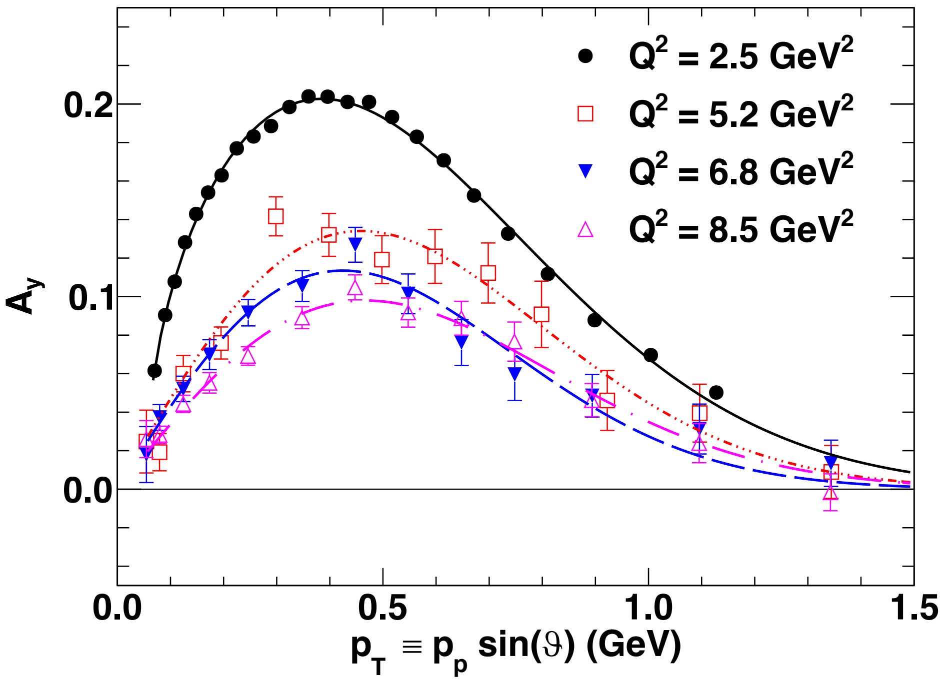

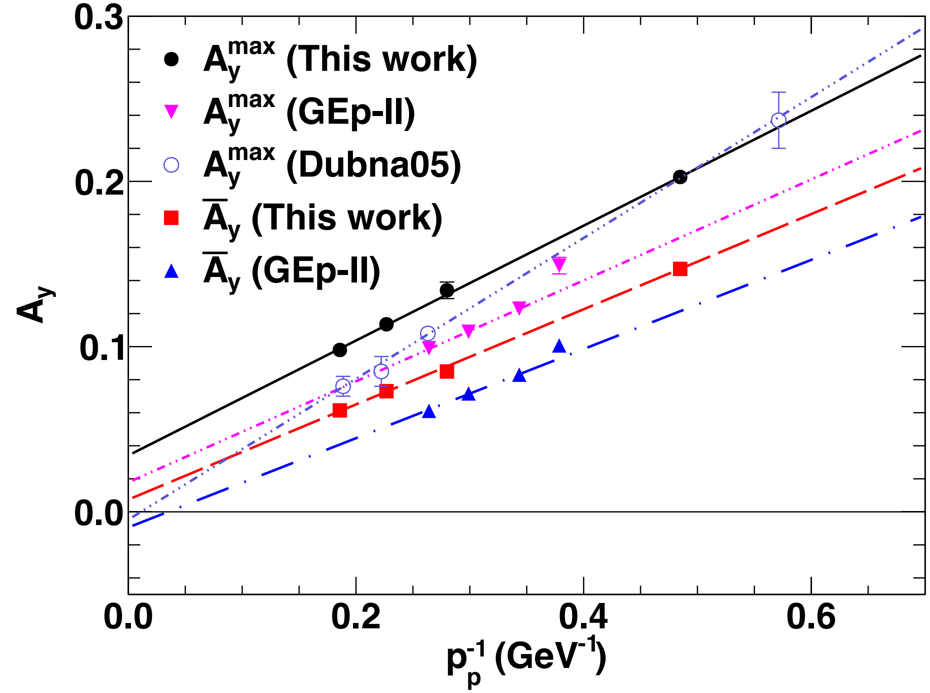

$$\hat{P}_t^{(A_y=1)} = \bar{A}_y P_t$$

$$\hat{P}_\ell^{(Ay=1)} = \bar{A}_y P_\ell$$

$$\bar{A}_y = \frac{\hat{P}_t^{(A_y=1)}}{P_t^{Born}} = \frac{\hat{P}_\ell^{(A_y=1)}}{P_\ell^{Born}}$$

$$A_y(p_p, p_T) = A_y^0(p_T)\frac{\bar{p_p}}{p_p},$$

- The analyzing power distribution in terms of $p_T = p_p \sin\vartheta$ is roughly Q^2-independent, up to an overall normalization constant, with a maximum at $p_T \approx 0.4$ GeV.
- Both the maximum and the average (for equivalent p_T ranges) analyzing power scale as p_p^{-1}.
- The analyzing power momentum dependence is corrected for event-by-event assuming an overall p_p^{-1} scaling, independent of ϑ.
- Hall C FPP effective A_y significantly exceeds that of other experiments using CH_2. This is attributable to the capability to isolate true single-track events, absent from Hall A and Dubna measurements

Inelastic Background Subtraction

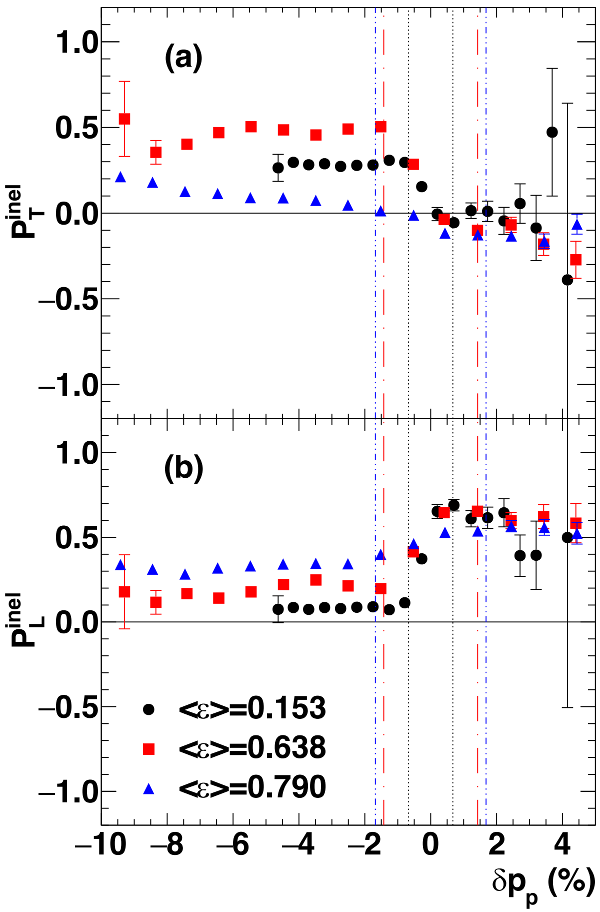

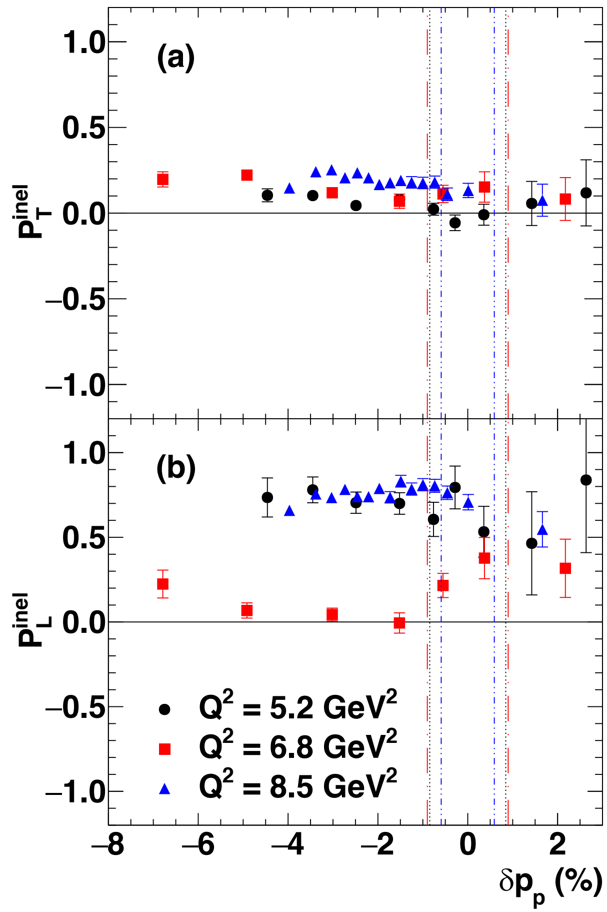

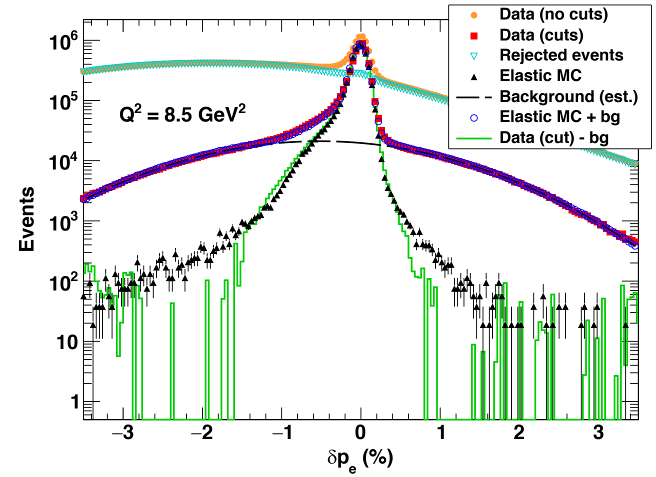

TABLE IV. (color online) Estimated fractional background contamination $f \equiv \frac{B}{S+B}$ (where B and S refer to the background and the signal, respectively) within the final, $\pm 3\sigma$ cut region of the δp_e distribution, for all the kinematics of the GEp-III and GEp-2γ experiments. The estimates shown are obtained after applying $\pm 3\sigma$ cuts to δp_p and $\delta\phi$. The quoted uncertainties are statistical only. The quoted beam energy E_e is the value from Table I, which is averaged over the duration of the running period, and *not* corrected for energy loss in the LH_2 target.

Q^2 (GeV^2)	E_e (GeV)	$(f \pm \Delta f_{stat})$ (%)
2.5	1.873	0.435 ± 0.002
2.5	1.868	0.512 ± 0.001
2.5	2.847	0.161 ± 0.002
2.5	3.548	0.198 ± 0.002
2.5	3.680	0.208 ± 0.001
5.2	4.052	1.018 ± 0.004
6.8	5.711	0.748 ± 0.004
8.5	5.712	4.89 ± 0.01

$$P_t^{obs} = (1 - f_{inel})P_t + f_{inel}P_t^{inel}$$
$$P_\ell^{obs} = (1 - f_{inel})P_\ell + f_{inel}P_\ell^{inel}$$

- The δp_p dependence of $f_{inel}, P_t^{inel}, P_\ell^{inel}$, are taken into account event-by-event in the ML analysis

TABLE VIII. Inelastic background corrections to P_t, P_ℓ, and R. Systematic uncertainties associated with the background correction are discussed in Ref. [52].

Q^2 (GeV^2)	$\langle\epsilon\rangle$	ΔP_t	ΔP_ℓ	ΔR
2.5	0.153	-0.0013	0.0024	0.0043
2.5	0.638	-0.0008	0.0005	0.0023
2.5	0.790	-0.0002	0.0002	0.0007
5.2	0.382	-0.0010	0.0015	0.0043
6.8	0.519	-0.0009	0.0030	0.0036
8.5	0.243	-0.0060	0.0096	0.0419

- Background transferred polarizations are extracted from the rejected events using the analyzing power obtained from the elastic events.

Radiative Corrections

TABLE IX. Estimated model-independent relative radiative corrections to $R = \mu_p G_E^p / G_M^p$ and the longitudinal transferred polarization component P_ℓ, calculated using the approach described in Ref. [65]. Note that a negative (positive) value for the radiative correction as presented below implies a positive (negative) correction to obtain the Born value from the measured value for the observable in question. These corrections have *not* been applied to the final results shown in Tables X and XI. See text for details.

Q^2 (GeV^2)	E_e (GeV)	$u_{\max}$ (GeV^2)	$\frac{R_{obs}}{R_{\text{Born}}} - 1$	$\frac{P_\ell^{obs}}{P_\ell^{\text{Born}}} - 1$
2.5	1.87	0.03	-1.4×10^{-3}	1.2×10^{-4}
2.5	2.848	0.08	-2.8×10^{-4}	6.2×10^{-4}
2.5	3.548	0.1	-1.6×10^{-4}	8.3×10^{-4}
2.5	3.680	0.1	-1.5×10^{-4}	8.4×10^{-4}
5.2	4.052	0.08	-5.0×10^{-4}	2.2×10^{-4}
6.8	5.710	0.12	-3.3×10^{-4}	3.2×10^{-4}
8.5	5.712	0.1	-8.0×10^{-4}	1.3×10^{-4}

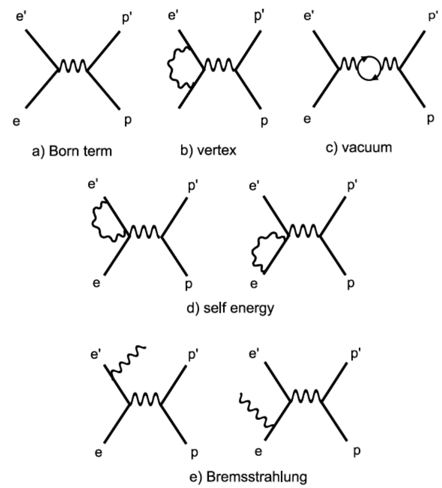

Figure 24: Born term and lowest order radiative correction graphs for the electron in elastic ep.

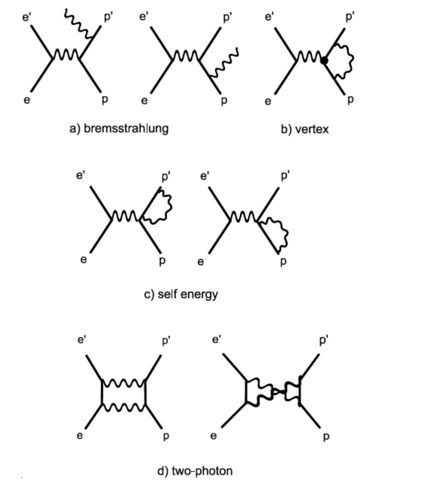

Figure 25: Lowest order radiative correction for the proton side in elastic ep scattering.

- The "standard", model-independent $\mathcal{O}(\alpha)$ radiative corrections (RC) to polarization observables in elastic *ep* scattering have been developed in, e.g., Phys. Rev. D 64, 113009 (2001), **Phys. Lett. B 514, 269 (2001),** Phys. Rev. D 65,013006(2001), and also Comput. Phys. Commun. 183,1448(2012)
- Polarization asymmetries, being ratios of spin-dependent and spin-averaged cross sections, tend to experience smaller RC than unpolarized cross sections, as the factorized, virtual terms of the RC cross section tend to partially or wholly cancel in the expression for the *relative* RC to the asymmetries.
- Elastic event selection cuts applied in GEp-III/GEp-2γ strongly suppress Bremsstrahlung corrections to asymmetries.
- Model-independent RC to the FF ratio are very small and found to be negative; corrections to the ratio P_ℓ / P_ℓ^{Born} are comparable in magnitude and positive.
- These corrections have not been applied to the final results.

Final Systematic Uncertainties—Ratio R

Table 3: Systematic uncertainty contributions for $R = -K\frac{P_t}{P_\ell} = \mu_p \frac{G_E^p}{G_M^p}$. The total systematic uncertainty includes the effects of partial correlations among the various systematic contributions, including $\Delta\phi_{tar}$ and Δy_{tar} (correlation coefficient $\rho_{\Delta\phi\Delta y} \approx -0.43$), and $\Delta\theta_{tar}$ and $\Delta\delta$ (correlation coefficient $\rho_{\Delta\theta\Delta\delta} \approx +0.26$). ΔR_{syst}^{total} is the total systematic uncertainty, while ΔR_{syst}^{ptp} is the "point-to-point" systematic uncertainty for $Q^2 = 2.5$ GeV^2 *relative* to the $\epsilon = 0.79$ setting.

Nominal Q^2 (GeV^2)	2.5	2.5	2.5	5.2	6.8	8.5
$\langle\epsilon\rangle$	0.153	0.638	0.790	0.38	0.52	0.24
$\frac{dR}{d\phi_{tar}}\Delta\phi_{tar}$	-3.4×10^{-3}	-2.1×10^{-3}	-2.0×10^{-3}	-4.8×10^{-3}	-5.7×10^{-3}	-0.010
$\frac{dR}{dy_{tar}}\Delta y_{tar}$	-2.0×10^{-3}	-1.2×10^{-3}	-1.2×10^{-3}	-2.9×10^{-3}	-3.9×10^{-3}	-7.7×10^{-3}
$\frac{dR}{d\theta_{tar}}\Delta\theta_{tar}$	-2.2×10^{-3}	-2.5×10^{-3}	-2.5×10^{-3}	1.4×10^{-3}	-5.0×10^{-3}	3.0×10^{-3}
$\frac{dR}{d\delta}\Delta\delta$	5.8×10^{-3}	1.2×10^{-3}	9.0×10^{-4}	1.2×10^{-3}	-3.3×10^{-6}	2.5×10^{-4}
$\frac{dR}{d\varphi_{FPP}}\Delta\varphi_{FPP}$	4.1×10^{-3}	2.5×10^{-3}	2.4×10^{-3}	4.6×10^{-4}	-6.0×10^{-3}	-0.017
$\frac{dR}{dE_e}\Delta E_e$	-1.8×10^{-3}	-1.1×10^{-4}	-5.6×10^{-5}	-1.9×10^{-4}	-8.3×10^{-5}	-1.4×10^{-4}
ΔR_{syst}(background)	3.5×10^{-4}	9.6×10^{-5}	9.9×10^{-5}	2.4×10^{-3}	1.6×10^{-3}	0.012
ΔR_{syst}^{total}	7.9×10^{-3}	4.0×10^{-3}	3.9×10^{-3}	5.5×10^{-3}	9.7×10^{-3}	0.024
ΔR_{syst}^{ptp}	4.3×10^{-3}	2.3×10^{-4}	1.1×10^{-4}	N/A	N/A	N/A

- Final systematic uncertainties for the FF ratio are somewhat reduced relative to the original (PRL) publications, owing largely to the more careful/thorough analysis of the non-dispersive-plane optics of the HMS, reducing the uncertainty of the total bend angle $\phi_{bend} = \phi_{fp} - \phi_{tar}$ to $\Delta\phi_{bend} = \pm 0.14$ mrad.
- Partial correlations between uncertainties in $\Delta\phi_{tar}, \Delta y_{tar}$ and $\Delta\theta_{tar}, \Delta\delta$ are now accounted for in the final systematics.
- Most systematic contributions for R are strongly correlated between the three ϵ values at 2.5 GeV^2. Same HMS momentum setting implies same spin transport, FPP analyzing power, scattering angle reconstruction systematics, etc.

Final Systematic Uncertainties--P_ℓ/P_ℓ^{Born}

Table 4: Systematic uncertainty contributions for P_ℓ and the ratio P_ℓ/P_ℓ^{Born} at $Q^2 = 2.5$ GeV^2. The point-to-point systematic uncertainty is calculated *relative* to the $\langle\epsilon\rangle = 0.153$ setting. The total systematic uncertainties in P_ℓ do not include the global uncertainty of $\Delta P_e \approx 1\%$ in the beam polarization measurement. This is because any global overestimation (underestimation) of P_e is exactly compensated by an equal and opposite underestimation (overestimation) of the polarimeter analyzing power A_y. See text for details.

Q^2 (GeV^2)	2.5	2.5	2.5
$\langle\epsilon\rangle$	0.153	0.638	0.790
$\frac{dP_\ell}{d\phi_{bend}}\Delta\phi_{bend}$	1.3×10^{-4}	1.6×10^{-4}	1.3×10^{-4}
$\frac{dP_\ell}{d\theta_{bend}}\Delta\theta_{bend}$	4.2×10^{-3}	3.2×10^{-3}	2.5×10^{-3}
$\frac{dP_\ell}{dy_{tar}}\Delta y_{tar}$	8×10^{-5}	9×10^{-5}	8×10^{-5}
$\frac{dP_\ell}{d\delta}\Delta\delta$	-2.5×10^{-4}	-1.8×10^{-4}	-1.4×10^{-4}
$\frac{dP_\ell}{d\varphi_{FPP}}\Delta\varphi_{FPP}$	-1.6×10^{-4}	-2.0×10^{-4}	-1.7×10^{-4}
ΔP_ℓ (background)	8×10^{-5}	3×10^{-5}	2×10^{-5}
$\frac{dP_\ell}{dA_y}\Delta A_y$	N/A	-1.5×10^{-3}	-1.2×10^{-3}
$\frac{dP_\ell}{dP_e}\Delta P_e$	N/A	-3.7×10^{-3}	-2.9×10^{-3}
Total ΔP_ℓ^{syst}	4.2×10^{-3}	5.1×10^{-3}	4.0×10^{-3}
Total $\Delta_{syst}\left(\frac{P_\ell}{P_\ell^{Born}}\right)$	N/A	7.0×10^{-3}	7.1×10^{-3}
$\Delta_{syst}^{ptp}\left(\frac{P_\ell}{P_\ell^{Born}}\right)$	N/A	5.3×10^{-3}	6.1×10^{-3}

- For more details of systematic uncertainty evaluation, see https://arxiv.org/abs/1707.07750 (NIM technical note forthcoming).

Results

GEp-III final results

TABLE X. Final results of the GEp-III experiment. These results supersede the originally published results from Ref. [31]. The central Q^2 value is defined by the HMS central momentum setting. The average beam energy $\langle E_{\text{beam}} \rangle$ is the result of correcting the incident beam energy event by event for the mean energy loss in the target materials upstream of the reconstructed interaction vertex. The kinematics of each setting are described by the average, rms deviation from the mean, and total accepted range of Q^2 and ϵ. The ratio $R = \mu_p G_E^p / G_M^p$ is quoted with its statistical and total systematic uncertainty. The polarization transfer components P_t and P_ℓ are quoted with their statistical uncertainties to illustrate the relative statistical precision with which the two components are simultaneously measured.[a] The quoted values of P_t and P_ℓ are the maximum-likelihood estimators obtained after calibrating the analyzing power at each Q^2 as in Sec. III B 7. The value of P_ℓ^{Born} is quoted with its statistical uncertainty, which is due solely to the uncertainty in R. $\rho(P_t, P_\ell)$ is the correlation coefficient between P_t and P_ℓ resulting from the maximum-likelihood analysis. See text for details.

Central Q^2 (GeV^2)	5.200	6.800	8.537
$\langle E_{\text{beam}} \rangle$ (GeV)	4.049	5.708	5.710
$\langle Q^2 \rangle \pm \Delta Q^2_{rms}$ (GeV^2)	5.17 ± 0.12	6.70 ± 0.19	8.49 ± 0.17
$(Q^2_{min}, Q^2_{\max})$ (GeV^2)	(4.90,5.47)	(6.20,7.21)	(8.14,8.87)
$\langle \epsilon \rangle \pm \Delta \epsilon_{rms}$	0.382 ± 0.026	0.519 ± 0.027	0.243 ± 0.028
$(\epsilon_{min}, \epsilon_{\max})$	(0.32,0.44)	(0.45,0.59)	(0.18,0.30)
$R \pm \Delta R_{\text{stat}} \pm \Delta R_{\text{syst}}$ (final)	$0.448 \pm 0.060 \pm 0.006$	$0.348 \pm 0.105 \pm 0.010$	$0.145 \pm 0.175 \pm 0.024$
$P_t \pm \Delta_{\text{stat}} P_t$	-0.090 ± 0.012	-0.063 ± 0.019	-0.020 ± 0.024
$P_\ell \pm \Delta_{\text{stat}} P_\ell$	0.918 ± 0.034	0.842 ± 0.027	0.970 ± 0.026
$P_\ell^{\text{Born}} \pm \Delta_{\text{stat}} P_\ell^{\text{Born}}$	0.918 ± 0.002	0.851 ± 0.002	0.970 ± 0.001
$\rho(P_t, P_\ell)$	-0.167	-0.076	0.052

[a]The difference between the absolute statistical errors ΔP_t and ΔP_ℓ is entirely explained by spin precession.

- No significant changes in GEp-III data relative to original publication (Phys. Rev. Lett. 104, 242301 (2010)), except that the FF ratio statistical uncertainty is reduced from 0.066 → 0.060 at $Q^2 = 5.2\ GeV^2$. This is a consequence of having neglected the covariance term between P_t and P_ℓ in the originally published statistical uncertainties.

GEp-III Final Results

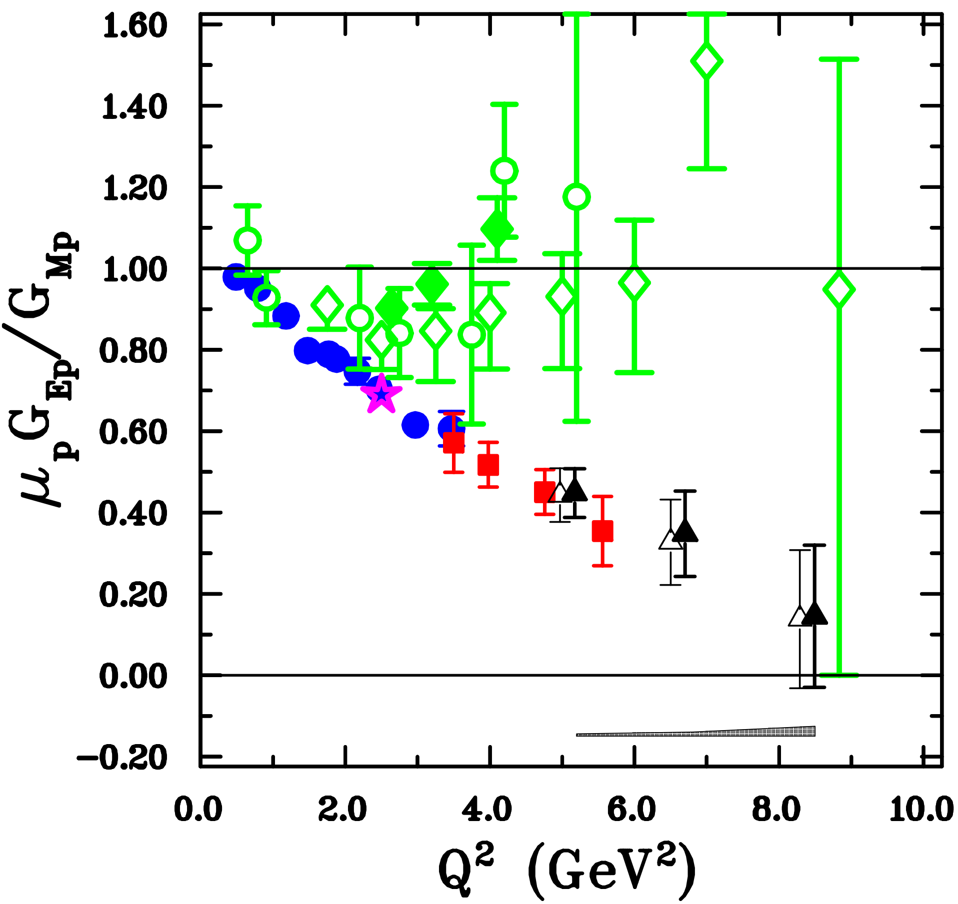

GEp-III final results (Phys. Rev. C 95, 055203 (2017)), compared to original publication (Phys. Rev. Lett. 104, 242301 (2010))

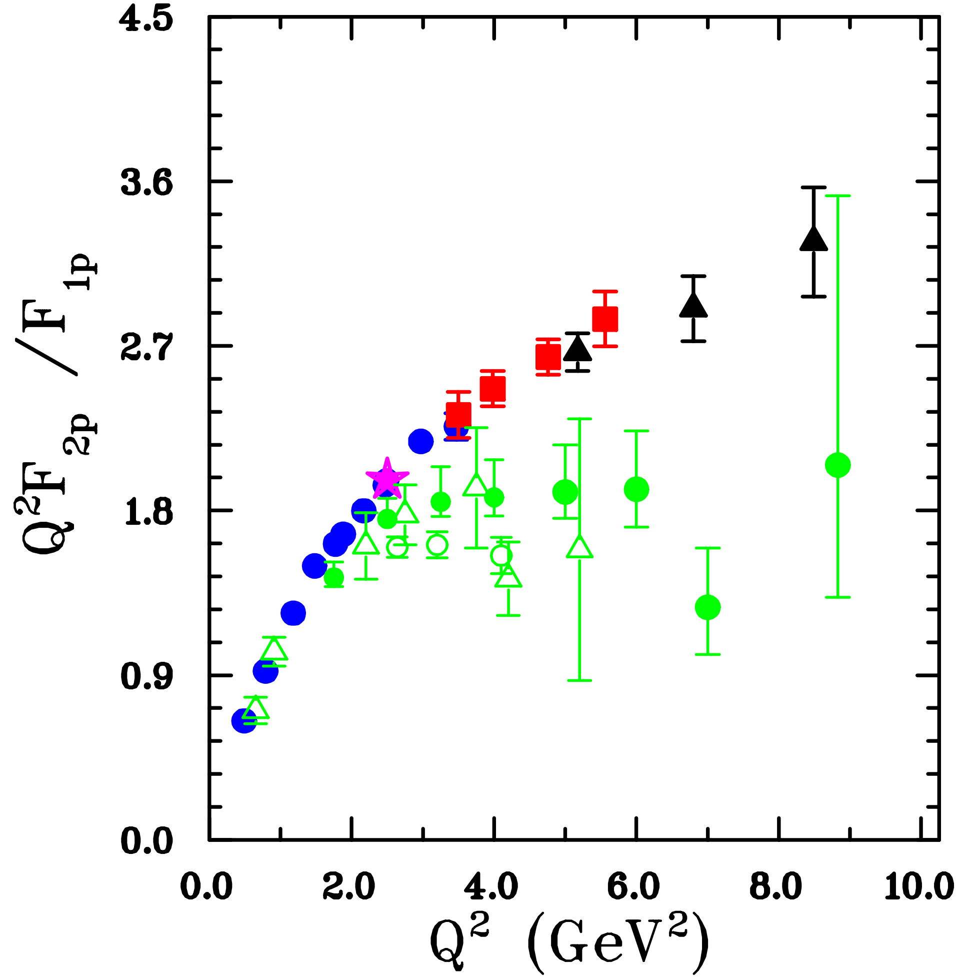

GEp-III final results plotted as $Q^2F_2^p/F_1^p$.

GEp-2γ final results

TABLE XI. Final results of the GEp-2γ experiment. These results supersede the originally published results from Ref. [47]. Average kinematics and ranges are defined as in Table X. The central ϵ value corresponds to the average beam energy and the central Q^2 of 2.5 GeV^2. The results at $\langle\epsilon\rangle = 0.790$ are obtained by combining the data collected at $E_e = 3.549$ GeV and $E_e = 3.680$ GeV (see Table I) and analyzing them together as a single setting, which is justified by the very similar acceptance-averaged values of Q^2 and ϵ at these two energies. The acceptance-averaged values of the ratio $R \equiv -\mu_p \frac{P_t}{P_\ell}\sqrt{\frac{\tau(1+\epsilon)}{2\epsilon}}$ and the longitudinal polarization transfer component P_ℓ are quoted with statistical and total systematic uncertainties. R_{bcc} is the "bin-centering-corrected" value of R at the central Q^2 of 2.5 GeV^2 (see Table XII and discussion in Sec. IV B). P_t is quoted with its statistical uncertainty only.[a] The total systematic uncertainty in P_ℓ is dominated by the beam polarization measurement. The point-to-point systematic uncertainties are defined relative to $\epsilon = 0.790(0.153)$ for $R(P_\ell/P_\ell^{\rm Born})$. $\rho(P_t, P_\ell)$ is the correlation coefficient between P_t and P_ℓ resulting from the maximum-likelihood analysis. See text for details.

Central Q^2 (GeV^2)	2.500	2.500	2.500
Central ϵ	0.149	0.632	0.783
$\langle E_{\rm beam}\rangle$ (GeV)	1.867	2.844	3.632
$\langle Q^2\rangle \pm \Delta Q^2_{rms}$ (GeV^2)	2.491 ± 0.032	2.477 ± 0.074	2.449 ± 0.105
$(Q^2_{\rm min}, Q^2_{\rm max})$ (GeV^2)	(2.42,2.58)	(2.33,2.68)	(2.18,2.75)
$\langle\epsilon\rangle \pm \Delta\epsilon_{rms}$	0.153 ± 0.015	0.638 ± 0.018	0.790 ± 0.017
$(\epsilon_{\rm min}, \epsilon_{\rm max})$	(0.11,0.19)	(0.59,0.67)	(0.73,0.83)
$R \pm \Delta R_{\rm stat} \pm \Delta R^{\rm total}_{\rm syst}$ (final)	$0.6953 \pm 0.0091 \pm 0.0079$	$0.6809 \pm 0.0070 \pm 0.0040$	$0.6915 \pm 0.0059 \pm 0.0039$
$\Delta R^{ptp}_{\rm syst}$ (cf. $\langle\epsilon\rangle = 0.790$)	0.0043	0.0002	0.0001
$R_{bcc} \pm \Delta_{\rm stat} R_{bcc}$	0.6940 ± 0.0091	0.6776 ± 0.0070	0.6837 ± 0.0059
$P_t \pm \Delta_{\rm stat} P_t$	-0.1481 ± 0.0019	-0.1881 ± 0.0019	-0.1622 ± 0.0013
$P_\ell \pm \Delta_{\rm stat} P_\ell \pm \Delta^{\rm total}_{\rm syst} P_\ell$	$0.9750 \pm 0.0020 \pm 0.0042$	$0.7335 \pm 0.0020 \pm 0.0051$	$0.5816 \pm 0.0014 \pm 0.0040$
$P_\ell^{\rm Born} \pm \Delta_{\rm stat} P_\ell^{\rm Born}$	0.9753 ± 0.0003	0.7295 ± 0.0008	0.5720 ± 0.0006
$\frac{P_\ell}{P_\ell^{\rm Born}} \pm \Delta_{\rm stat}(\frac{P_\ell}{P_\ell^{\rm Born}}) \pm \Delta^{\rm total}_{\rm syst}(\frac{P_\ell}{P_\ell^{\rm Born}})$	N/A	$1.0055 \pm 0.0029 \pm 0.0070$	$1.0167 \pm 0.0027 \pm 0.0071$
$\Delta^{ptp}_{\rm syst}(\frac{P_\ell}{P_\ell^{\rm Born}})$ (cf. $\langle\epsilon\rangle = 0.153$)	N/A	0.0053	0.0061
$\rho(P_t, P_\ell)$	0.019	0.009	0.006

[a]As in Table X, the quoted values of P_t and P_ℓ correspond to the maximum-likelihood estimators obtained using the results of the analyzing power calibration of Sec. III B 7, performed at $\langle\epsilon\rangle = 0.153$ under the assumption $P_\ell = P_\ell^{\rm Born}$ and applied to all three kinematic settings.

GEp-2γ final results

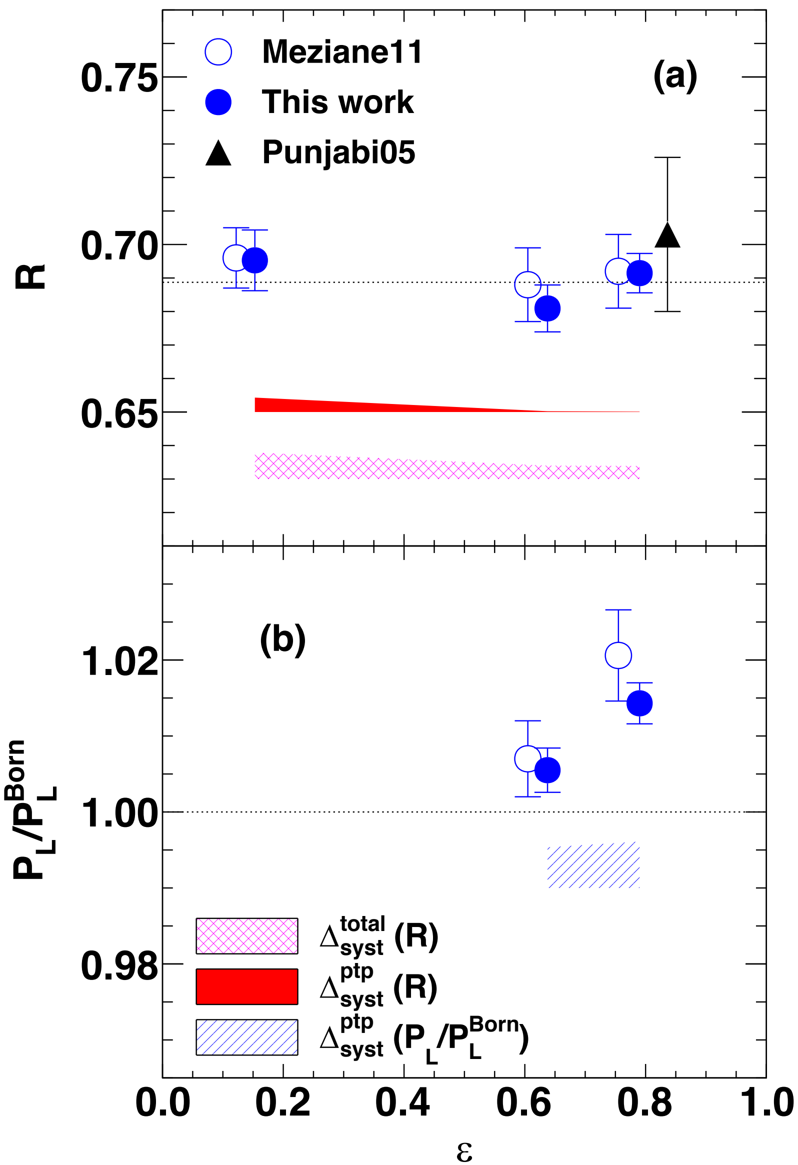

- For the originally published analysis, acceptance-matching cuts were applied to the two higher-ϵ points to match the envelope of elastic events at the HMS focal plane for the lowest ϵ. Additionally, $|\delta| \leq 2\%$ was required.
- These acceptance-matching cuts were applied to equalize the average Q^2, the analyzing power, and the spin transport across the three kinematics.
- The final analysis is based on the full-acceptance dataset for all three kinematics.
- The full acceptance data contain approximately 2.5 (3.4) times the statistics of the original publication at $\epsilon = 0.638$ (0.790)
- The acceptance-averaged results are quoted, and considered valid, at the acceptance-averaged kinematics.

$$R \equiv -\mu_p \sqrt{\frac{\tau(1+\epsilon)}{2\epsilon}} \frac{P_t}{P_\ell} = \frac{\mu_p G_E^p}{G_M^p} \text{ (Born approx.)}$$

New "Global" Fits to Proton FF Data

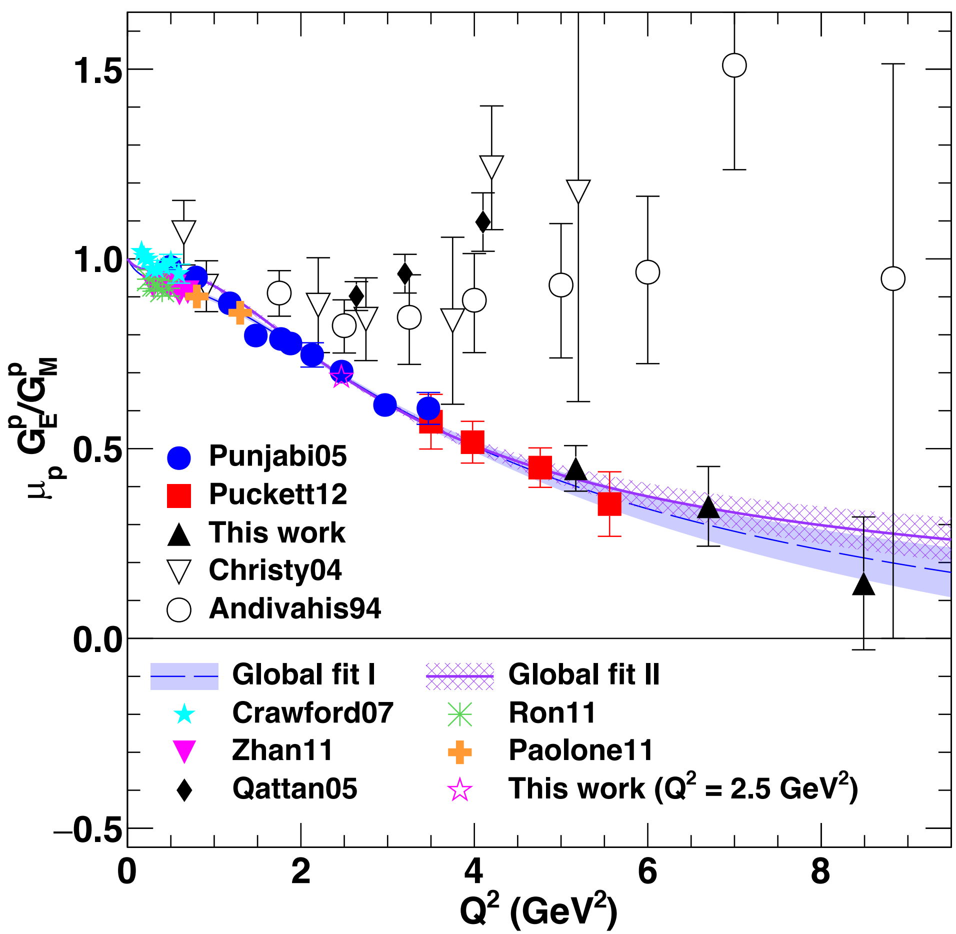

TABLE XIV. Summary of global proton FF fit results. Form factor parametrization is $G(Q^2) = \frac{1+a_1\tau}{1+b_1\tau+b_2\tau^2+b_3\tau^3}$, where $G(Q^2) = G_E(Q^2)$ or $G_M(Q^2)/\mu_p$. The uncertainty bands shown in Fig. 28 represent the pointwise, 1σ errors computed from the full covariance matrix of the fit result. The asymptotic values of the form factors shown below are normalized to a dipole form $G_D = (1+Q^2/\Lambda^2)^{-2}$ with scale parameter $\Lambda^2 = 0.66$ GeV^2 corresponding to an RMS radius $r_p = 0.84$ fm. The total χ^2 and degrees of freedom are shown along with the breakdown of χ^2 contributions among cross section (σ_R) and polarization (R_p^{pol}) data. The χ^2 contributions of cross section measurements are also separated into "low" ($Q^2 \le 1$ GeV^2) and "high" ($Q^2 > 1$ GeV^2) data. The best-fit normalization constants of the cross section experiments are omitted for brevity.

Fit	Global fit I	Global fit II
a_1^E	-0.21 ± 0.09	-0.01 ± 0.14
b_1^E	12.21 ± 0.18	12.16 ± 0.25
b_2^E	12.6 ± 1.1	9.7 ± 1.3
b_3^E	23 ± 4	37 ± 7
a_1^M	0.058 ± 0.022	0.093 ± 0.025
b_1^M	10.85 ± 0.073	11.07 ± 0.08
b_2^M	19.9 ± 0.2	19.1 ± 0.2
b_3^M	4.4 ± 0.6	5.6 ± 0.7
$\lim_{Q^2\to\infty} \frac{G_E^p}{G_D(r_p=0.84\text{ fm})}$	-0.26 ± 0.15	-0.01 ± 0.11
$\lim_{Q^2\to\infty} \frac{G_M^p}{\mu_p G_D(r_p=0.84\text{ fm})}$	0.38 ± 0.09	0.47 ± 0.07
χ^2/ndf (all data)	706/460	696/455
χ^2/n_{data} (σ_R)	672/427	653/427
χ^2/n_{data} (R_p^{pol})	34/53	44/48
χ^2/n_{data} ($\sigma_R, Q^2 \le 1$ GeV^2)	337.7/275	308.4/275
χ^2/n_{data} ($\sigma_R, Q^2 > 1$ GeV^2)	334.5/152	344.1/152

Two global fits, differing only in choice of low-Q^2 polarization data for $\frac{\mu_p G_E^p}{G_M^p}$

- Global fit I: includes recent precise recoil polarization data from Hall A (Ron11 Zhan11, Paolone11), excludes BLAST data (Crawford07) and the two lowest Q^2 points from GEp-I (Punjabi05).
- Global fit II: excludes Ron11, Zhan11, Paolone11, includes Crawford07, and all of GEp-I data.

The low-Q^2 region

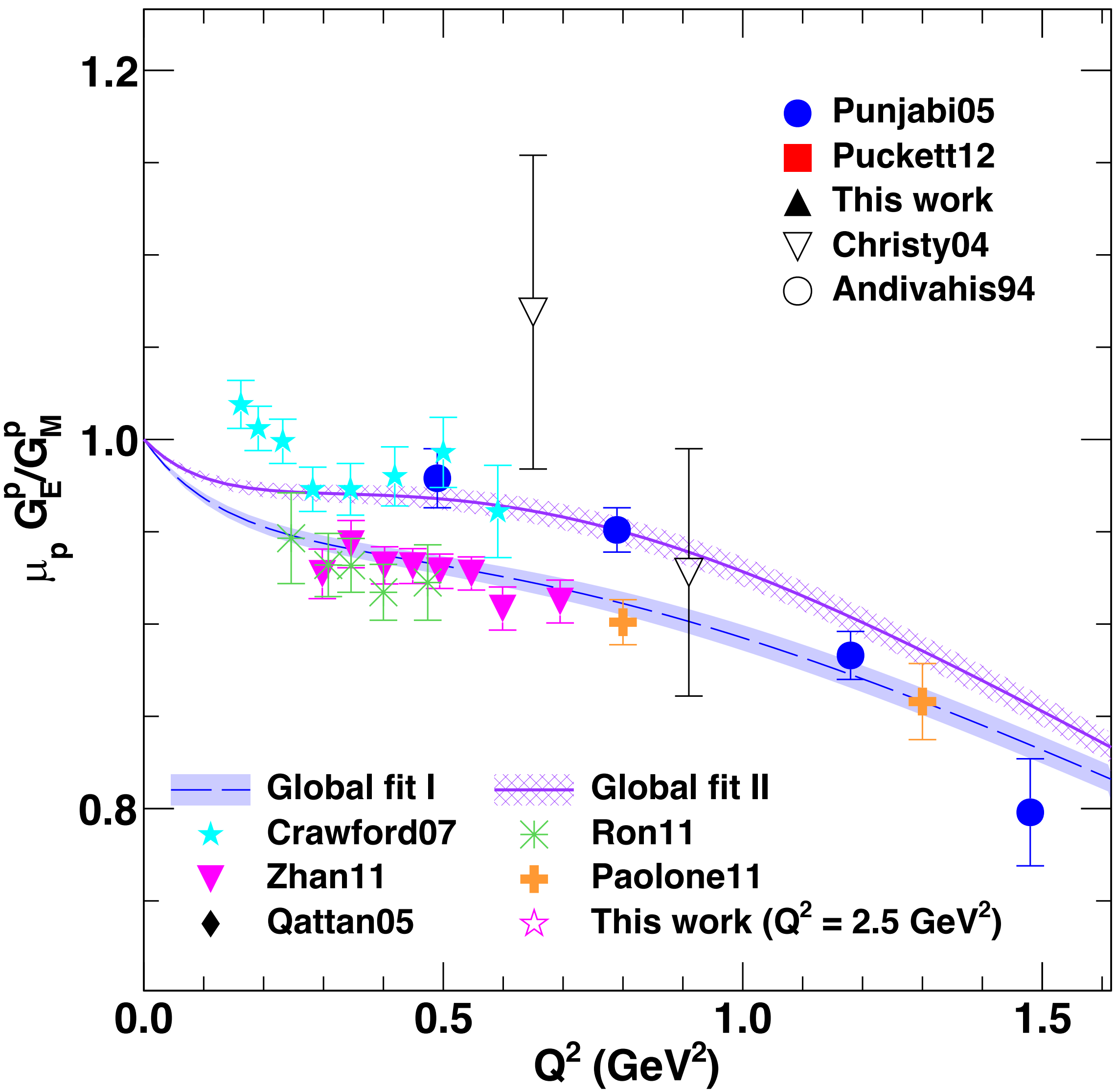

- Unresolved tension among polarization data in the low-Q^2 region.
- The two global proton FF fits differ only in the selection of low-Q^2 data

New “Global” Fits: Data/fit ratios

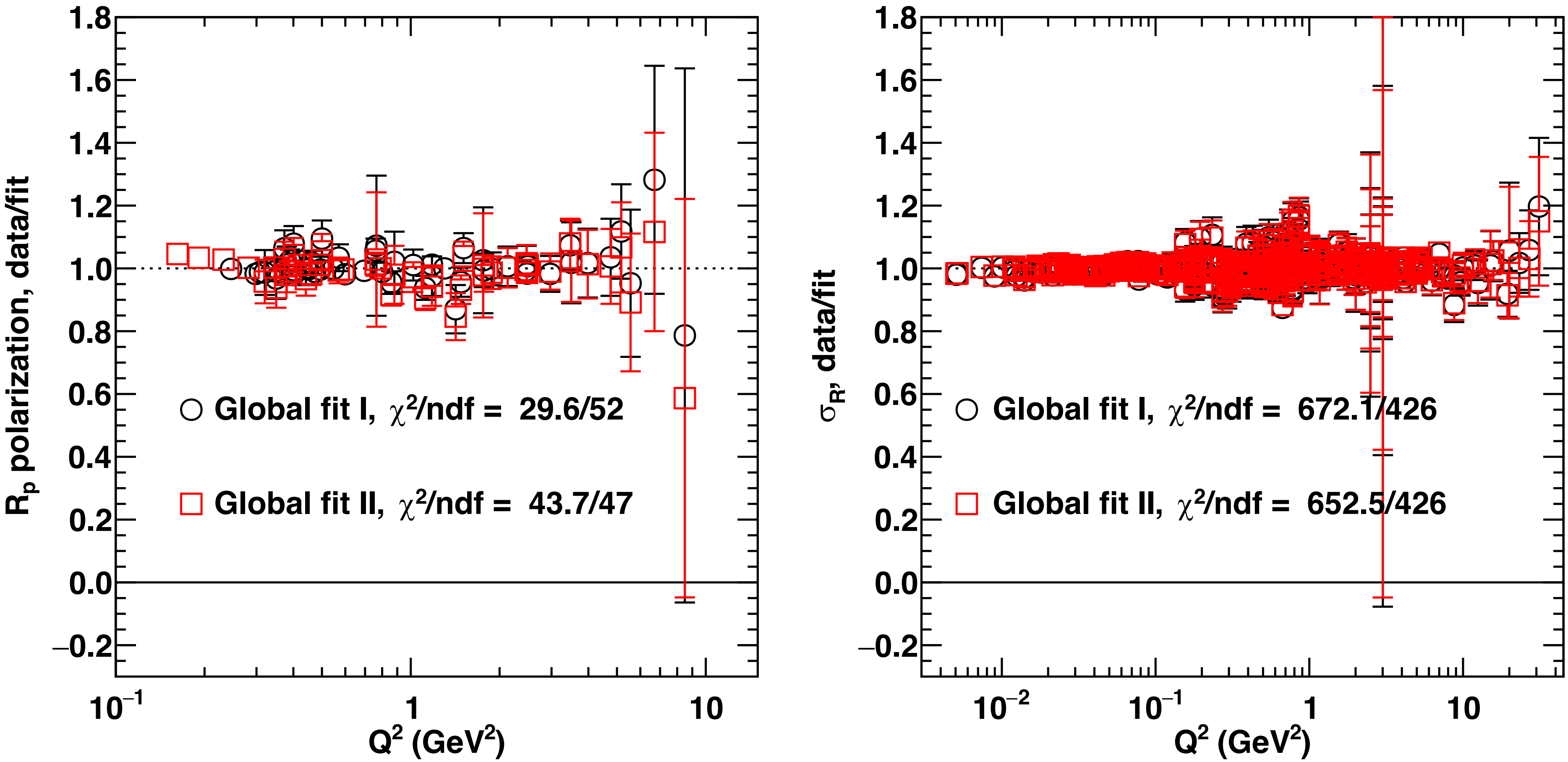

- The global fits were used to estimate the bin centering effects for the FF ratio at 2.5 GeV^2, and to ensure a self-consistent extraction of P_ℓ / P_ℓ^{Born}.
- The recent Mainz low-Q^2 data were not included in the fits.

New Global Fit II: Proton FFs

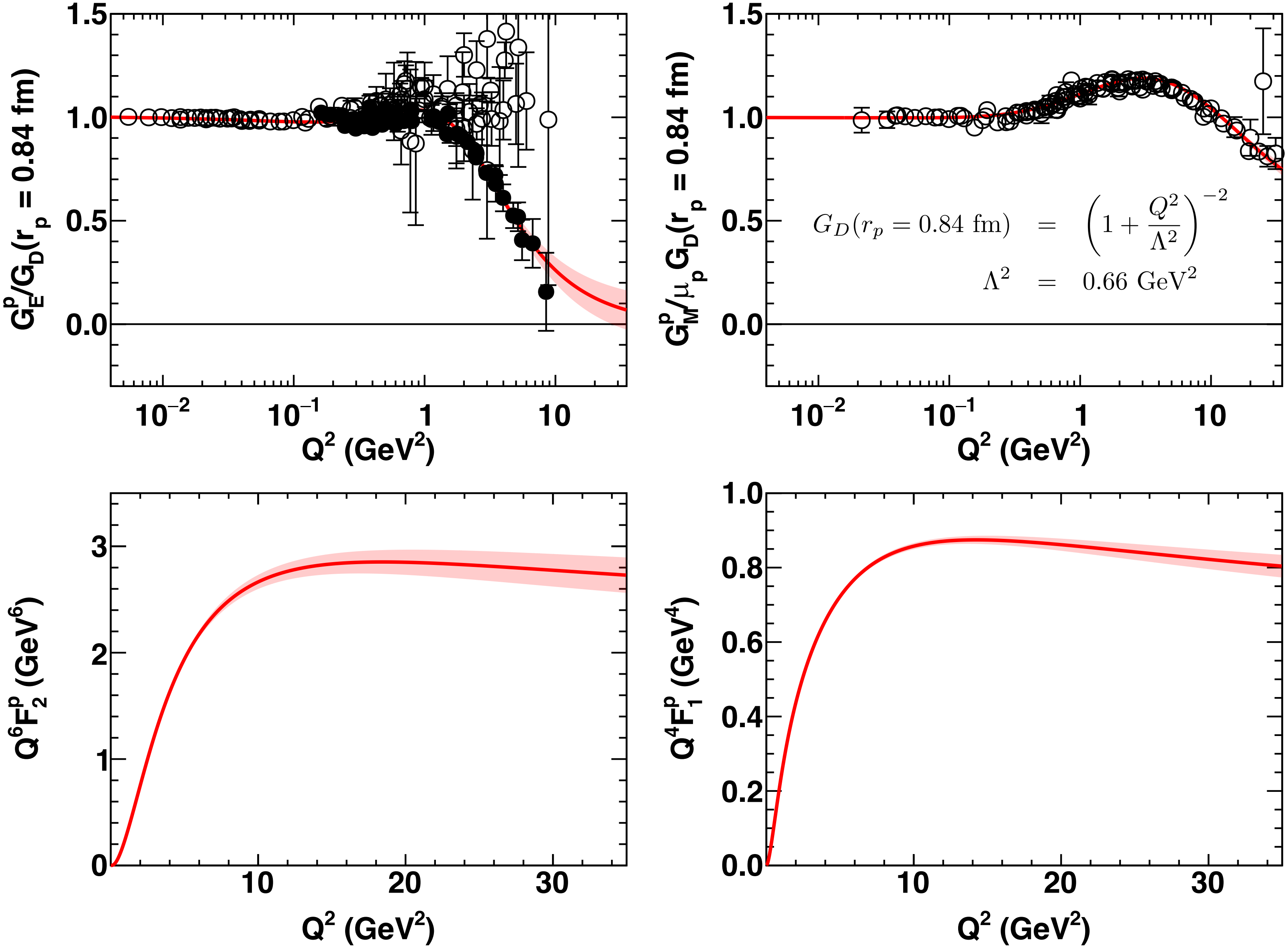

GEp-2γ full-acceptance data: Q^2 dependence

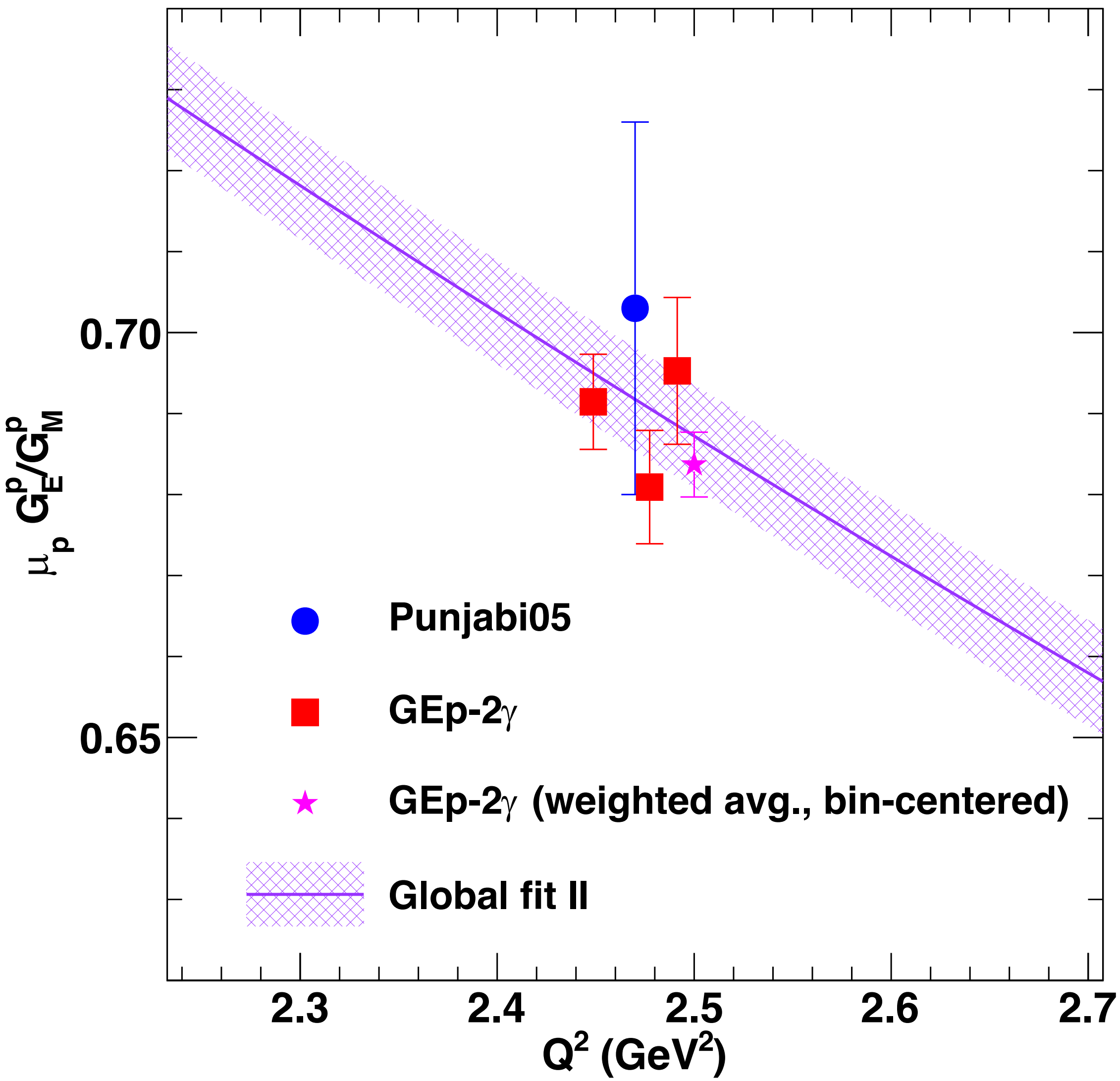

- Unlike original (PRL) publication, the unbinned full-acceptance data for GEp-2γ have significantly different average Q^2 values.
- The global Q^2 dependence of $\frac{G_E^p}{G_M^p}$ is used to correct the data to a common central $Q^2 = 2.5$ GeV^2.
- A bin-centering correction is calculated assuming that the global Q^2 dependence of R factorizes from any ϵ dependence, at least within the acceptance of each kinematic.

Bin-centering effects in GEp-2γ data

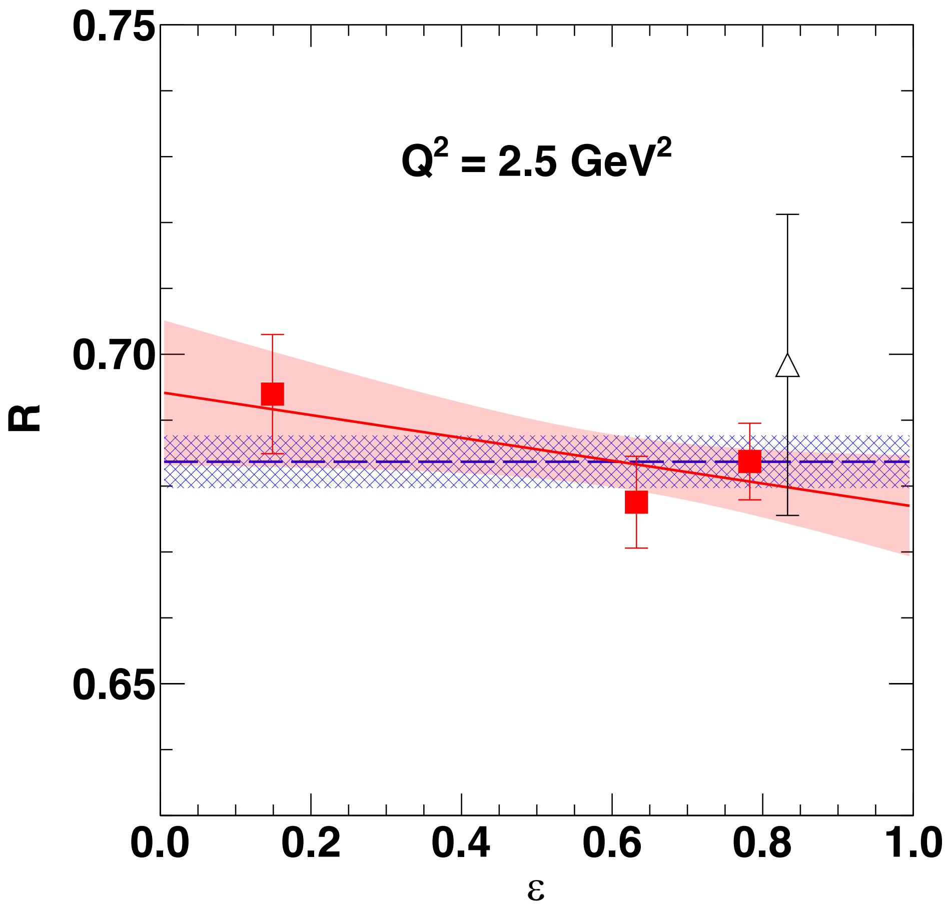

Bin-centering corrected data for R vs. ϵ, with linear fit and 68% confidence band.

TABLE XII. Summary of bin-centering corrections to R at $Q^2 = 2.5$ GeV^2. $\langle Q^2 \rangle$ and $\langle \epsilon \rangle$ are the acceptance-averaged kinematics. ϵ_c is the central ϵ value computed from the central Q^2 value and the average beam energy. R_{bcc} is the bin-centering-corrected value of R with statistical uncertainty. $R_{bcc} - R_{avg}$ is the bin-centering correction relative to the results for the average kinematics reported in Tab. XI.

$\langle Q^2 \rangle$ (GeV^2)	$\langle \epsilon \rangle$	ϵ_c	$R_{bcc} \pm \Delta_{stat} R_{bcc}$	$R_{bcc} - R_{avg}$
2.491	0.153	0.149	0.6940 ± 0.0091	-0.0013
2.477	0.638	0.632	0.6776 ± 0.0070	-0.0033
2.449	0.790	0.783	0.6837 ± 0.0059	-0.0078

TABLE XIII. Linear and constant fit results for the ϵ dependence of R, with and without bin-centering corrections. Quoted uncertainties in fit results are statistical only.

	No b.c.c.	b.c.c.
Slope $dR/d\epsilon$	-0.0076 ± 0.0169	-0.0173 ± 0.0169
Linear fit χ^2/ndf	1.78/1	1.02/1
Linear fit "p"-value	0.18	0.31
Linear fit $R(\epsilon = 0)$	0.693 ± 0.011	0.694 ± 0.011
Constant fit R	0.6887 ± 0.0040	0.6837 ± 0.0040
Constant fit χ^2/ndf	1.98/2	2.07/2
Constant fit "p"-value	0.37	0.36

Theoretical interpretation of high-Q² FFs—PQCD scaling?

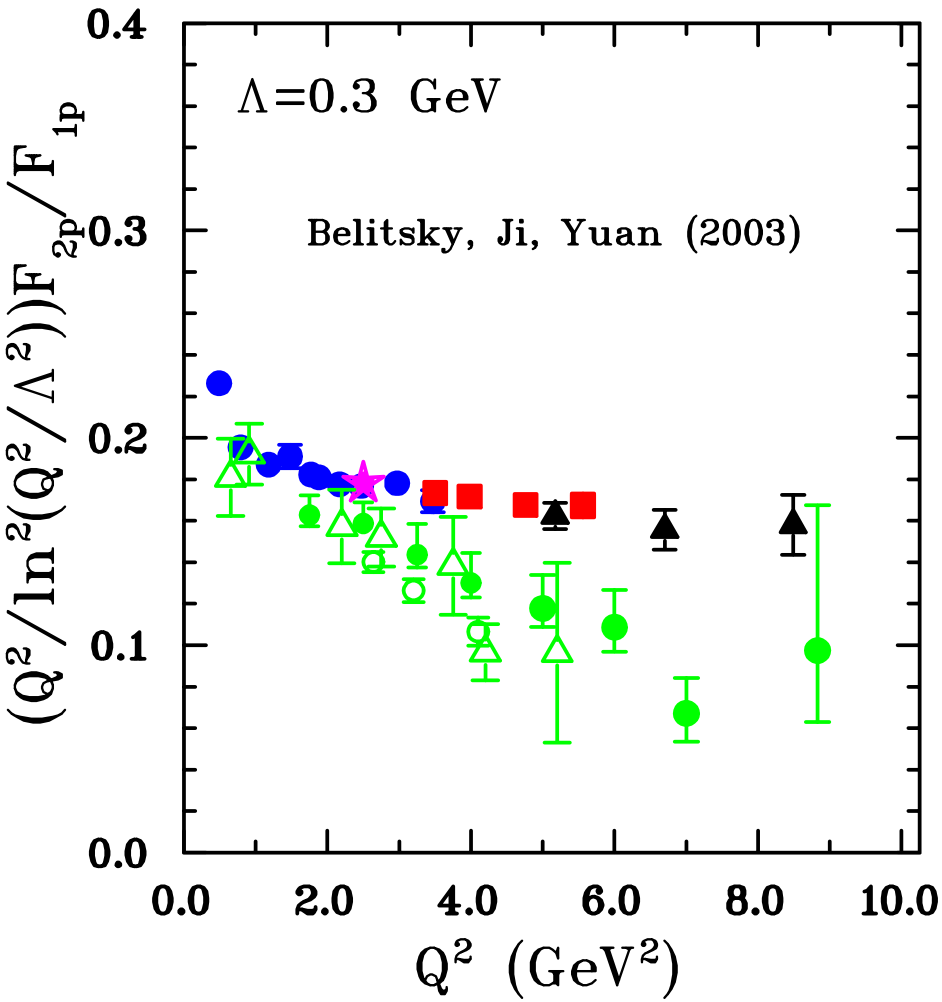

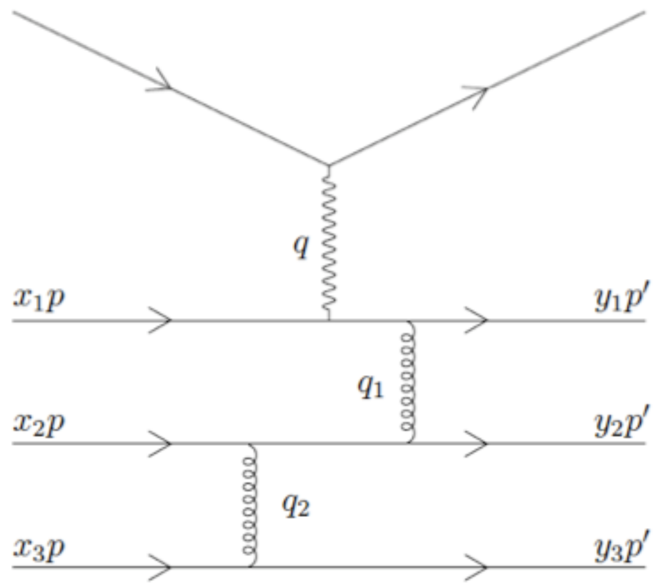

- Brodsky, Farrar, PRD 11, 1309 (1975) $\quad F_1 \propto \frac{\alpha_S^2}{Q^4}$
- Brodsky, Lepage PRL 43, 545 (1979) $\quad F_2 \propto \frac{F_1}{Q^2}$
- Belitsky, Ji, Yuan, PRL 91, 092003 (2003) $\quad \left(\frac{Q^2}{\ln^2\left(\frac{Q^2}{\Lambda^2}\right)}\right) F_2^p \propto F_1^p$

"Precocious" scaling observed in F_2^p/F_1^p not seen in F_2^n/F_1^n, for values of cutoff parameter Λ similar to that which describes proton data

Reaching high Q^2 in Lattice QCD

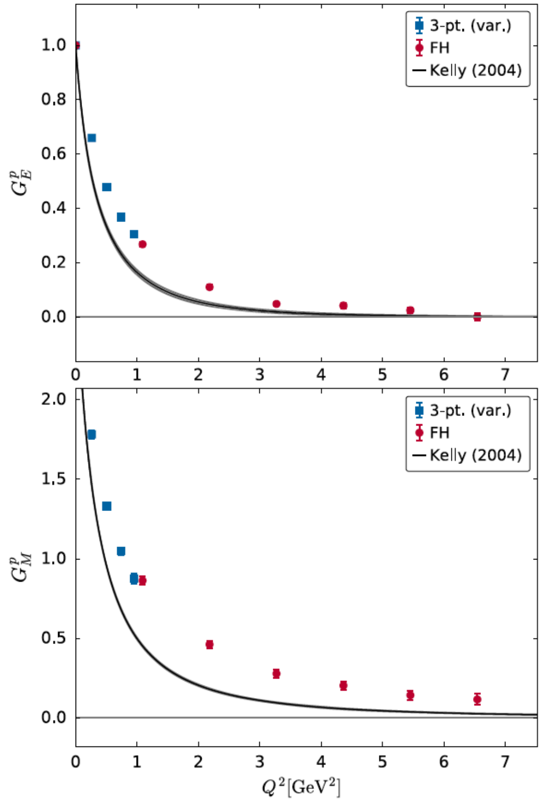

FIG. 3. G_E and G_M for the proton from the Feynman-Hellmann method and from a variational method described in Ref. [29] employed on the same ensemble. The experimental parametrization is from Ref. [49].

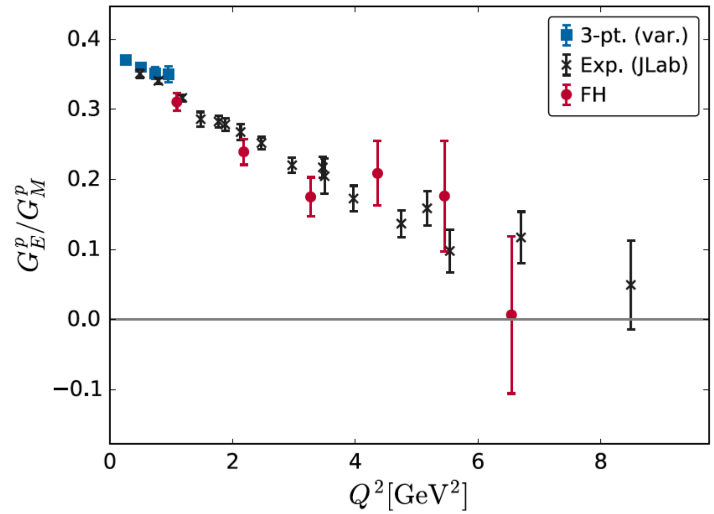

FIG. 4. Ratio G_E/G_M for the proton from the application of the Feynman-Hellmann method, from a variational analysis of three-point functions [29], and from experiment [5–7]. Note this is not scaled by the magnetic moment of the proton μ_p, as this would require phenomenological fits to the low-Q^2 data, which is not the focus of this work.

$$\frac{\partial E_\psi}{\partial \lambda} = \left\langle \psi \left| \frac{\partial H}{\partial \lambda} \right| \psi \right\rangle$$

A. J. Chambers *et al.*, (QCDSF/UKQCD/CSSM Collaborations) Phys. Rev. D 96, 114509 (2017)

- Novel application of the Feynman-Hellman method: relates hadronic matrix elements to energy shifts, allowing access to form factors via two-point correlators as opposed to more complicated three-point functions; improves signal-to-noise ratio for high-momentum states

Dyson-Schwinger Equations/diquark correlations

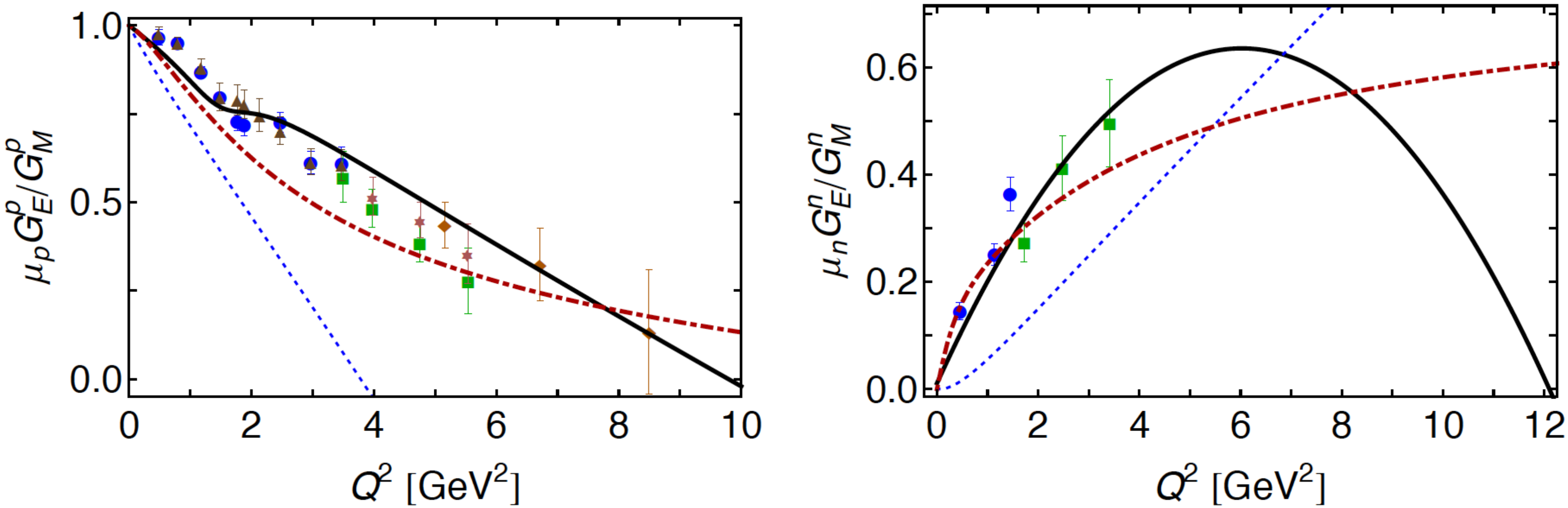

Fig. 3 *Left panel*: normalised ratio of proton electric and magnetic form factors. Curves: *solid, black* – result obtained herein, using our QCD-kindred framework; *Dashed, blue* – CI result [18]; and *dot-dashed, red* – ratio inferred from 2004 parametrisation of experimental data [65]. Data: blue circles [68]; green squares [69]; brown triangles [70]; purple asterisk [71]; and orange diamonds [72]. *Right panel*: normalised ratio of neutron electric and magnetic form factors. Curves: same as in left panel. Data: blue circles [73]; and green squares [74].

J. Segovia, I. Cloet and C. Roberts: [Few-Body Syst. 55, 1185 (2014)]

Quote from the abstract:

of dynamical chiral symmetry breaking in the bound-state problem. Amongst the results we describe, the following are of particular interest: $G_E^p(Q^2)/G_M^p(Q^2)$ possesses a zero at $Q^2 = 9.5\,\mathrm{GeV}^2$; any change in the interaction which shifts a zero in the proton ratio to larger Q^2 relocates a zero in $G_E^n(Q^2)/G_M^n(Q^2)$ to smaller Q^2; there is likely a value of momentum transfer above which $G_E^n > G_E^p$; and the presence of strong diquark correlations within the nucleon is sufficient to understand empirical extractions of the flavour-separated form factors. Regarding the $\Delta(1232)$-baryon, we find that, *inter*

Exposing the dressed-quark mass function

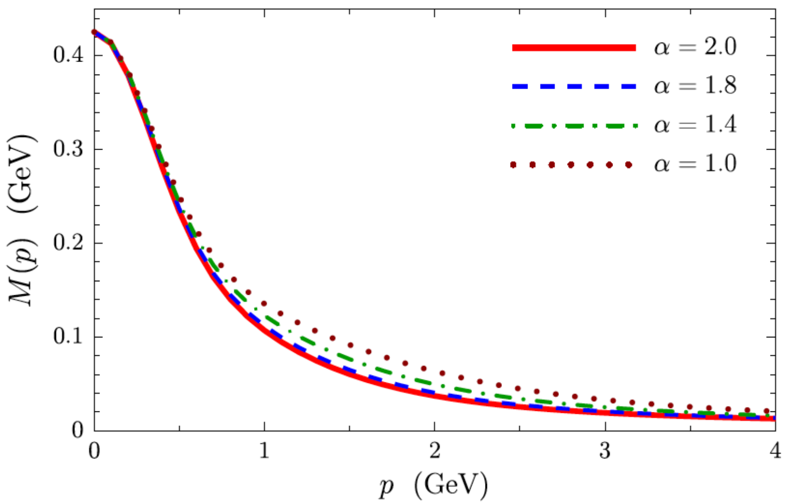

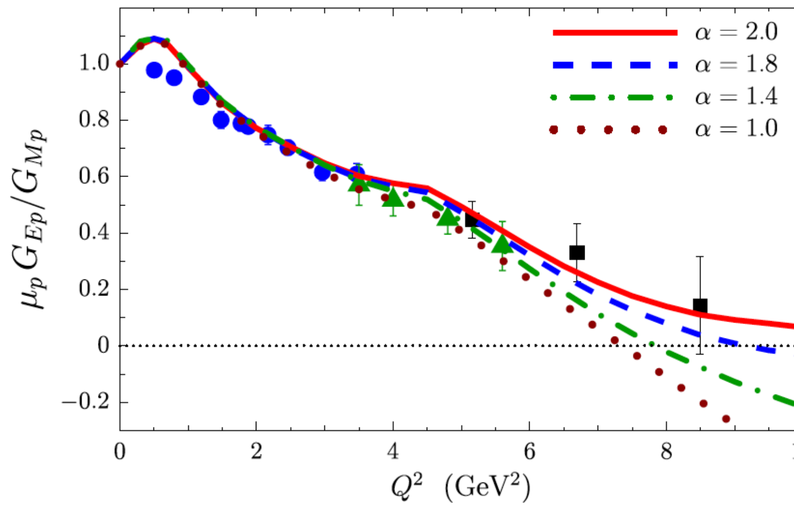

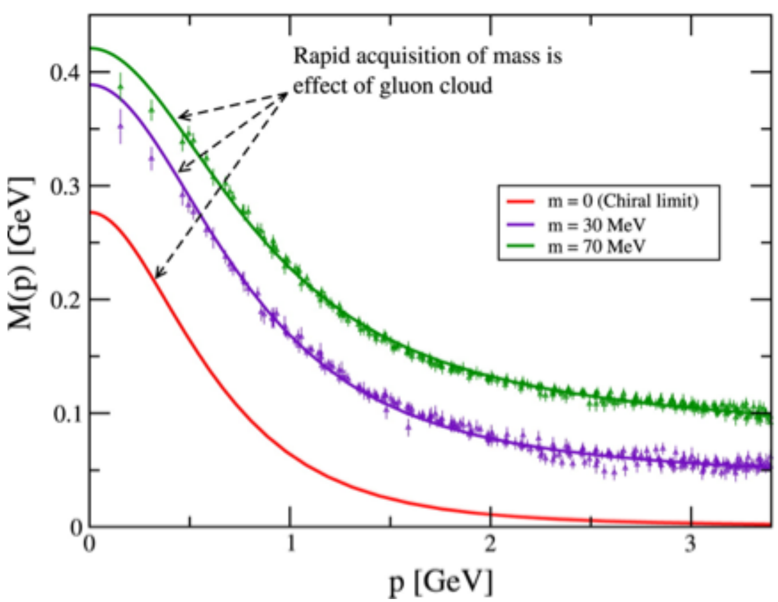

In the framework of Dyson-Schwinger equations, the high-Q^2 nucleon FFs ($Q^2 > 5$ GeV^2) are especially sensitive to momentum-dependent dressed-quark mass function in the few-GeV region, see e.g.,:

- I. Cloet, C. Roberts, A. Thomas: “Revealing Dressed Quarks via the Proton’s Charge Distribution”, **PRL 111, 101803 (2013)**
- I. Cloet and C. Roberts: “Explanation and Prediction of Observables Using Continuum Strong QCD”, arxiv:1310.2651v2 (2013), **PPNP 77 (2014), 1-69**

Nucleon EMFFs compared to selected theoretical predictions

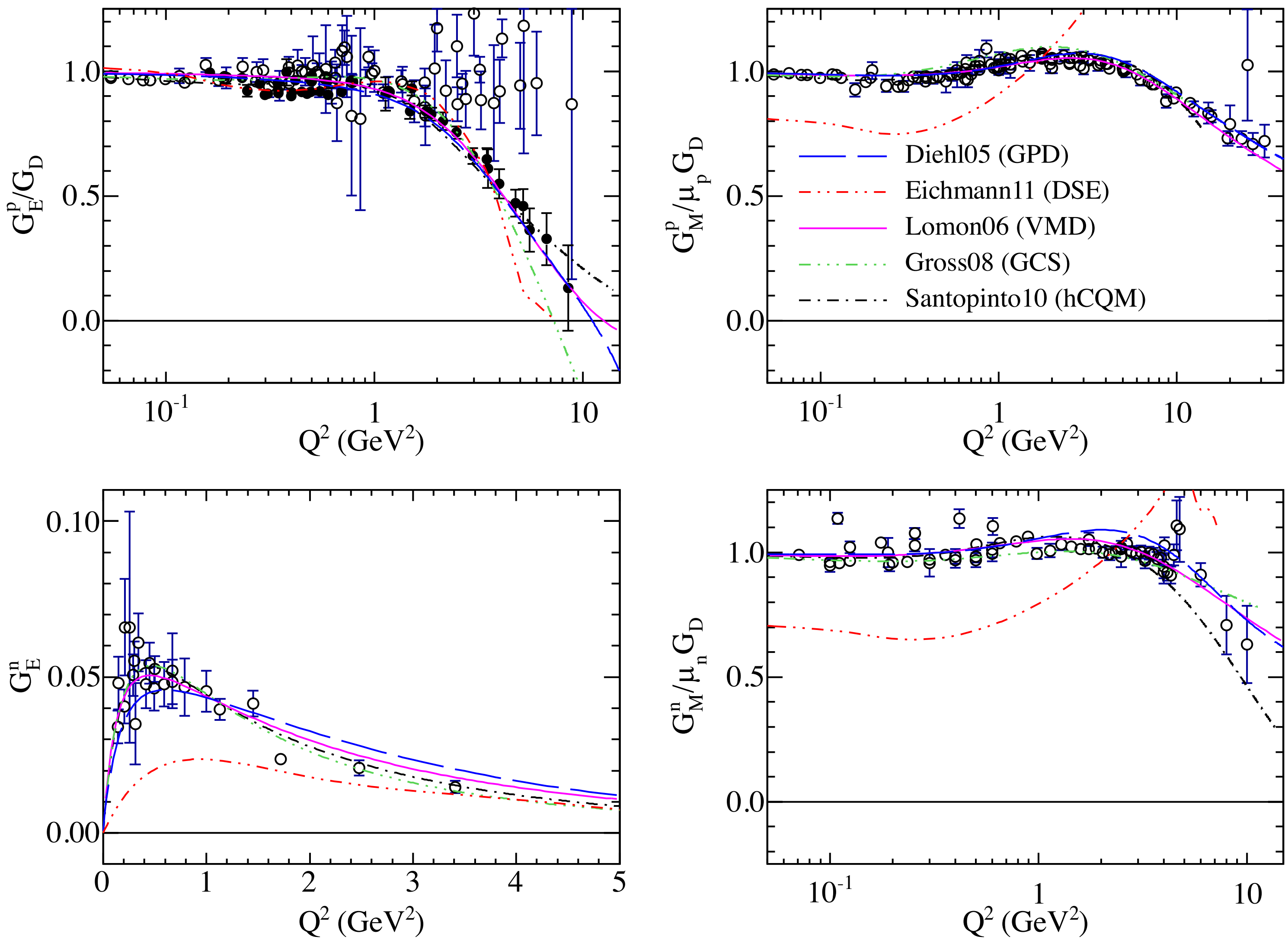

Figure from Puckett *et al.,* Phys Rev. C 85, 045203 (2012)

Rosenbluth-Polarization Discrepancy and Two-Photon-Exchange

- “Standard” QED radiative corrections to ep cross section data at lowest order in α include:
    - Vertex corrections
    - Vacuum polarization
    - Self-energy
    - Bremsstrahlung
- Two-photon exchange (TPEX) process where both photons are “hard”: previously neglected
    - **Cannot be calculated model-independently**
    - **Has been shown to partially resolve the discrepancy between L/T and polarization data for G_{Ep}**

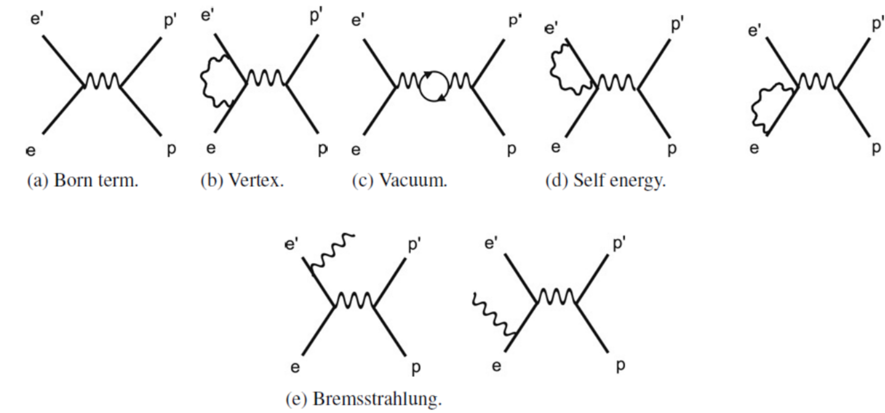

Fig. 24. Born term and lowest order radiative correction graphs for the electron in elastic *ep*.

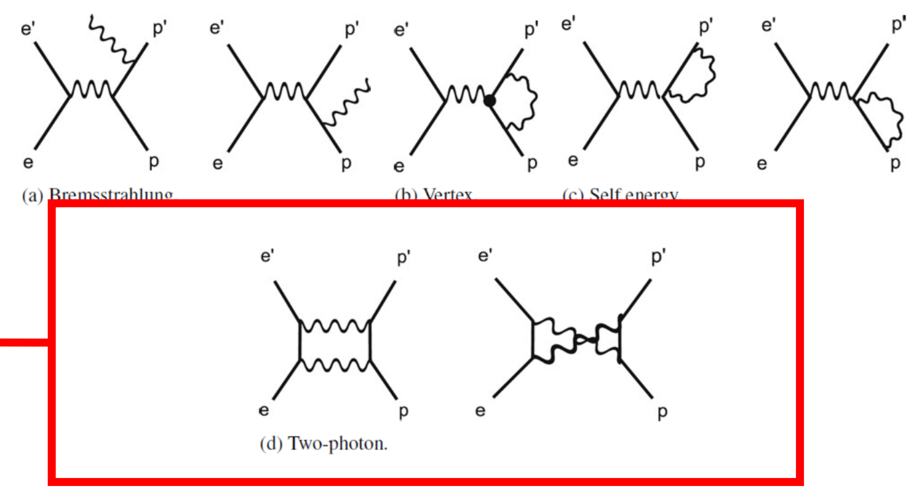

Two-photon-exchange and the G_{Ep} puzzle—experiment and theory

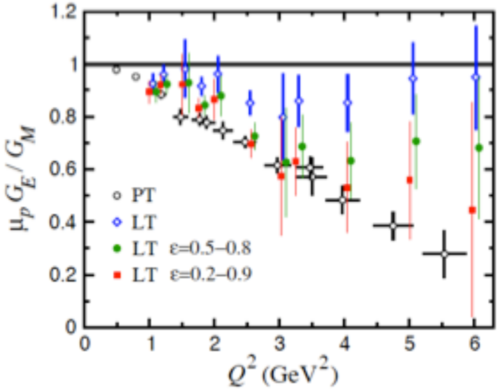

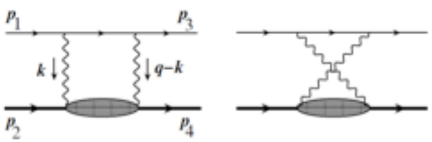

FIG. 1: Two-photon exchange box and crossed box diagrams for elastic electron-proton scattering.

"Hadronic" approach: Blunden, Melnitchouk, Tjon, **PRC 72, 034612 (2005)**. TPEX corrections with N intermediate state

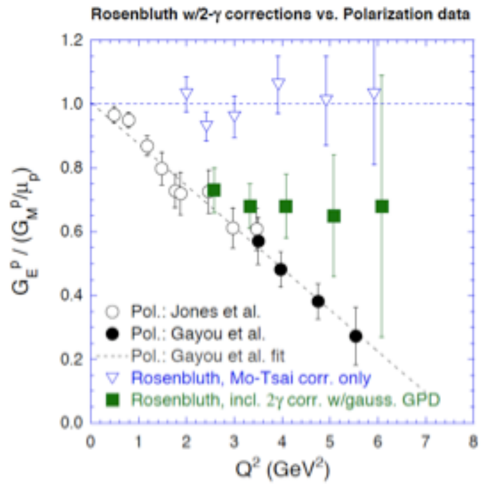

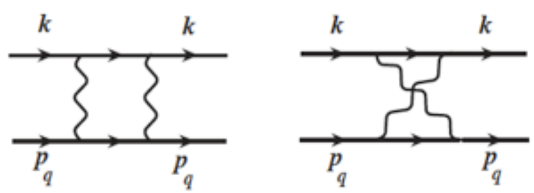

"Partonic" approach: Afanasev *et al.*, **PRD 72, 013008 (2005).** TPEX in "hard" scattering on a single quark, embedded in nucleon through GPDs

Experimental efforts:

- Several experimental observables are directly sensitive to TPEX effects
- ε-dependence of "R" ratio from polarization transfer. GEp-2γ: originally published Meziane *et al.*, **PRL 106, 132501 (2011),** and this work
- Induced normal recoil polarization or analyzing power A_N; imaginary part of TPEX amplitude—**never measured!**
- Elastic e^+p/e^-p cross section ratio: zero in one-photon exchange, measures real part of 2γ-exchange amplitude. Three experiments recently published:
  - CLAS-TPE (JLab Hall B)
  - OLYMPUS@DESY
  - VEPP-III (Novosibirsk)
- For a recent review, see Afanasev *et al.*, Prog. Part. Nucl. Phys. 95,245(2017)

GEp-2γ data compared to model TPEX calculations

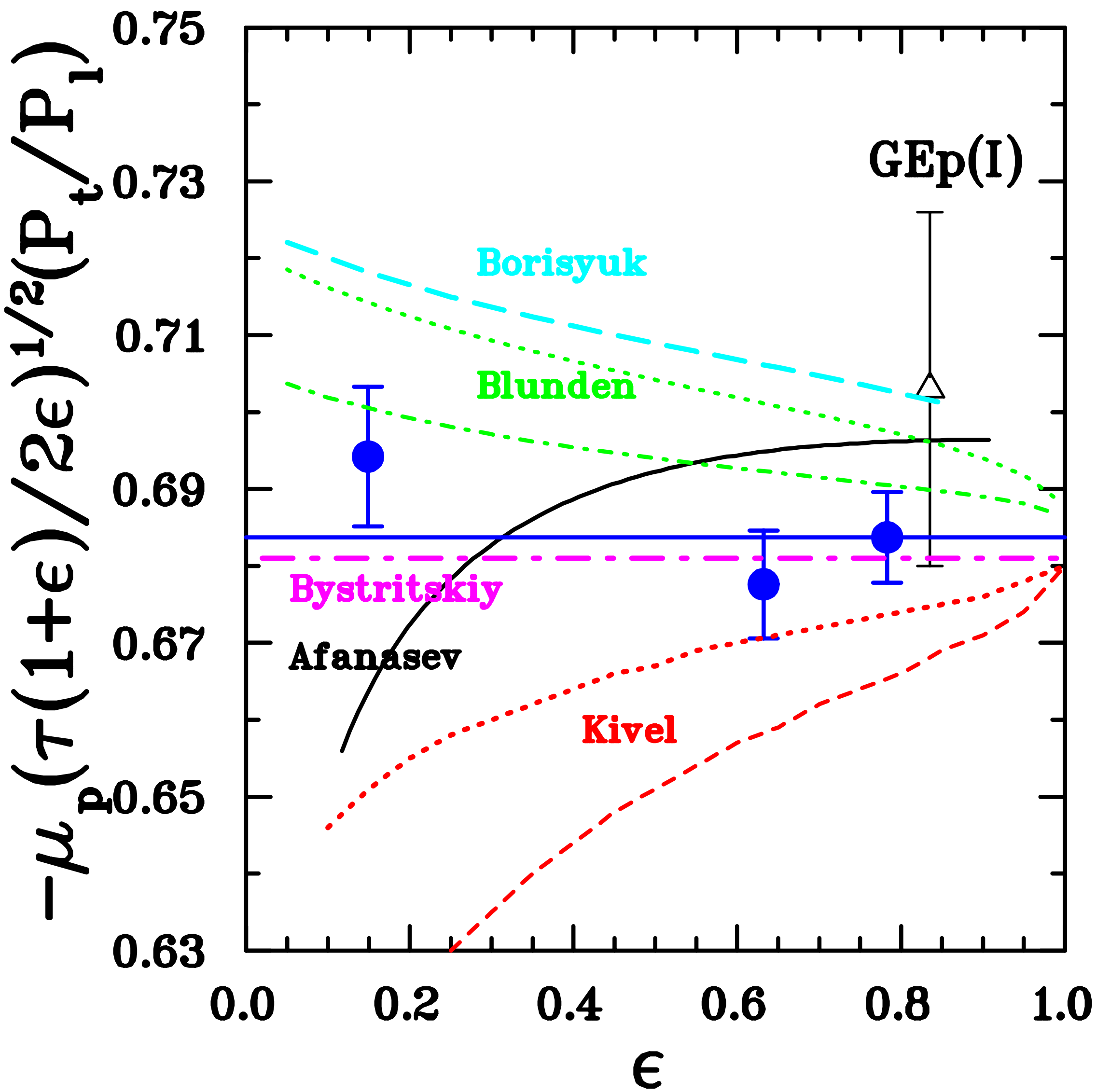

- Borisyuk: Phys. Rev. C 89, 025204 (2014).
  - Dispersion theory calculation including P_{33} πN contribution with width, shape, and nonresonant continuum
- Blunden: Phys. Rev. C95, 065209 (2017)
  - Dispersion theory calculation with "on shell" intermediate N (green dot-dashed) and N+Δ (green dotted)
- Bystritskiy: Phys. Rev. C75, 015207 (2007).
  - All-order QED RC calculation using electron structure function method
- Afanasev: Phys. Rev. D72, 013008 (2005).
  - Partonic approach using GPD model
- Kivel: Phys. Rev. Lett. 103, 092004 (2009)
  - PQCD approach using DAs

Status of TPEX

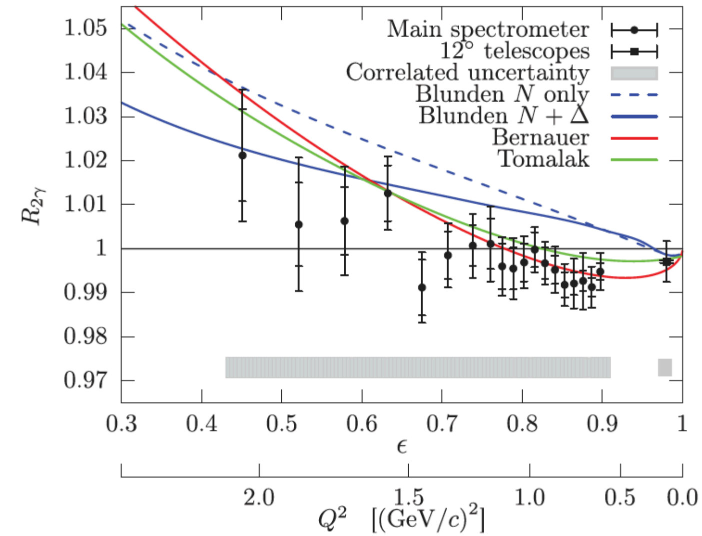

FIG. 2. OLYMPUS result for $R_{2\gamma}$ using the Mo-Tsai [21] prescription for radiative corrections to all orders. Uncertainties shown are statistical (inner bars), uncorrelated systematic (added in quadrature, outer bars), and correlated systematic (gray band). Note the 12° data point at $\epsilon = 0.978$ is completely dominated by systematic uncertainties.

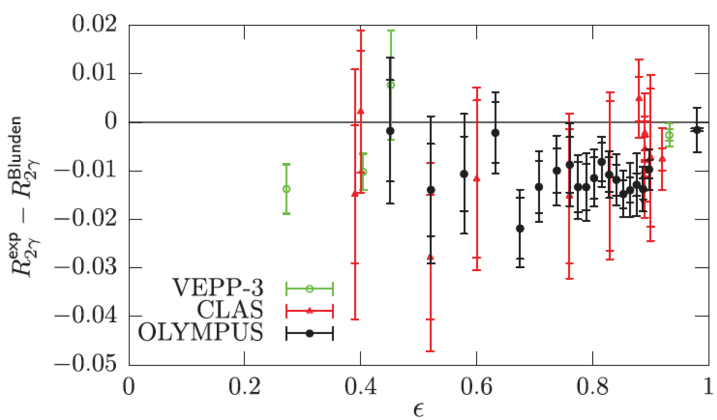

FIG. 3. Comparison of the recent results to the calculation by Blunden. The data are in good agreement, but generally fall below the prediction. Please note that data at similar ϵ values have been measured at different Q^2. Also note that the VEPP-3 data have been normalized to the calculation at high ϵ.

- Henderson *et al.*, (OLYMPUS Collaboration): Phys. Rev. Lett. 118, 092501 (2017)
- S. K. Blau, Physics Today 70, 14 (2017)
- Blunden TPEX calculation with N and N+Δ intermediate states is consistent with recent e+p/e-p cross section ratios from CLAS-TPE, VEPP-3 (Novosibirsk), and OLYMPUS data.
- However, all of these data have $Q^2 \leq 2.1$ GeV^2

Summary of GEp-III/GEp-2γ

- New analysis reduces systematic uncertainty for all data and significantly reduces statistical uncertainty for GEp-2γ high-ϵ kinematics
- Sharpens the constraints on models of hard TPEX amplitudes at $Q^2 = 2.5$ GeV^2.
- Confirms the validity of the polarization transfer method, in the sense that deviations from the Born approximation are not large in PT observables, and consistency of data from different experiments over a wide range of Q^2 are highly internally consistent (see, however, low-Q^2 data tension)
- Hall C experience carries important lessons for future efforts to reach yet higher Q^2

Nucleon Form Factors in the 12 GeV era

Precision elastic ep cross sections in Hall A

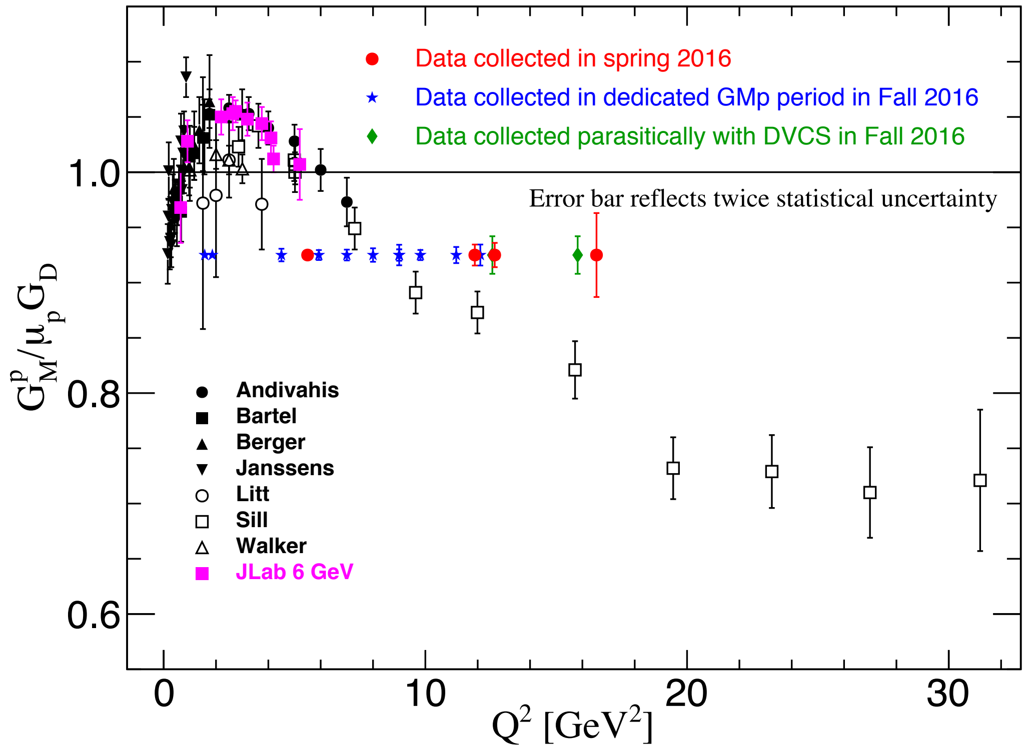

Projected results from recently completed Hall A high-Q^2 G_{Mp} run

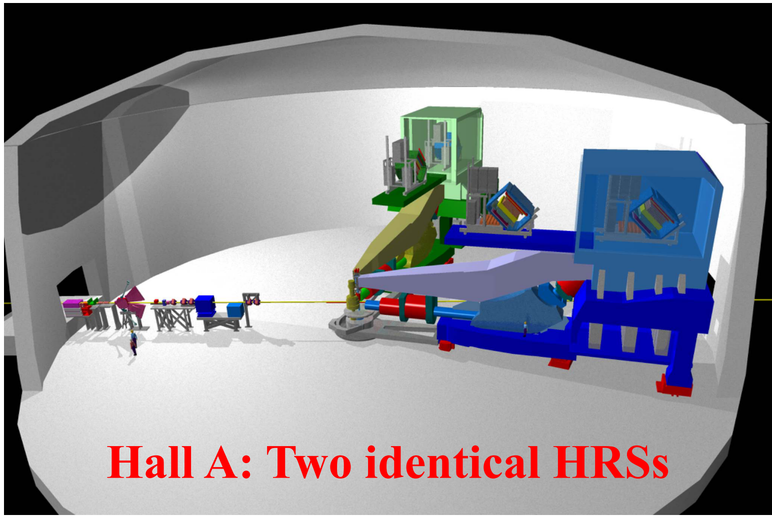

- Elastic ep → ep cross section at large Q^2 is dominated by G_{Mp}.
- Existing data for $Q^2 \geq 10$ GeV^2 come from a single experiment at SLAC (Sill *et al.*, Phys. Rev. D, 48(1), 29 (1993)) with large uncertainties
- The absolute elastic *ep* cross section data serve as the "anchor" for the determination of all four nucleon EMFFs

Electron Scattering Kinematics @11 GeV

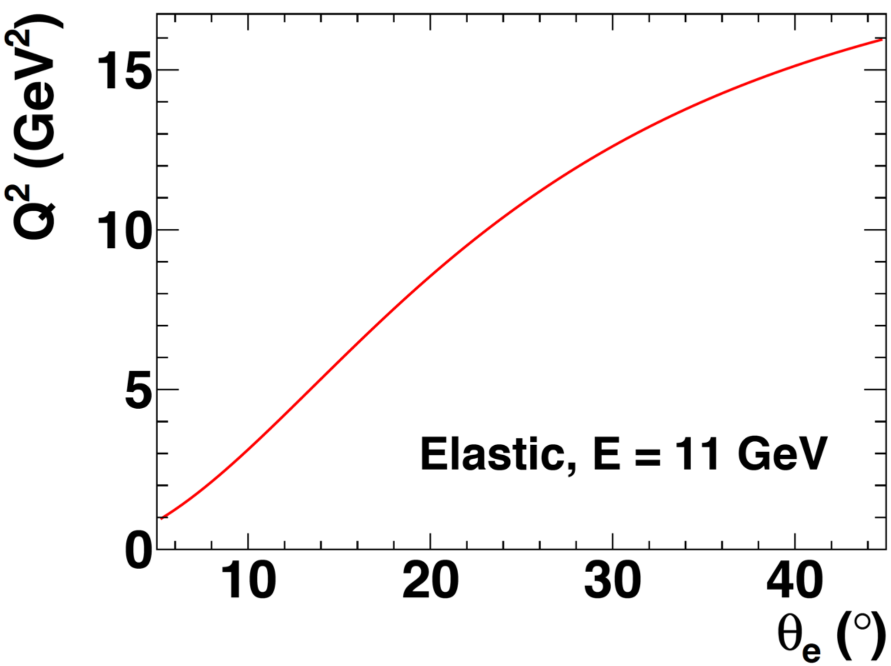

- Measurements of elastic FFs, SIDIS, DVCS, etc involve coincidence N(e,e'X) (electroproduction) reactions, where X =
  - N' (elastic)
  - h (SIDIS or DVMP)
  - γ (DVCS)
- Virtual photon angle decreases as "inelasticity" increases

$$Q^2 = 2M\nu x_{Bj}$$

- Particles associated with the partonic (or other) degree of freedom that absorbed the virtual photon are found predominantly near the direction of the momentum transfer **q**
- ***Partonic interpretation is accessible at large Q^2 → particles of interest are located at forward angles and high momentum***

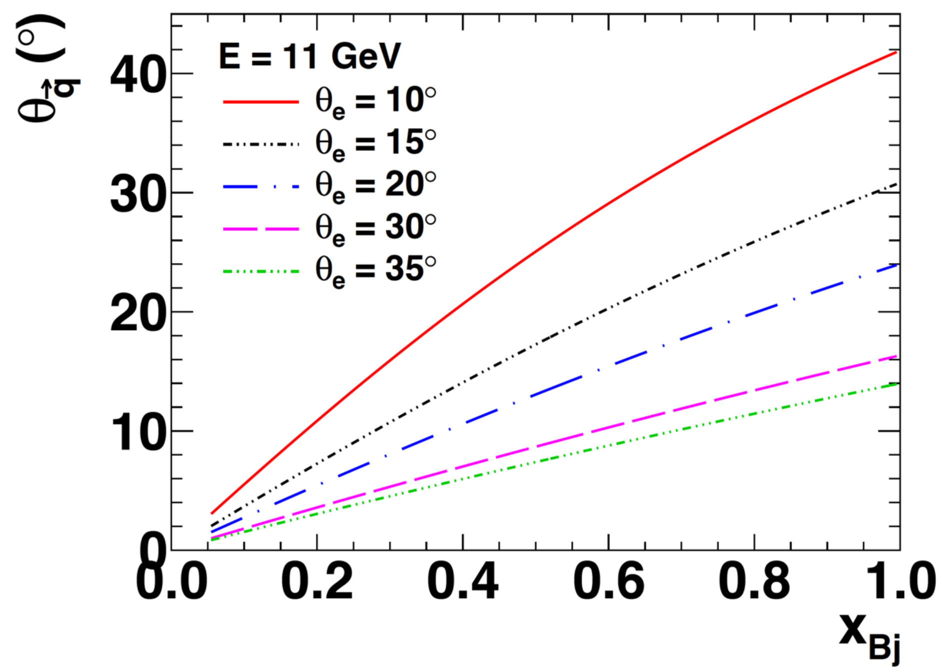

The Super BigBite Spectrometer in Hall A

Proton form factors ratio, GEp(5) (E12-07-109)

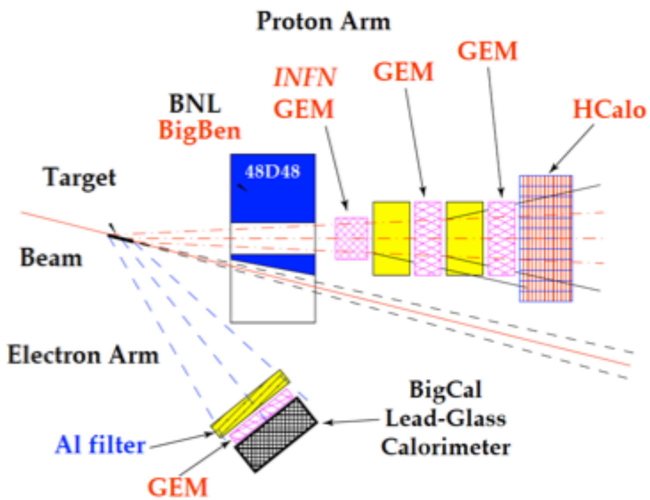

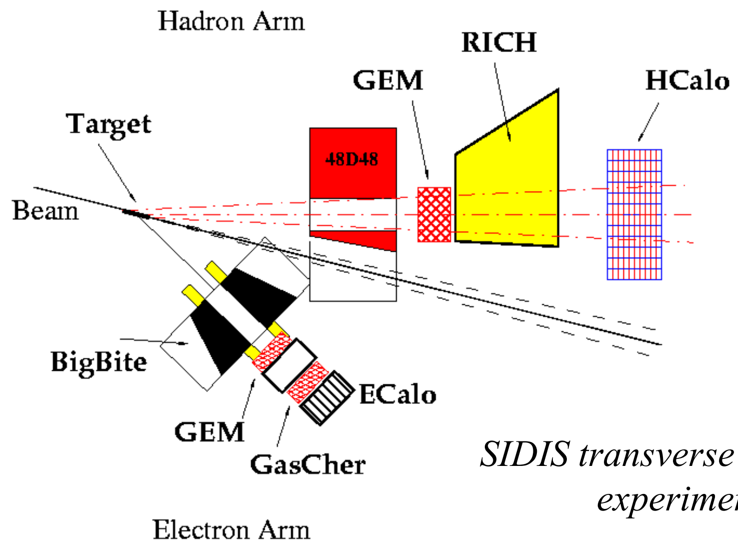

SIDIS transverse single-spin asymmetry experiment: E12-09-018

Neutron form factors, E12–09–016 and E12–09–019

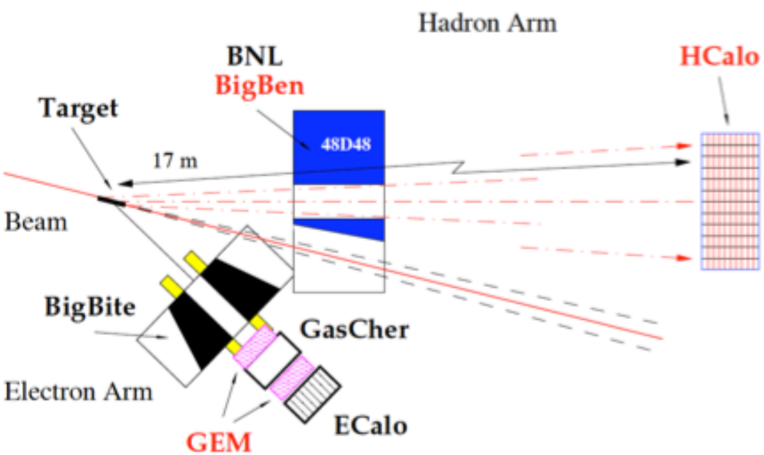

- What is it? A 2.5 T*m dipole magnet with vertical bend, a cut in the yoke for passage of the beam pipe to reach forward scattering angles, and a flexible/modular configuration of detectors.
- Designed to operate at luminosities up to 10^{39} cm^{-2} s^{-1} with large momentum bite, moderate solid angle
- Time-tested "Detectors behind a dipole magnet", two-arm coincidence approach—historically most productive in fixed-target expts.
- ***Large solid-angle + high luminosity @ forward angles = most interesting physics!***

Gas Electron Multipliers (GEMs): High-Rate, High Resolution Charged-Particle Tracking

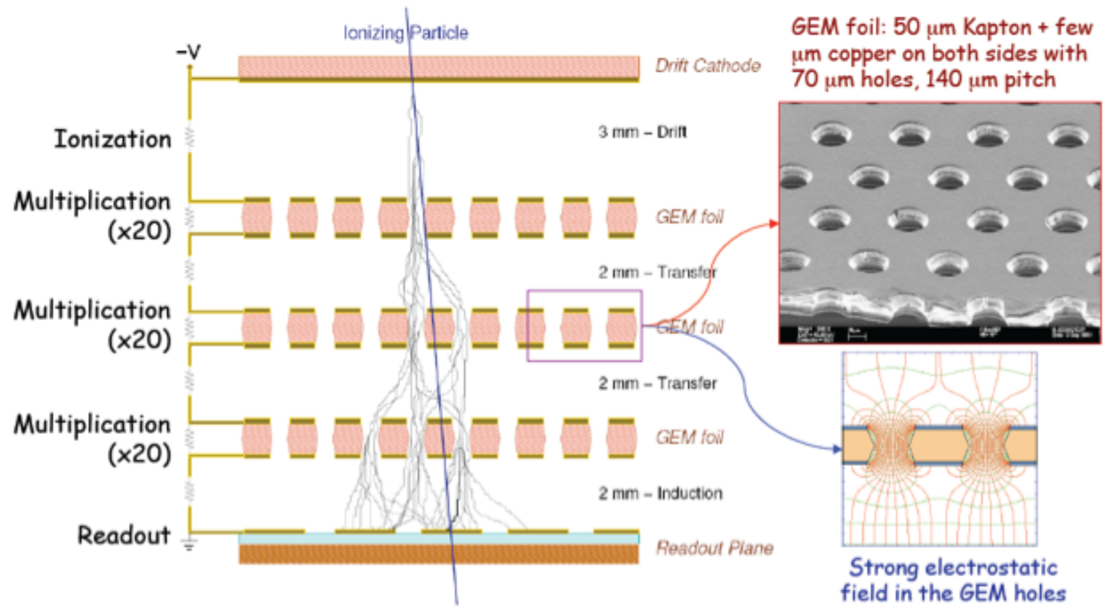

Recent technology: F. Sauli, NIM A 386, 531 (1997)

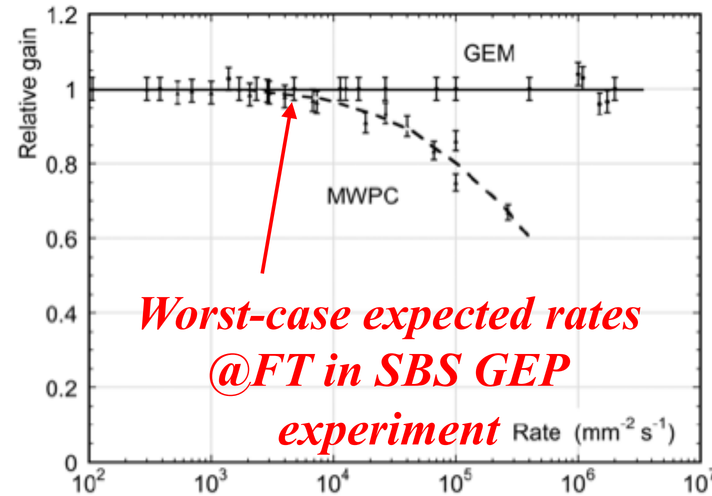

Figure 28.9: Normalized gas gain as a function of particle rate for MWPC [70] and GEM [84].

Stable gain up to very high rates

- High spatial granularity
- Ability to cascade several foils: higher gain at lower voltage, reduced discharge risk
- Readout and amplification stages decoupled
- Excellent spatial resolution ~70 μm
- Fast signals: intrinsic time resolution <10 ns
- **Enabling technology for SBS physics program!**

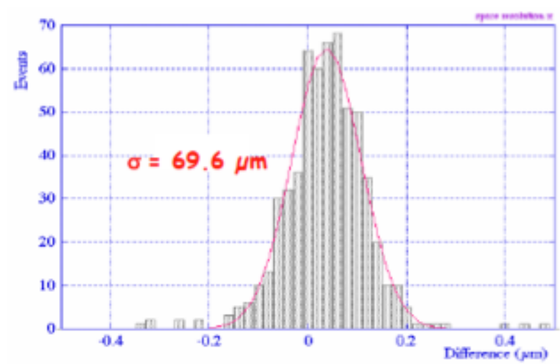

Space resolution

Experiment E12-07-109 (G_{Ep}/G_{Mp} at large Q^2)

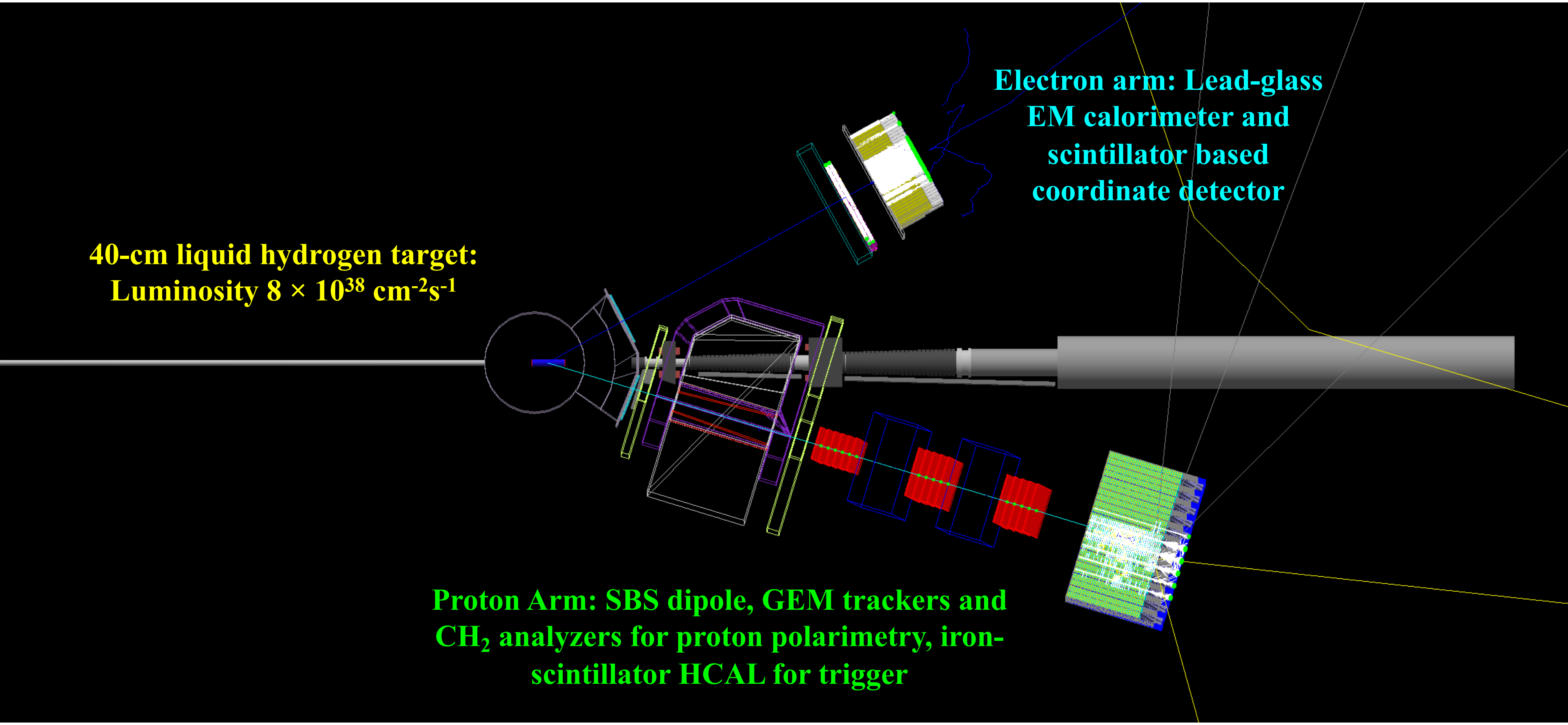

- Original motivation for SBS concept. Need large solid angle to overcome rapidly falling cross section at large Q^2 in elastic *ep* scattering. New double proton polarimeter with GEM-based tracking and hadronic calorimeter-based trigger
- Lead-glass electromagnetic calorimeter to detect the scattered electron in coincidence (using two-body kinematic correlations to aid tracking in high-rate environment and reject inelastic background events); also provides a selective trigger for high-energy electrons.

SBS G_E^p Projected Results

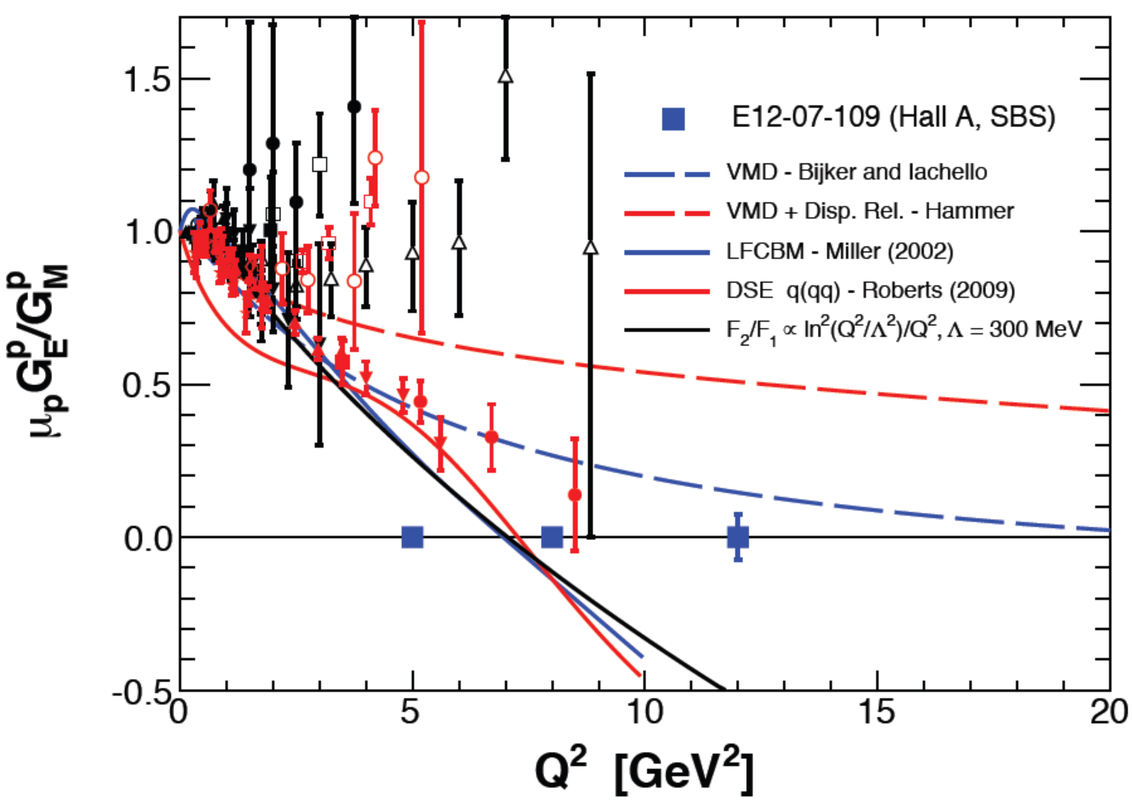

- The SBS GEP experiment in ~11 days running will dramatically improve the statistical precision in $\mu G_E/G_M$ at Q^2 in the range overlapping GEp-II/III, and in 30 days will reach comparable precision at 12 GeV^2 to that of GEp-II/III at 5-6 GeV^2
- Data of such precision carry significant discovery potential and may (or may not) settle the questions of a zero crossing of G_E^p and the onset (or lack thereof) of dimensional scaling.

- Combined with GEN, GMN, GMP experiments, full flavor decomposition of F_1 and F_2 becomes possible up to 10 GeV^2

Kinematics and expected accuracy							
E (GeV)	Q^2 (GeV^2)	θ_E (deg)	P_e (GeV)	Θ_p (deg)	P_p (GeV)	Days	$\Delta\mu G_E/G_M$
6.6	5.0	25.3	3.94	29.0	3.48	1	0.023
8.8	8.0	25.9	4.54	22.8	5.12	10	0.032
11.0	12.0	28.2	4.60	17.4	7.27	30	0.074

Experiment E12-09-019 (G_{Mn} at large Q^2)

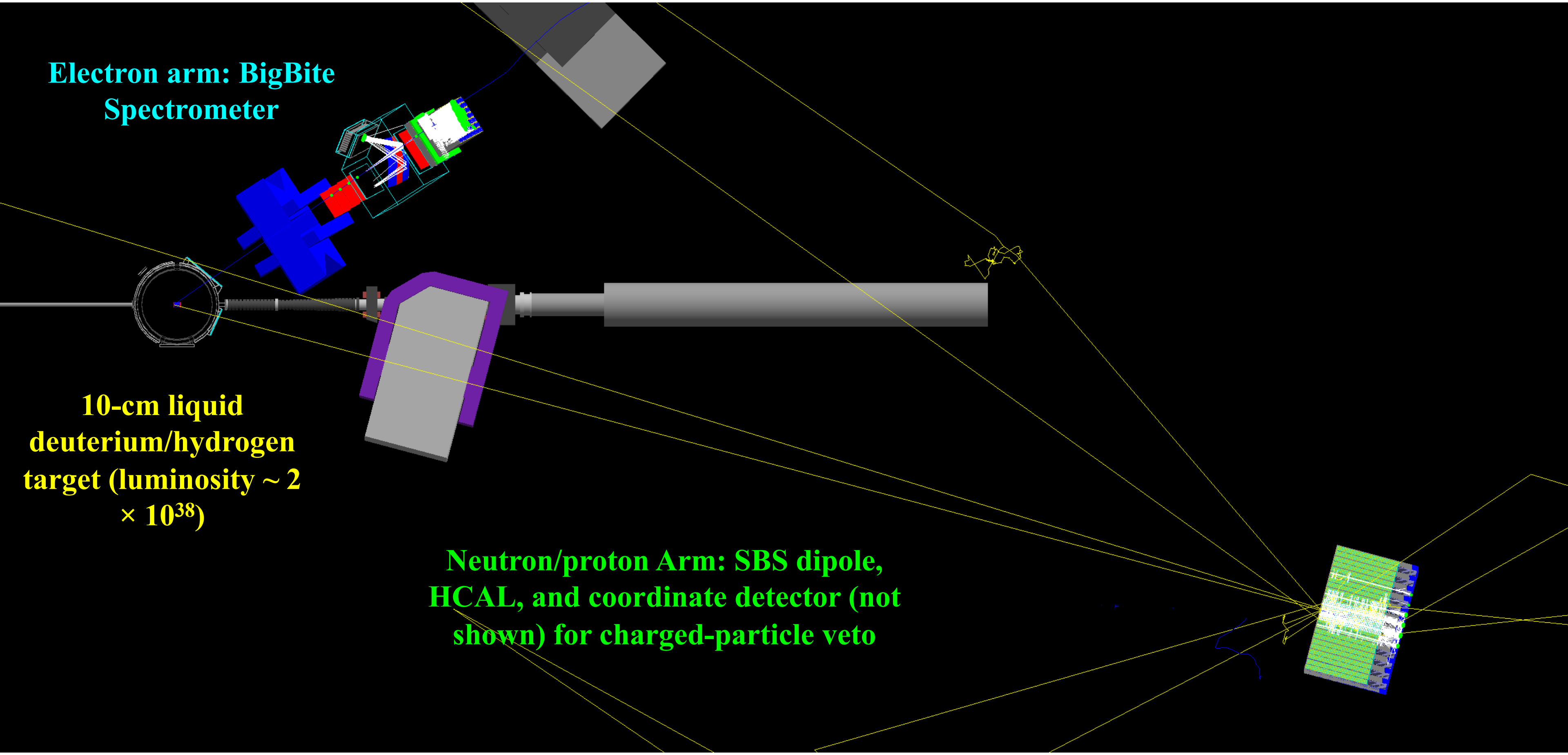

- Neutron magnetic form factor at large Q^2 is obtained from the ratio of quasi-elastic d(e,e'n)p/d(e,e'p)n cross sections on a deuterium target and precise knowledge of elastic ep cross section
- SBS dipole deflects protons to separate from neutrons relative to $\vec{q}$; nucleon momentum is measured using time-of-flight method to separate quasi-elastic/inelastic channels.
- Existing BigBite spectrometer with upgraded detector package detects the scattered electron.

SBS G_{Mn} projected Results

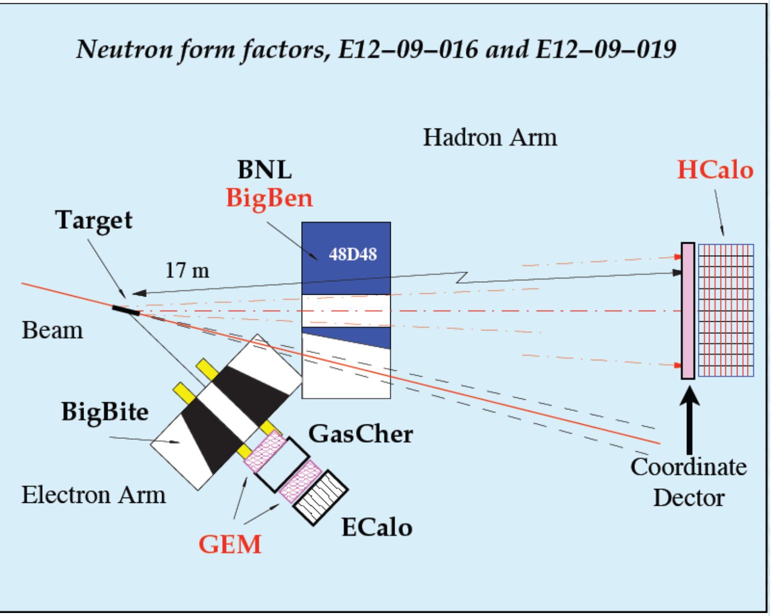

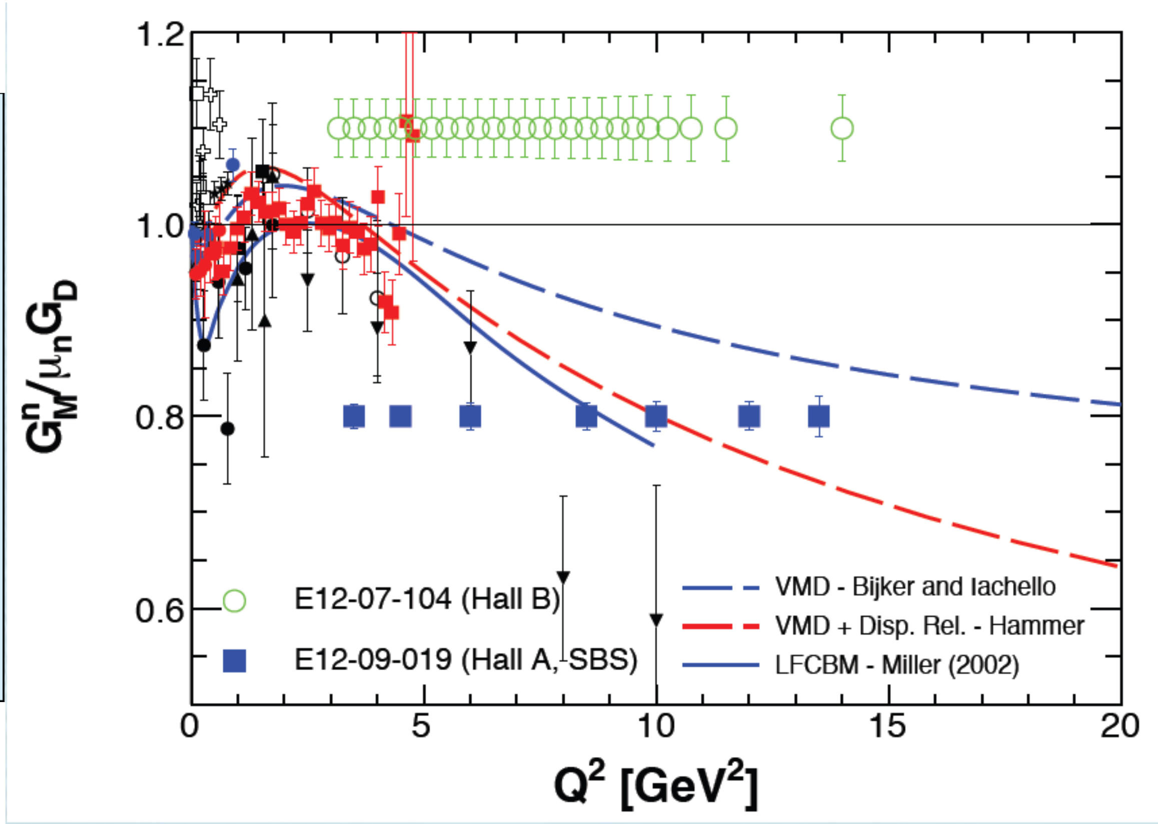

- SBS as neutron arm w/48D48 + HCAL
- Magnet sweeps charged particles out of acceptance, limiting backgrounds and ”CDet” acts as charged-particle veto
- BigBite as electron arm w/upgraded 12 GeV detector package (including re-use of GEMs, built for GEP, not otherwise in use during BigBite expt’s.)
- Standard LH2/LD2 target

Experiment E12-09-016 (G_{E_n} at large Q^2)

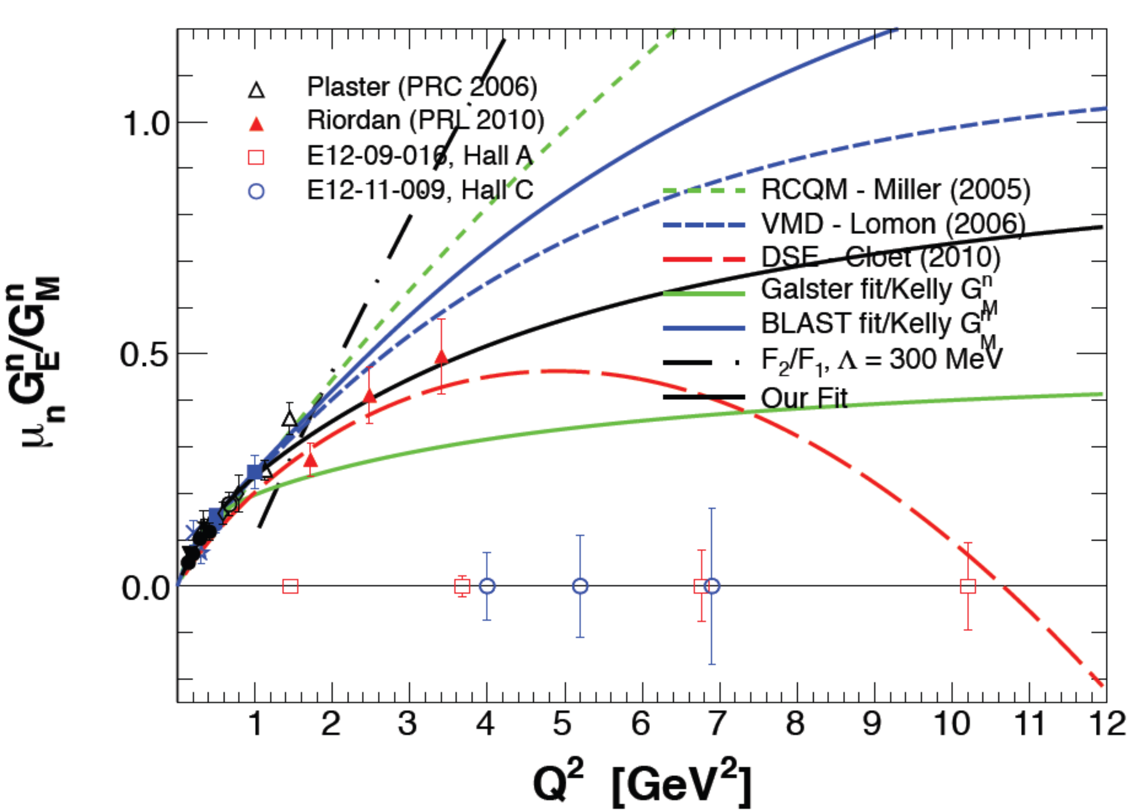

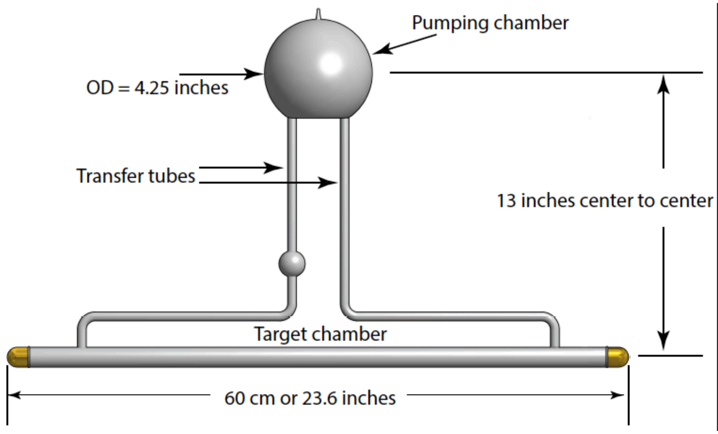

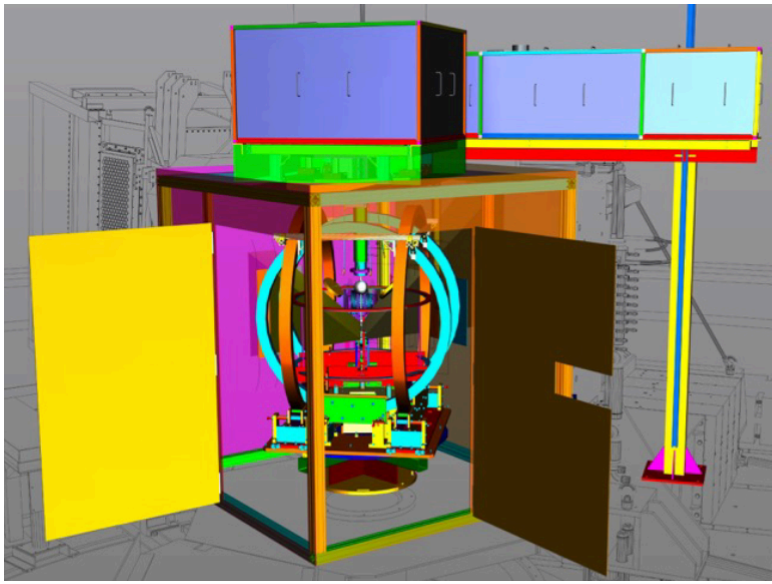

- Detector configuration same as GMN experiment
- High-luminosity polarized ^{3}He target based on spin-exchange optical pumping and convection-driven circulation of polarized gas between optical pumping chamber and target chamber.
- Reach Q^2 = 10 GeV^2 (approximately tripling Q^2 reach of the data)

Conceptual and Engineering Designs of Polarized ^{3}He target

The SBS Form Factor Program—Summary

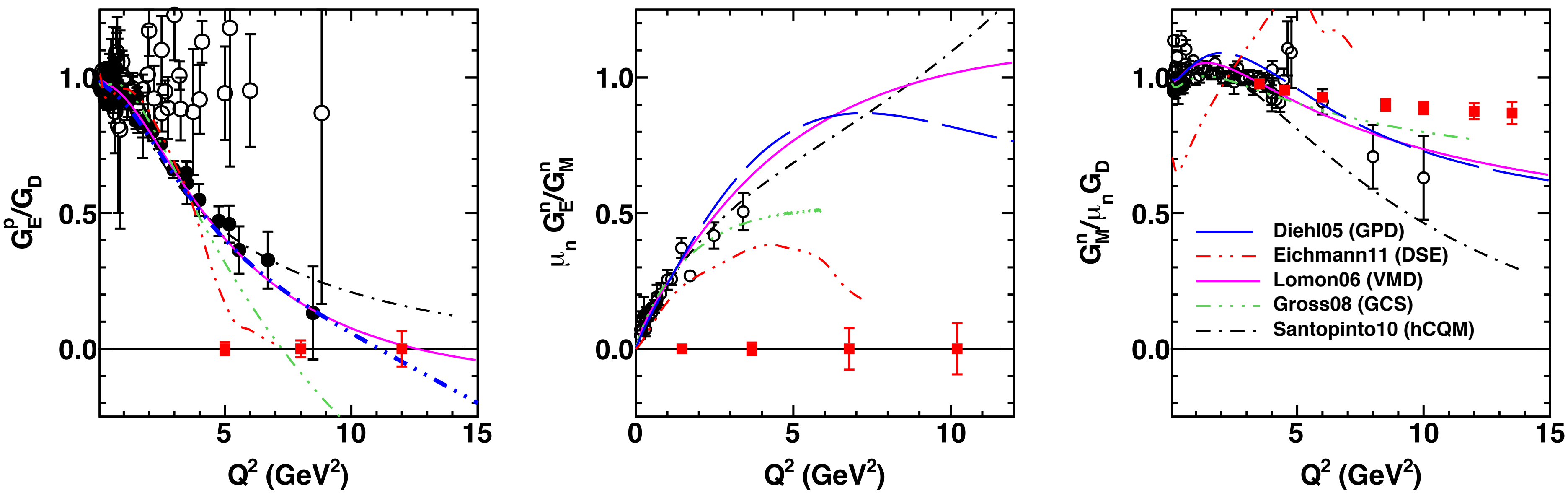

- SBS high-Q^2 form factor program:
  - Map transition to perturbative regime—running of dressed quark mass function
  - Imaging of the nucleon charge and magnetization densities in impact-parameter space in the infinite momentum frame.
  - Precision high-Q^2 form factors have significant impact on GPD extraction from DVCS
- GEP: Proton electric form factor, increase Q^2 range from 8.5 → 12 GeV^2
- GEN: Neutron electric form factor, increase Q^2 range from 3.4 → 10 GeV^2
- GMN: Neutron magnetic form factor, increase Q^2 range from 5 → 13.5 GeV^2

Backup Slides

Neutron form factors: G_M^n

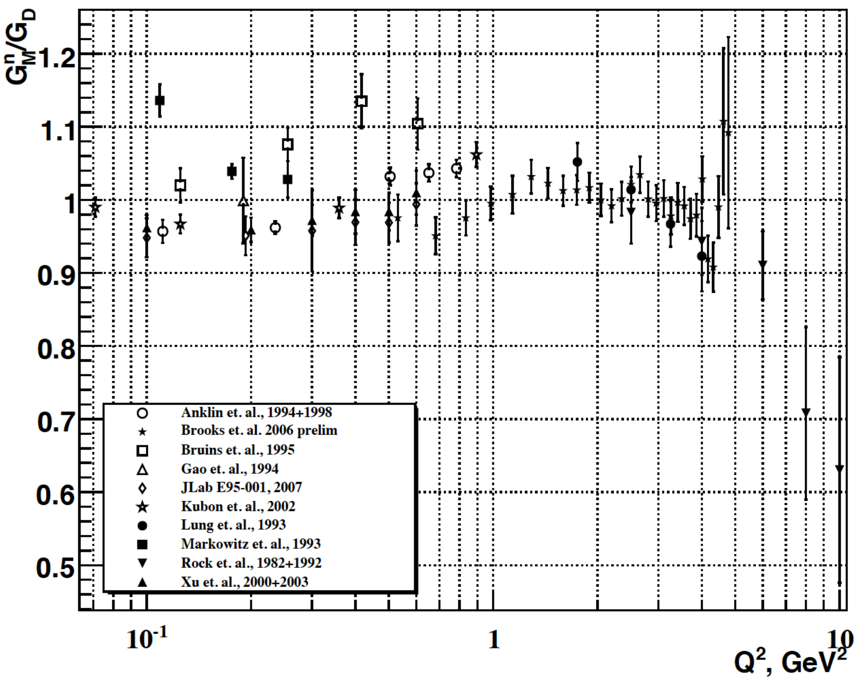

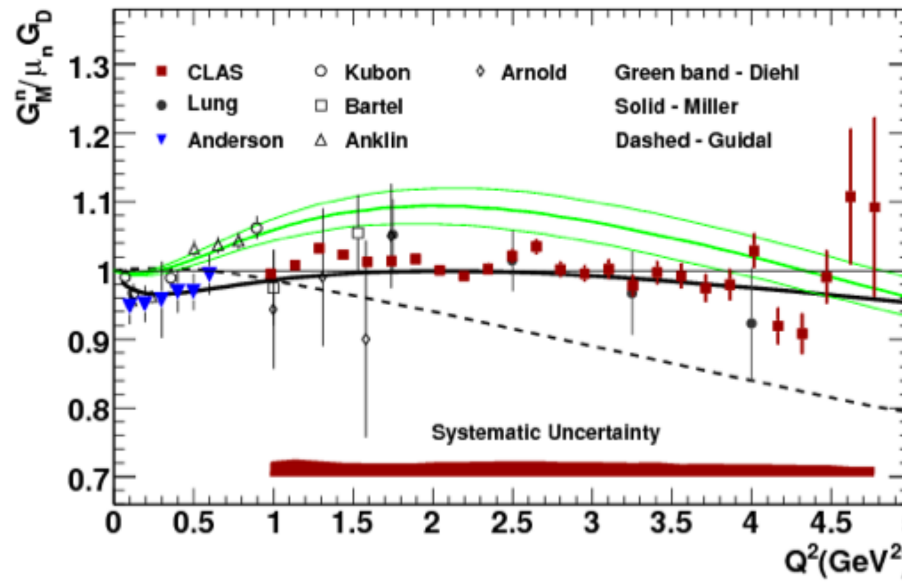

Lachniet *et al.*, CLAS Collaboration, Phys.Rev.Lett. 102 (2009) 192001

- Three main methods have been used to measure G_{Mn}:
  - "Ratio" method: measure cross section ratio of d(e,e'n)p/d(e,e'p)n in quasi-elastic kinematics
  - Absolute d(e,e'n)p quasi-elastic cross section measurement
  - Beam-target double-spin asymmetry* in inclusive quasi-elastic ^{3}He(e,e')

- **Note:** *double-spin asymmetry method for G_{Mn} would not work for a free neutron target, as the free nucleon asymmetry depends only on the ratio G_E/G_M, and not G_E or G_M independently.*
- The widest Q^2 coverage and precision come from recent CLAS 6 GeV data for $1 < Q^2 < 5$ GeV^2—consistent with the "standard" dipole
- Consistency issues exist among low-Q^2 data

Neutron form factors: G_E^n

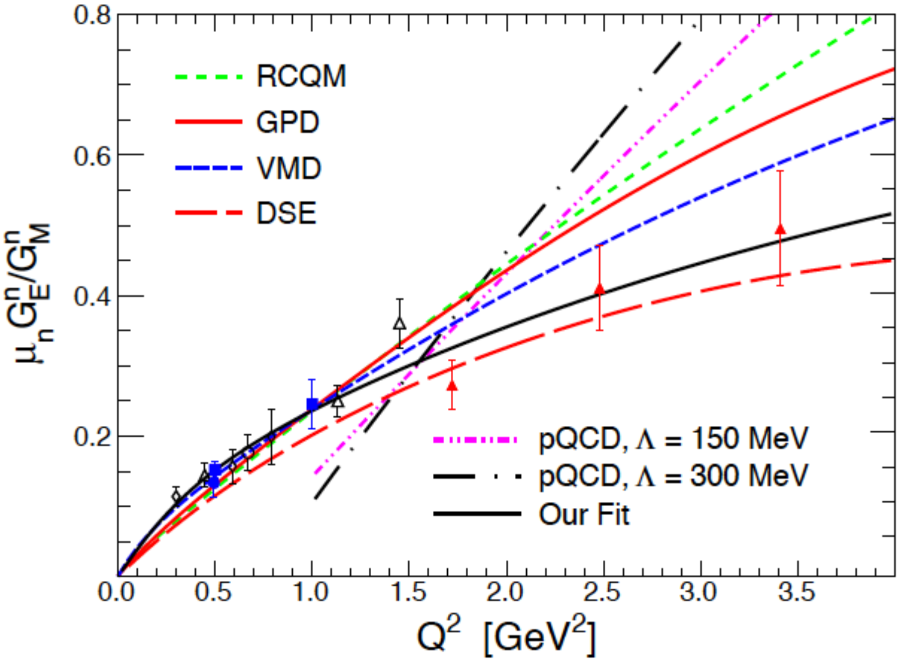

Riordan *et al.*, Phys. Rev. Lett. 105, 262302 (2010)

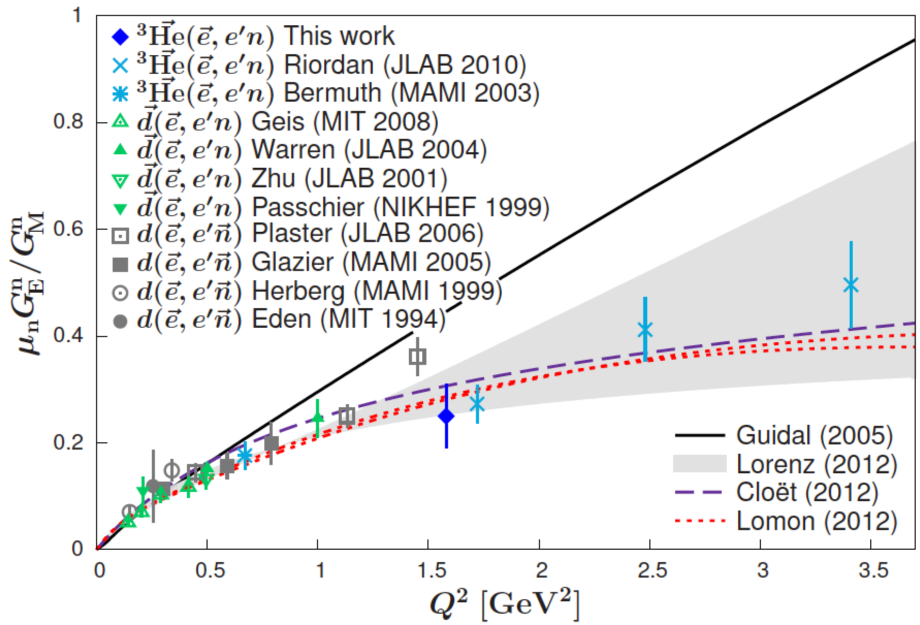

Schlimme *et al.*, Phys.Rev.Lett. 111 (2013), 132504

- G_{En} is the least well-known and most difficult to measure of the nucleon EMFFs:
  - Goes to zero at low Q^2 and cross-section contribution is small at large Q^2
- Existing knowledge is based on polarization observables:
  - Beam-target double-spin asymmetry in semi-exclusive quasi-elastic ^{3}**He**(**e**,e'n)pp
  - Beam-target double-spin asymmetry in semi-exclusive quasi-elastic ^{2}**H**(**e**,e'n)p
  - Neutron recoil polarimetery: d(**e**,e'**n**)p

Custom HMS trigger logic

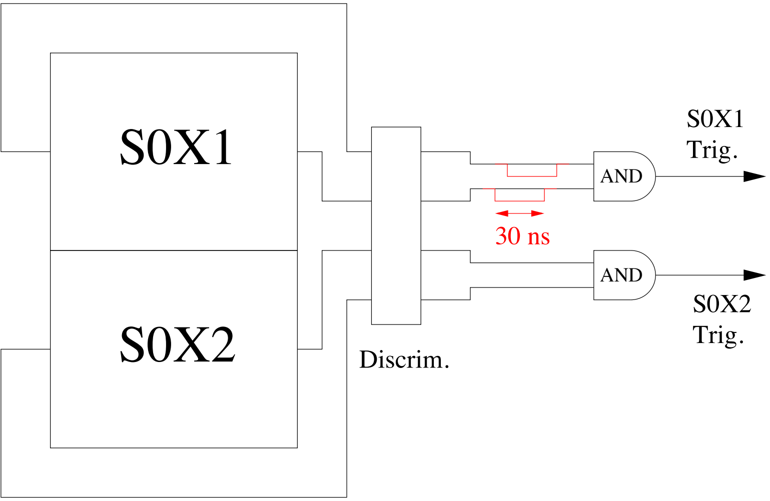

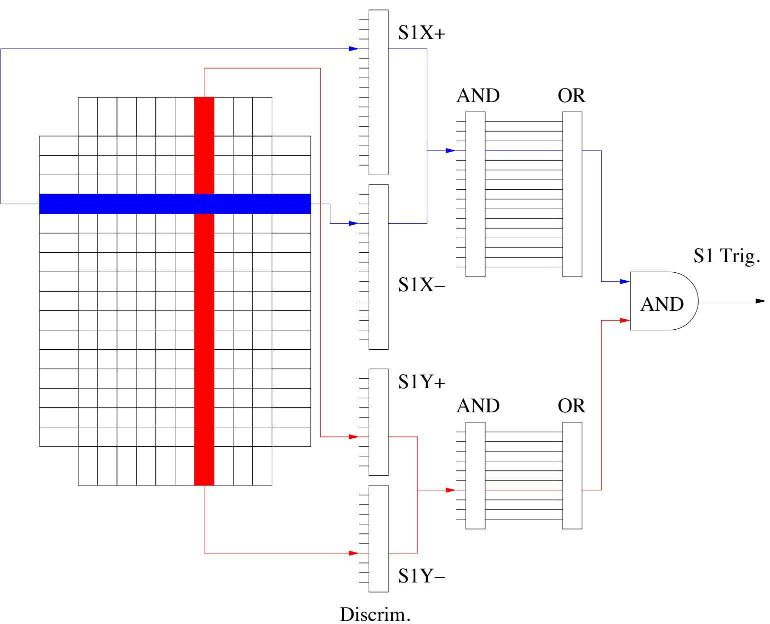

- Because the standard "S2" scintillator planes were removed from the HMS, the requirements applied to the "S1" signals for the GEp-III trigger were somewhat more restrictive (and potentially less efficient) than the "standard" requirements.
  - At least one paddle with both PMTs firing was required in both "S1X" and "S1Y"
- A distinguishing feature of the proton trigger for GEp-III (in common with GEp-I/II) was that the proton trigger was formed entirely prior to the secondary polarization-analyzing scattering in CH_2, such that the trigger could not be biased according to scattering direction in the FPP.
- Since GEp-III did not intend to measure absolute cross sections, some efficiency losses were deemed acceptable.
- For all but two production kinematics, the HMS trigger was a coincidence between "S0" and "S1"
  - For the kinematics with the largest HMS central angle, the HMS trigger was based on"S1" only
- "S0" and "S1" triggers were found to be nearly 100% efficient in any case.

BigCal Trigger Logic

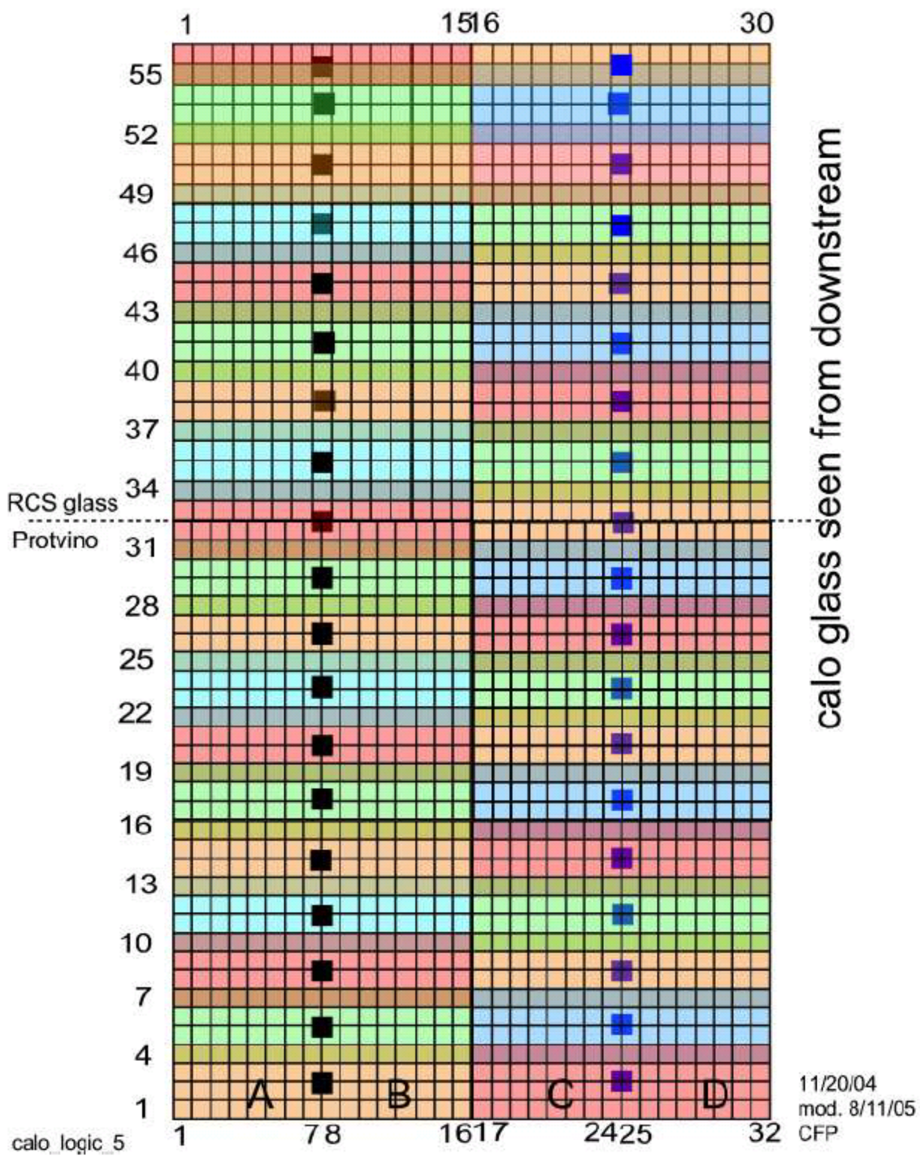

- Eight-channel analog (NIM) summing modules were used to form the trigger, and to amplify the signals (4.2X) before transmission to readout electronics
- Amplification of the signals allowed operation of PMTs at lower gain, for lower power consumption and longer lifetime
- "First-level" sums-of-8 were combined using the same summing modules into "second-level" sums-of-64, grouped with partial overlap to avoid regions of inefficiency.
- A global logical "OR" of all 38 "second-level" sums with a threshold equivalent to roughly half the elastically scattered electron energy defined the BigCal trigger
- The main DAQ trigger was defined by a coincidence between the BigCal and HMS trigger signals within a (typically) 50-ns window
- Lack of overlap in trigger logic between left and right halves limits threshold to less than half of the elastically scattered electron energy to insure high, uniform efficiency

Coincidence Trigger Logic

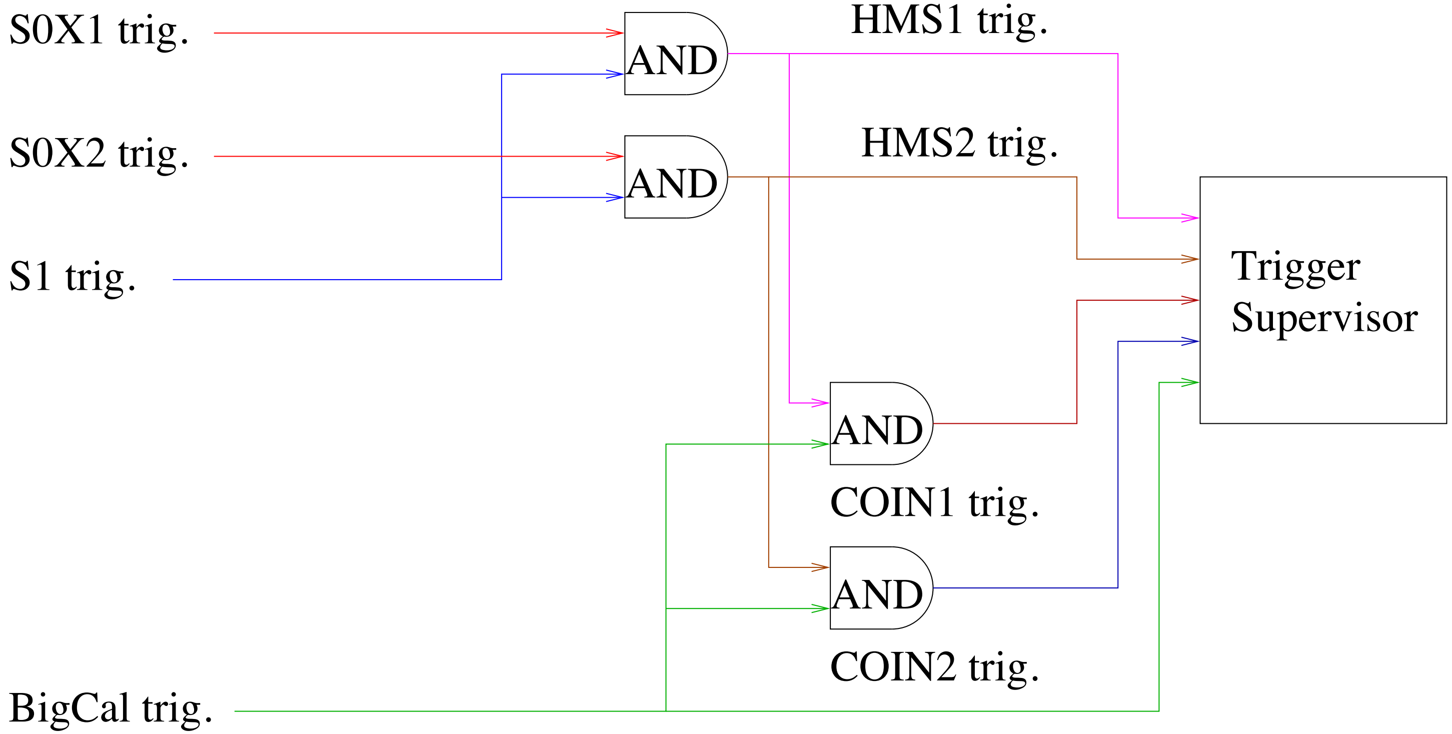

- Separate singles and coincidence triggers were defined for each of the two paddles of “S0”
- These two coincidence triggers could be prescaled separately by the DAQ system
- The “S0X2” paddle covers the center of the HMS focal plane, while “S0X1” covers the lower-momentum (inelastic) region
- For some kinematics, the entire envelope of elastically scattered protons was cointained within “S0X2”, and “S0X1” was dominated by inelastics, and could thus be heavily prescaled.
- For other kinematics, elastic protons were spread out over both paddles.

Overview of new/final analysis of the Hall C data

- Goal: Improve understanding of systematic uncertainties in order to publish full-acceptance results from GEp-2γ and final archival results from GEp-2γ and GEp-III.
- Major aspects of event reconstruction/calibration revisited:
  - **HMS optics calibration: angle and vertex reconstruction**
  - **HMS and FPP time-to-distance calibration performed run-by-run (and card-by-card for FPP drift chambers)**
  - **Improved FPP-HMS drift chamber alignment from straight-through data**
  - Minor improvements/bug fixes to HMS/FPP tracking algorithms
  - Recalibration of BigCal energy reconstruction for some run ranges
  - Minor improvements to BigCal shower coordinate reconstruction
  - Updated beam position/energy database from EPICS (beam position + raster corrections important for momentum/out-of-plane angle reconstruction)
  - More thorough run-by-run data quality checks
    - Exclusion of runs with significant FPP data quality issues from GEp-2gamma analysis (minimize false asymmetries)
    - Fix minor problems with beam polarization database
- Major aspects of physics analysis revisited:
  - Refined elastic event selection cuts
  - Improved "fully differential" description of the analyzing power for $Q^2 = 2.5$ GeV^2
  - Bin-centering corrections for full-acceptance data at 2.5 GeV^2
  - More thorough analysis of the non-dispersive-plane optical study of the HMS to reduce systematic uncertainties due to spin precession calculation.
  - Final evaluation of systematic uncertainties

Data quality checks ($\mu_p G_E^p / G_M^p$)—Analyzing power cancellation

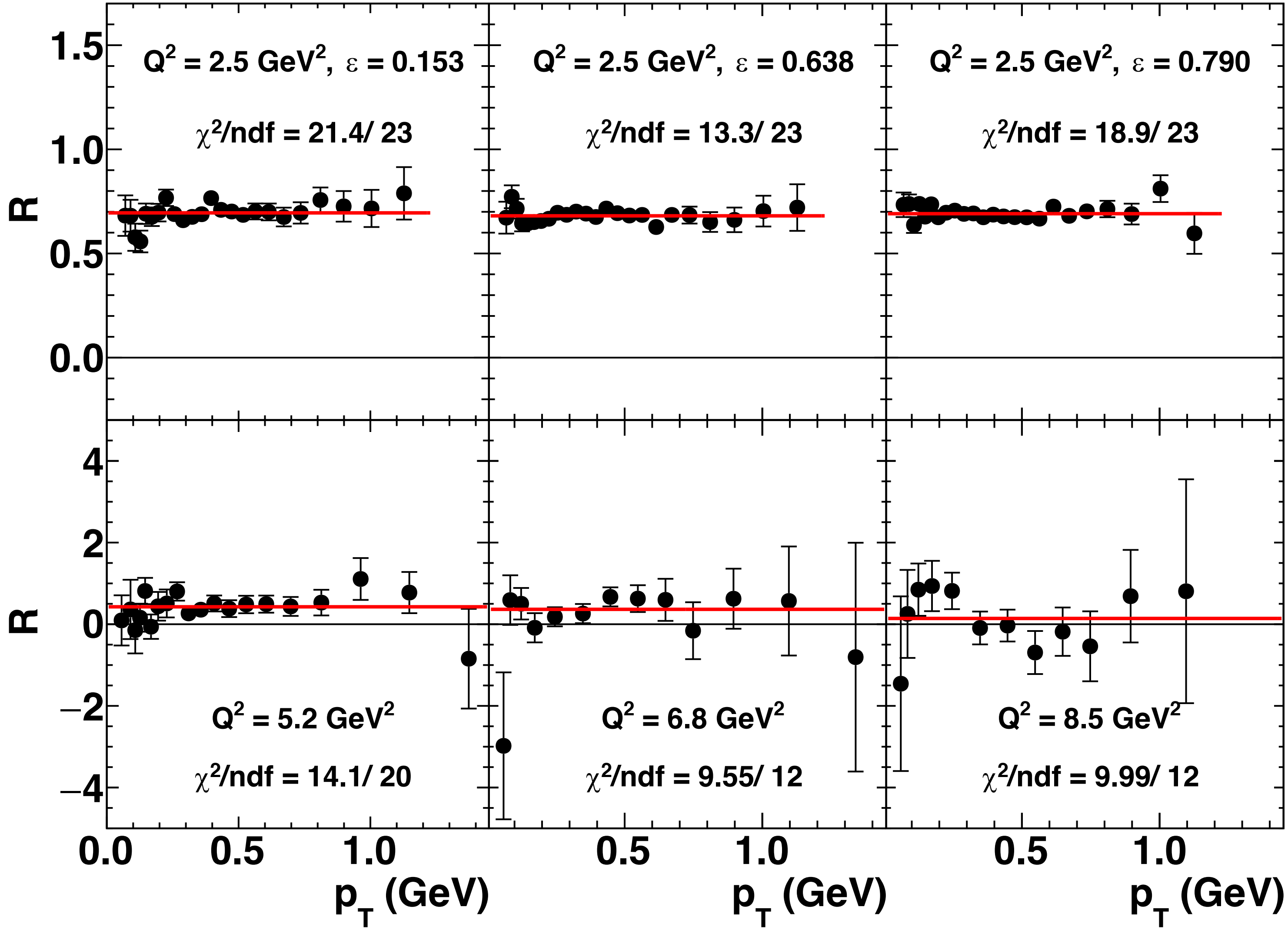

- The constancy of the extracted FF ratio as a function of $p_T = p_p \sin\vartheta$ confirms the cancellation of A_y in the ratio P_t/P_ℓ

Data quality checks ($\mu_p G_E^p/G_M^p$)—kinematic dependence

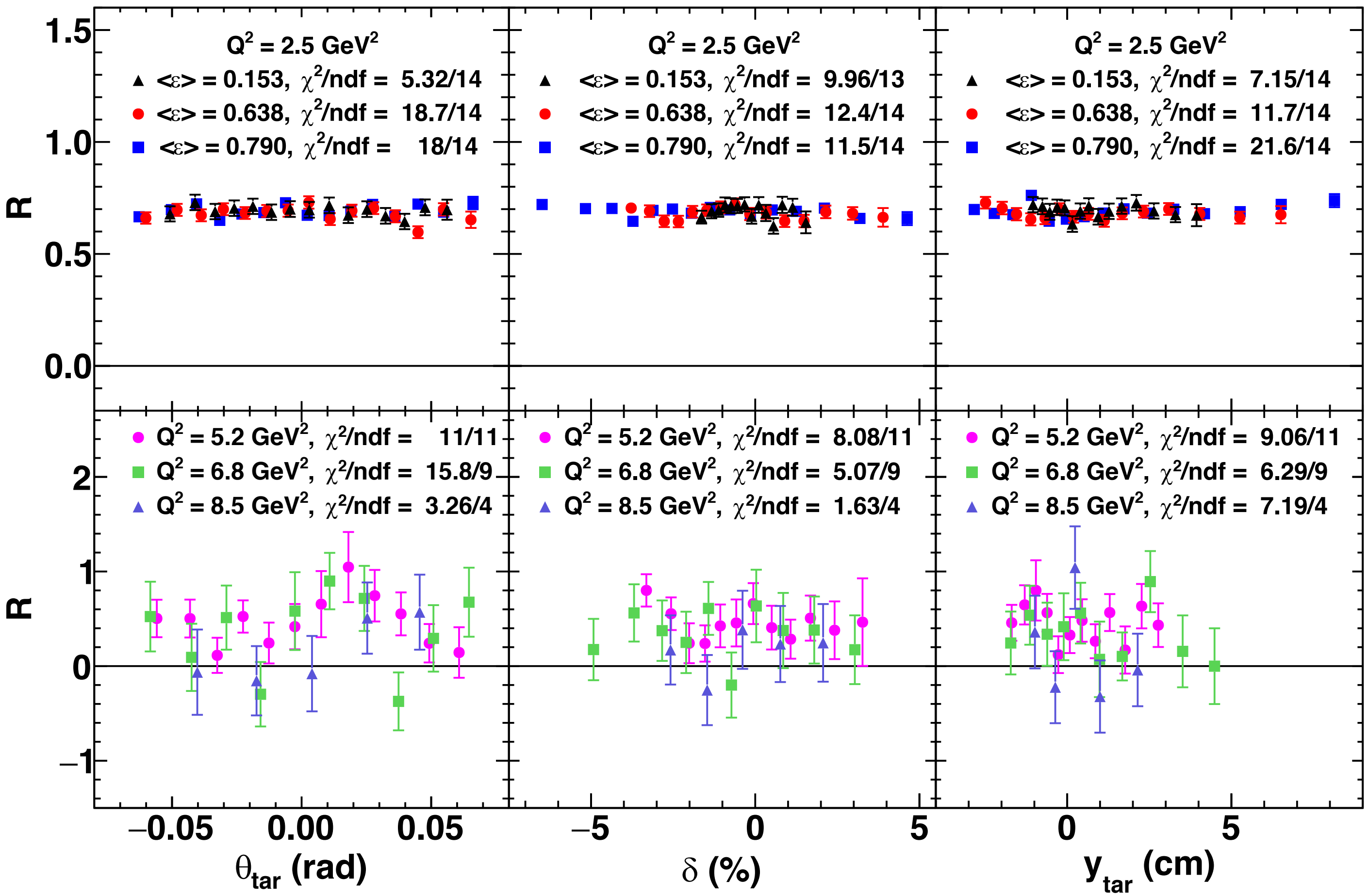

$$\chi^2 \equiv \sum_i \frac{\left(\frac{R_i}{R_0(Q_i^2)} - \bar{R}\right)^2}{\sigma_i^2},$$

$$\bar{R} \equiv \frac{\sum_j \frac{R_j}{\sigma_j^2 R_0(Q_j^2)}}{\sum_k \frac{1}{\sigma_k^2}},$$

$$\sigma_i^2 \equiv \left(\frac{\Delta R_i}{R_0(Q_i^2)}\right)^2,$$

- The absence of spurious dependence of the extracted FF ratio on the reconstructed proton kinematics validates the ML method for the extraction of R and the accuracy of the HMS optics and spin transport calculation.
- Here χ^2 is computed with respect to the ratio of R to its “expected” value based on a global proton FF fit, to account for the Q^2 dependence of R within the acceptance.

Data quality checks (P_ℓ/P_ℓ^{Born})—A_y momentum dependence

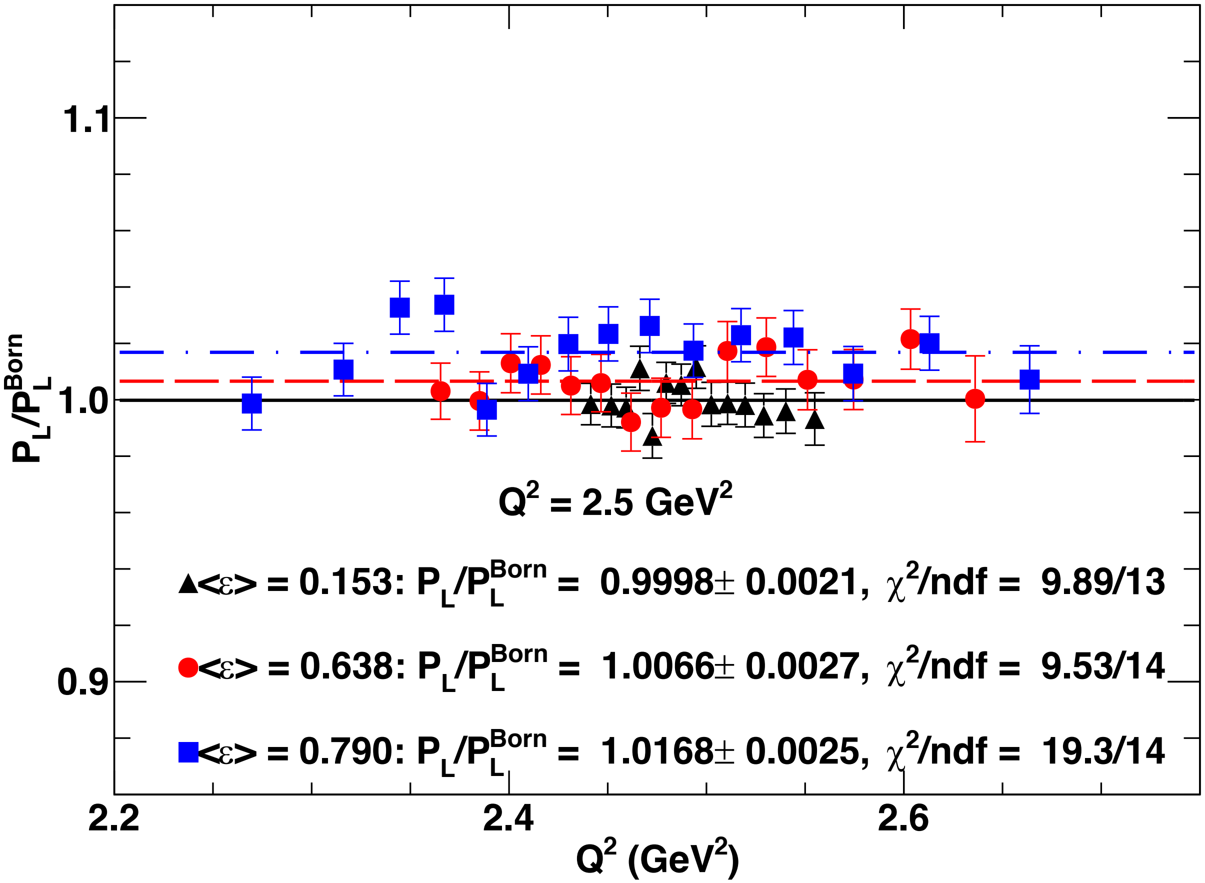

- The overall proton momentum dependence of the analyzing power is assumed to factorize from the angular dependence, according to:

$$A_y(p_p, p_T) = A_y^0(p_T)\frac{\bar{p_p}}{p_p},$$

- The application of identical cuts on the scattering parameters $s_{close}, z_{close}, p_T$ insures that the average analyzing power for the three ϵ values is the same, up to differences in the momentum distribution of incident protons.

- Measuring the *relative* ϵ dependence of P_ℓ/P_ℓ^{Born} at 2.5 GeV² relies on the assumption that the average analyzing power is the same for all three kinematics, up to an overall $\frac{1}{p_p}$ scaling which accounts for the differences in Q^2 acceptance/average Q^2 between the different kinematics.
- The lowest ϵ point is used to calibrate A_y under the assumption $P_\ell = P_\ell^{Born}$, since $P_\ell^{Born} \to 1$ as $\epsilon \to 0$, and is thus very insensitive to the FF ratio ($P_\ell^{Born} = 0.9753 \pm 0.0003$ at $< \epsilon > = 0.153$).

Data quality checks—Beam Polarization Database

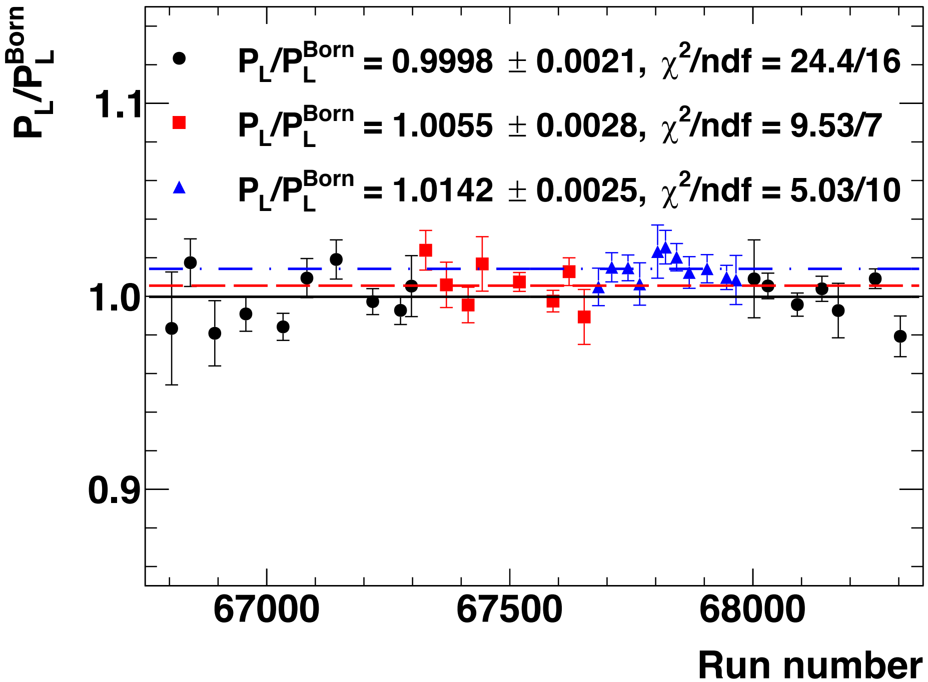

Extracted $\frac{P_\ell}{P_\ell^{Born}}$ vs. run number during GEp-2γ

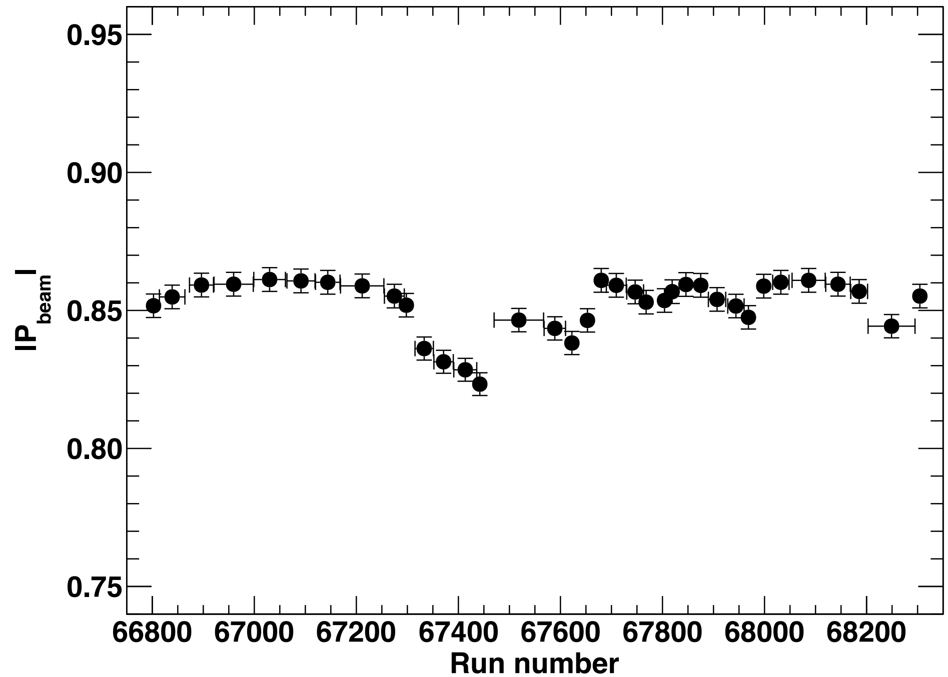

Moller measurements of beam polarization during GEp-2γ with associated run ranges

- Moller measurement of beam polarization was carried out roughly every 2 days during GEp-2γ. As an intrusive measurement, data taking had to be interrupted to measure polarization; no ”online” monitoring of beam polarization was possible, except via FPP asymmetry magnitude.
- Stability of extracted $\frac{P_\ell}{P_\ell^{Born}}$ confirms validity of beam polarization database and stability of beam polarization between Moller measurements.

HMS Spin Transport Systematics—non-dispersive plane

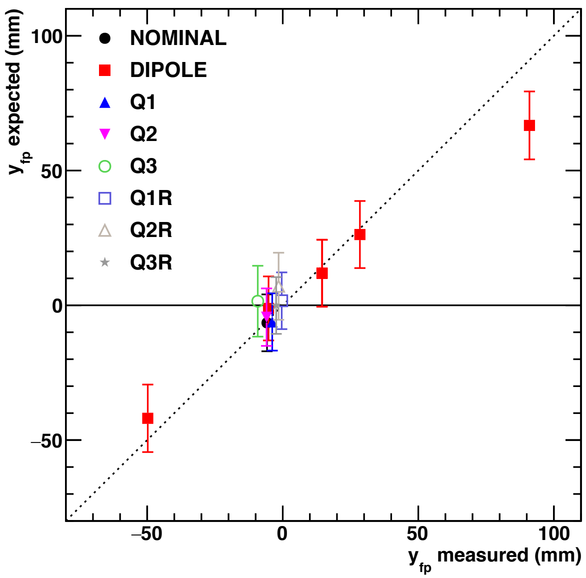

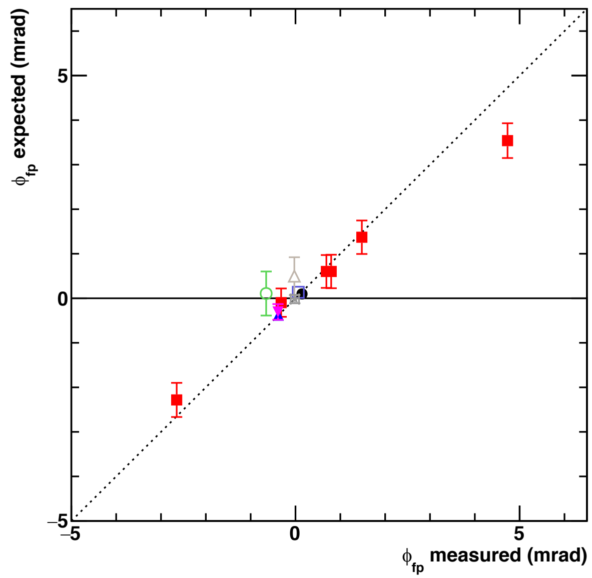

$$
\begin{aligned}
S_{yt} &\approx \cos\chi_\phi \\
S_{y\ell} &\approx \sin\chi_\phi \\
S_{xt} &\approx \sin\chi_\phi \sin\chi \\
S_{x\ell} &\approx -\cos\chi_\phi \sin\chi \\
\chi_\phi &\equiv \gamma\kappa_p(\phi_{fp} - \phi_{tar}) \\
&\equiv \gamma\kappa_p\phi_{bend} \\
\chi &\equiv \gamma\kappa_p\theta_{bend}
\end{aligned}
$$

$$
\begin{aligned}
\phi_{bend}^{(s)} &= \sum_i (\phi_{fp}|s_i)s_i \\
\phi_{bend}^{(total)} &= \phi_{bend}^{(s)} + \phi_0^{fp} + (\phi_{fp}|y_{tar})y_0^{tar} \\
&+ [(\phi_{fp}|\phi_{tar}) - 1]\frac{y_{sieve} - y_0^{tar}}{z_{sieve}},
\end{aligned}
$$

$$
R = -K\frac{P_t}{P_\ell} = K\frac{\tan(\chi_\phi) + \sin(\chi)\frac{P_y^{FPP}}{P_x^{FPP}}}{1 - \tan(\chi_\phi)\sin(\chi)\frac{P_y^{FPP}}{P_x^{FPP}}}
$$

$$
R = -K\frac{P_t}{P_\ell} \approx K\left[\chi_\phi + \sin(\chi)\frac{P_y^{FPP}}{P_x^{FPP}}\right],
$$

$$
K \equiv \mu_p\sqrt{\frac{\tau(1+\epsilon)}{2\epsilon}}
$$

- FF ratio is highly sensitive to HMS non-dispersive bend angle at high Q^2
- At 8.5 GeV^2, $\frac{dR}{d\phi_{bend}} = -\frac{0.1}{mrad}$

$y_0^{fp} \pm \Delta y_0^{fp}$ (mm)	0 ± 10	0 ± 2
$\phi_0^{fp} \pm \Delta\phi_0^{fp}$ (mrad)	-0.05 ± 0.18	-0.03 ± 0.07
$y_0^{tar} \pm \Delta y_0^{tar}$ (mm)	-0.3 ± 0.2	-0.3 ± 0.1
$s_1 \pm \Delta s_1$ (mm)	0.8 ± 0.3	0.7 ± 0.1
$s_2 \pm \Delta s_2$ (mm)	1.0 ± 0.7	1.1 ± 0.2
$s_3 \pm \Delta s_3$ (mm)	2.7 ± 1.3	3.1 ± 0.8
$\phi_{bend}^{(s)} \pm \Delta\phi_{bend}^{(s)}$ (mrad)	0.16 ± 0.18	0.13 ± 0.07
$\phi_{bend}^{(total)} \pm \Delta\phi_{bend}^{(total)}$ (mrad)	0.12 ± 0.14	0.13 ± 0.08
χ^2/ndf	$22.2/21$	$35.1/21$

HMS Spin Transport Systematics—dispersive plane

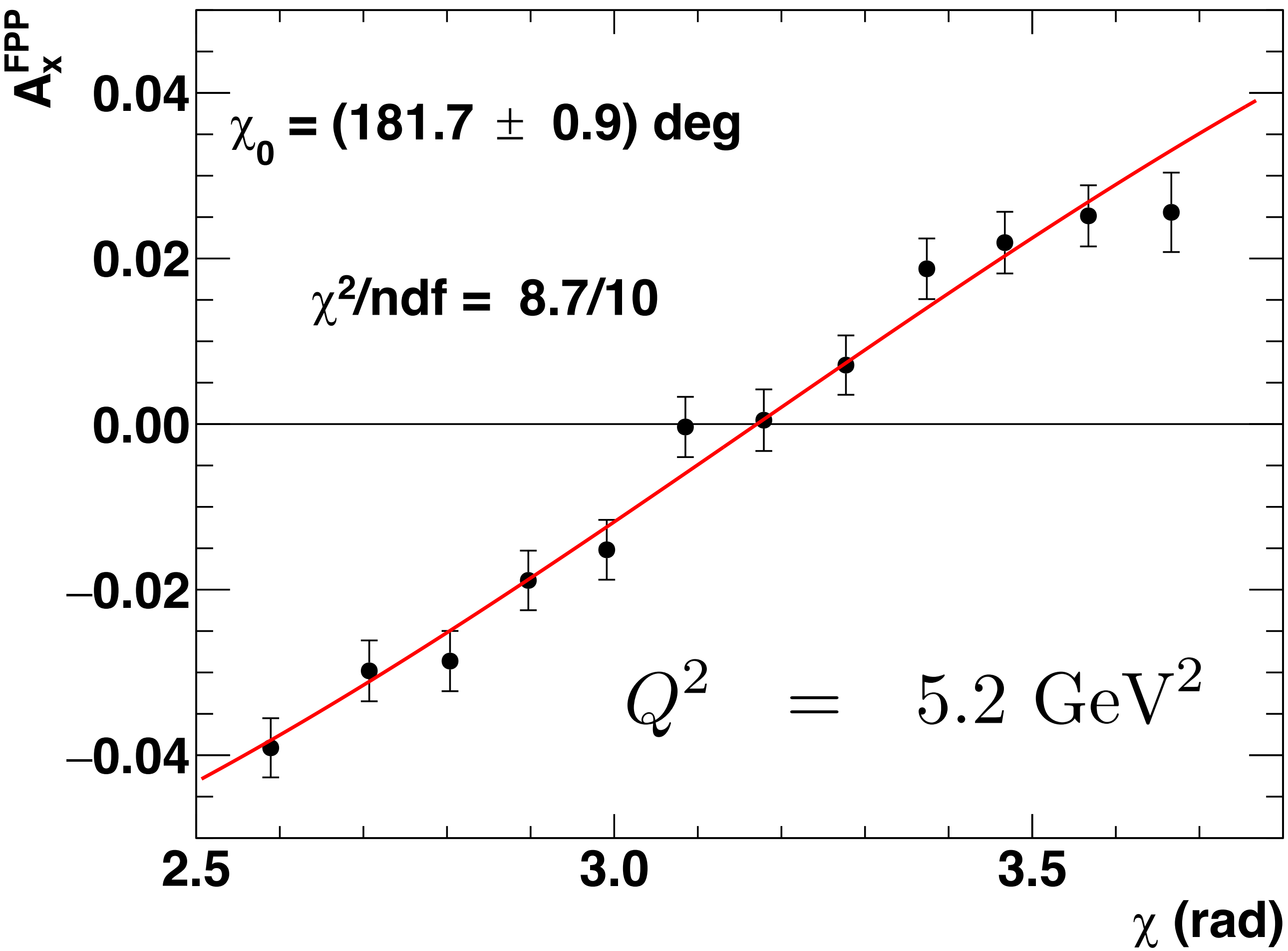

$$\begin{aligned}\text{Expected } \chi_0 &= (180.42 \pm 0.02)^\circ \\ \text{Measured } \chi_0 &= (181.7 \pm 0.9)^\circ \\ \Delta\theta_{bend} &\approx \frac{\Delta\chi_0}{\gamma\kappa_p} = 3.2 \text{ mrad}\end{aligned}$$

- Systematic uncertainty in dispersive-plane total bend angle estimated from asymmetry zero crossing at 5.2 GeV^2

High-Q² Nucleon Form Factors, GPDs and Spin

Flavor decomposition of nucleon EMFFs (neglecting strangeness):

$$F^p_{1,2} \approx e_u F^u_{1,2} + e_d F^d_{1,2}$$

$$F^n_{1,2} \approx e_u F^d_{1,2} + e_d F^u_{1,2}$$

Quark flavor FFs are integrals of valence quark GPDs H and E at zero skewness :

$$F^q_1(t) = \int_0^1 H^q_v(x,t)dx$$

$$F^q_2(t) = \int_0^1 E^q_v(x,t)dx$$

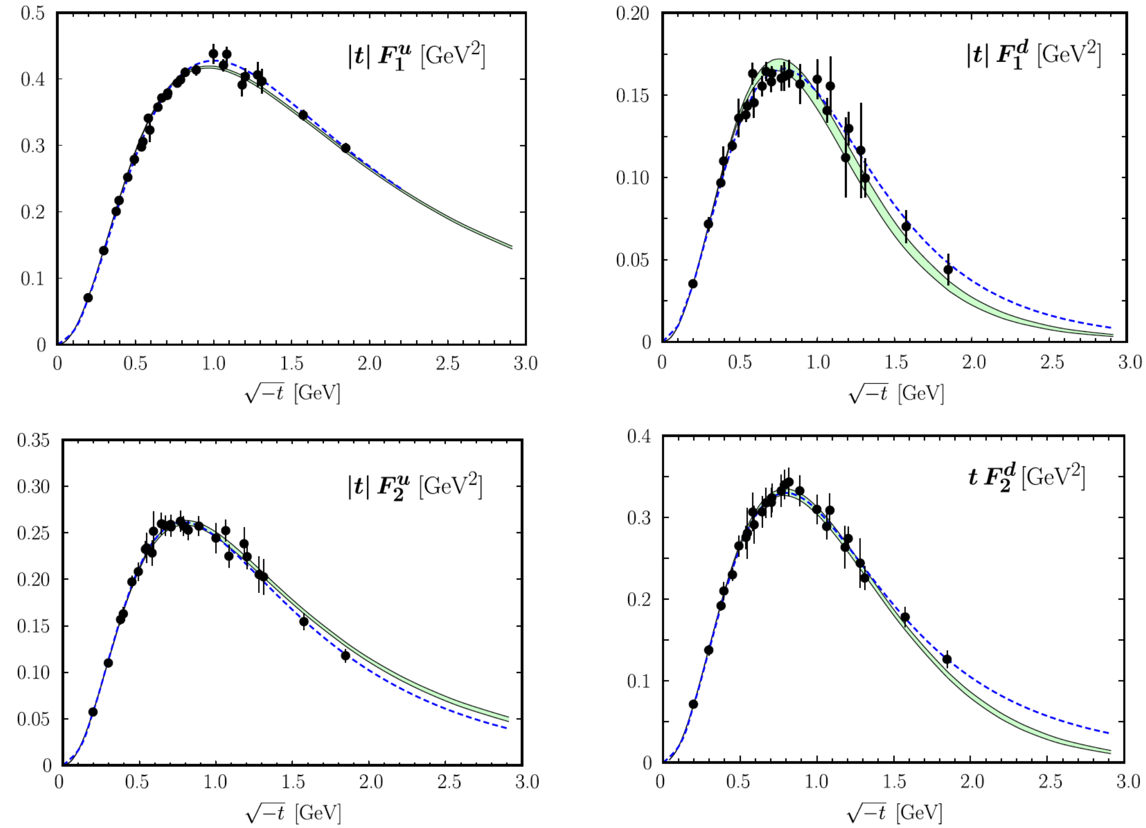

Phys.Rev.Lett. 78 (1997) 610-613: Ji sum rule for total angular momentum

$$J_q = \frac{1}{2}\int_{-1}^{+1} dx x[H^q(x,\xi,t=0) + E^q(x,\xi,t=0)].$$

Diehl, Kroll. Eur. Phys. J. C (2013) 73:2397

- FF data + forward PDFs from global DIS fits → model-dependent extraction of GPDs
- Compute valence-quark contributions to the Ji sum rule: $J^u_v = 0.230^{+0.009}_{-0.024}, \qquad J^d_v = -0.004^{+0.010}_{-0.016}$

The under-appreciated importance of knowledge of the high-Q^2 FFs in the extraction of GPDs from experiment

From the recent paper by **M. Diehl and P. Kroll. Eur. Phys. J. C (2013) 73:2397**

- “This requires an ansatz for the functional form of the GPDs and in this sense is intrinsically model dependent, but on the other hand it can reach values of the invariant momentum transfer t much larger than what can conceivably be measured in hard exclusive scattering...”
- “We note that the electromagnetic form factors provide indirect constraints on GPDs at high values of t, which will conceivably never be accessible in hard exclusive scattering processes.”

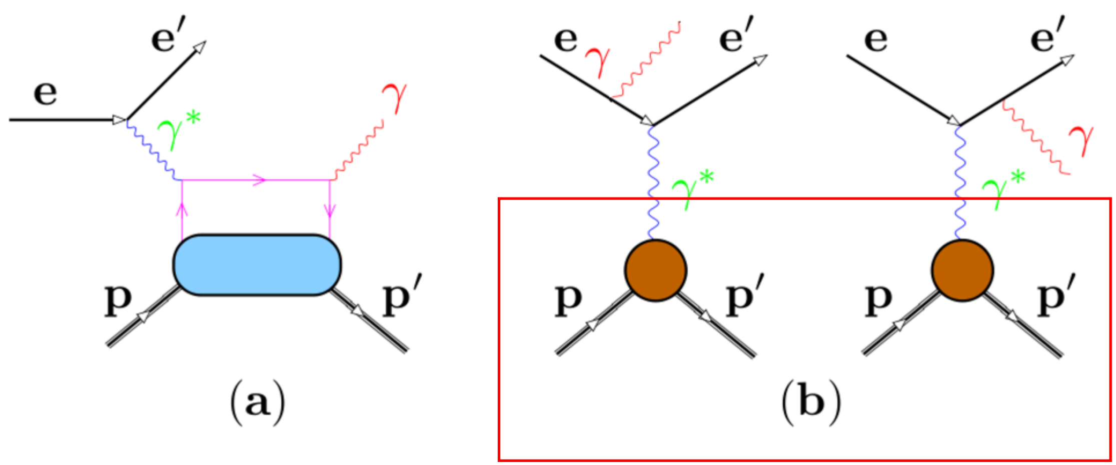

- DVCS experiments actually measure the interference of Bethe-Heitler and DVCS handbag mechanism at the same order of $\alpha \rightarrow$ precise knowledge of elastic FFs is needed to separate DVCS contribution!
- EMFFs thus provide both direct constraints to GPDs via the sum rules and crucial input to the extraction of Compton Form Factors from experimental observables

Polarization Transfer FOM vs. Q^2: HMS/HRS vs SBS

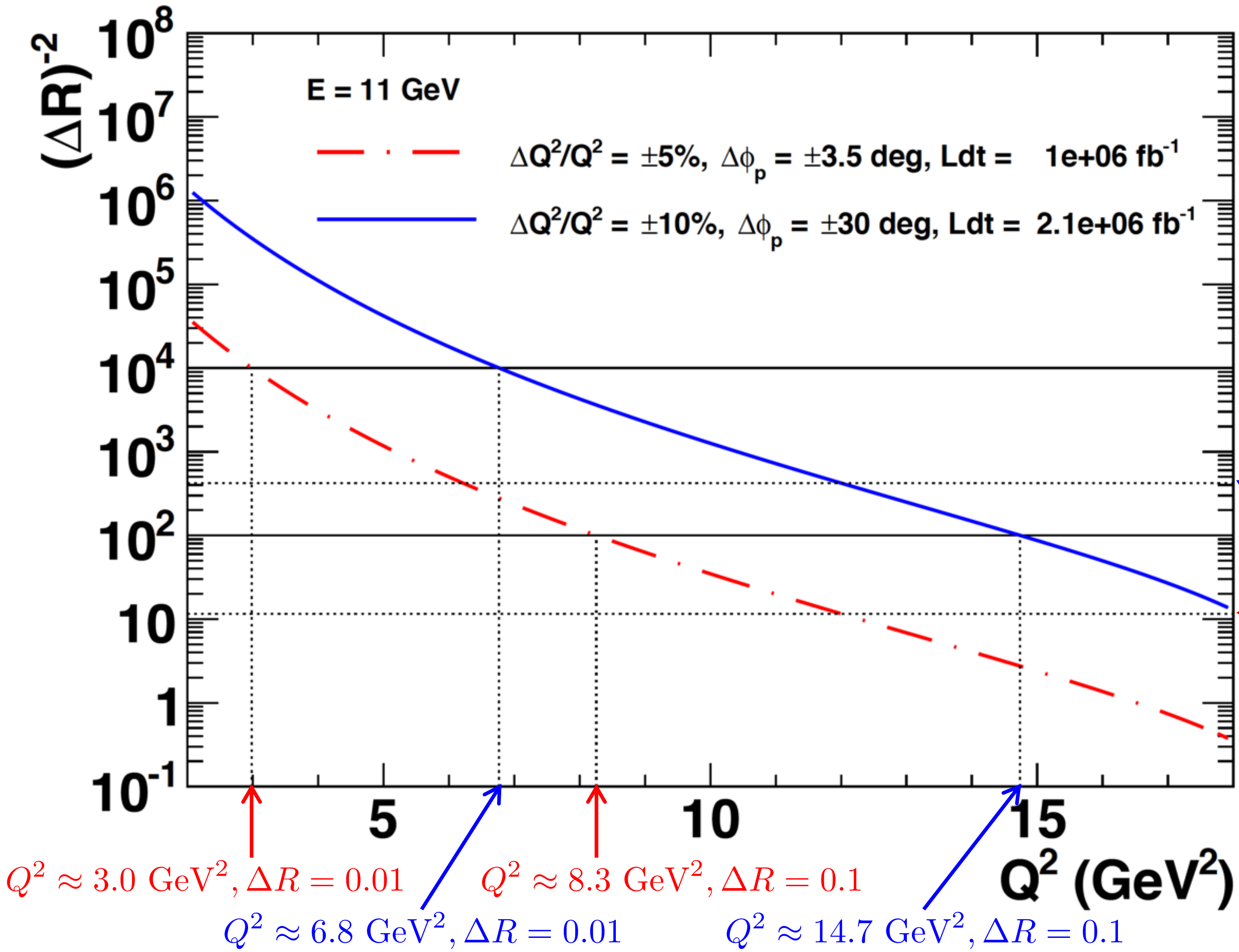

$\Delta R \approx 0.05, Q^2 = 12$ GeV^2

$\Delta R \approx 0.3, Q^2 = 12$ GeV^2

Assumptions:

- 11 GeV beam energy
- 85% beam polarization
- FPP coefficient of merit scaled by $1/Q^2$ relative to Hall C $Q^2 = 8.5$ GeV^2 result
- Integrated luminosity corresponds to ~30 day experiment at 100% efficiency on **20-cm**/**40-cm** LH_2 target

Increase in proton solid angle from 6→35 msr and ~2X increase in luminosity leads to *doubling* of Q^2 range for which absolute $\Delta(\mu G_E/G_M) \leq 0.1$

Statistical FOM of PT expt.'s

Experiment	Q^2 $(\mathrm{GeV/c})^2$	E_e (GeV)	$\Delta\Omega_p$ (msr)	P_e (%)	$\Delta\left(\mu_p G_E^p/G_M^p\right)$	Reference
GEp-I	0.5-3.5	0.9-4.1	6.5	40-60	0.01-0.05	PRL **84**, 1398 (2000), PRC **71**, 055202 (2005)
GEp-II	3.5-5.6	4.6	6.5	70	0.05-0.09	PRL **88**, 092301 (2002) PRC **85**, 045203 (2012)
GEp-III	5.2-8.5	4.0, 5.7	7	80-85	0.07-0.18	PRL **104**, 242301 (2010)

Future Experiments: Moderate increase in Solid Angle → Huge increase in FOM!

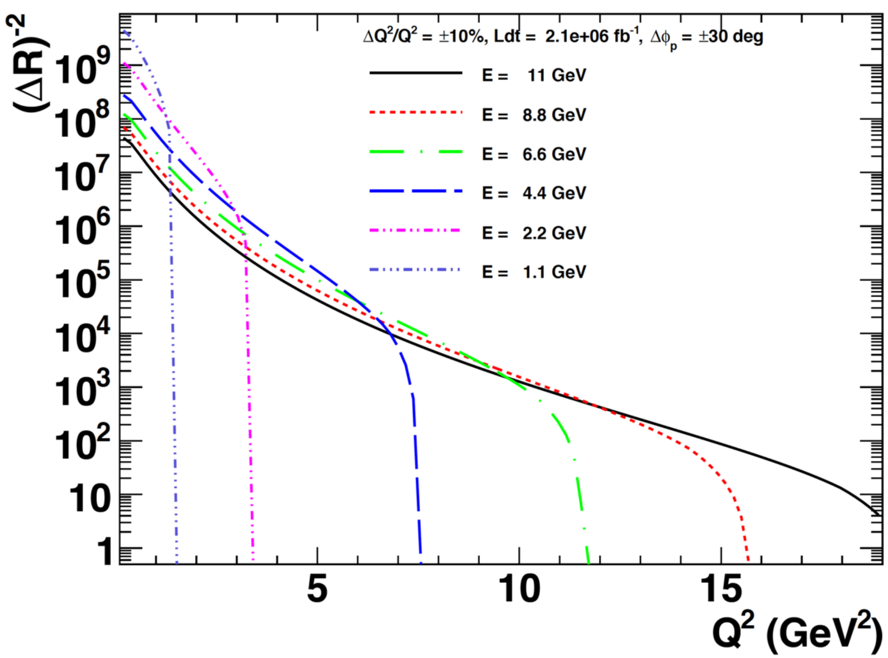

Theoretical PT FOM vs. Q^2 for different beam energies

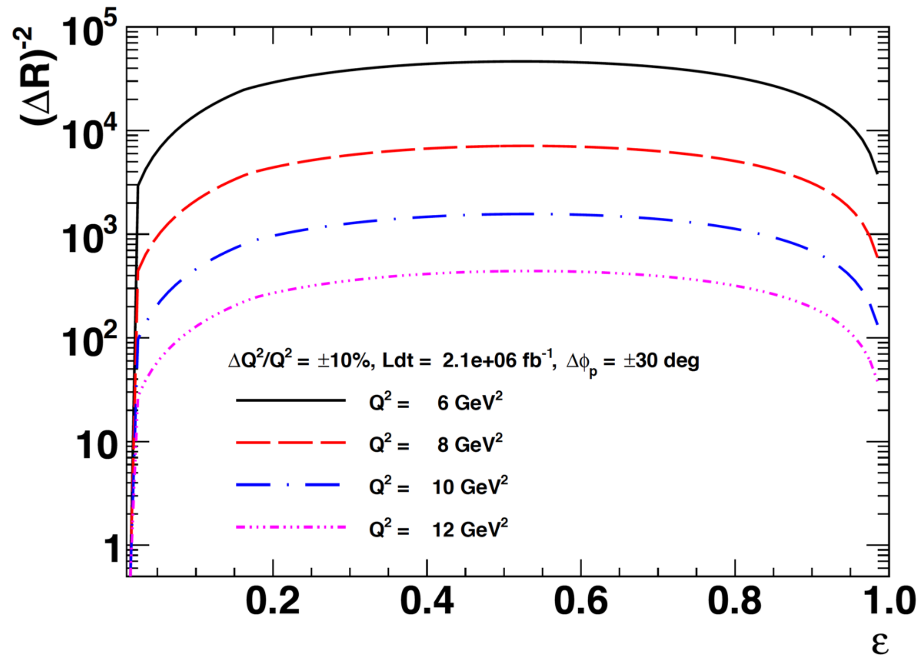

Theoretical PT FOM vs. ε for different Q^2—recall $P_T \sim \sqrt{2\varepsilon(1-\varepsilon)}$